Top-down platform for strong antenna-emitter interactions

Feldman, N.

Award date:
2020

Top-down platform for strong antenna-emitter interactions

Master's thesis

Nick Feldman

Supervisors:
Prof. dr. Niek van Hulst
Prof. dr. Andrea Fiore

Eindhoven, October 2020

Abstract

In everyday physical processes, the coupling between light and matter is usually rather weak and can be ignored. Quantum emitters positioned inside an optical cavity, however, experience a modified electromagnetic environment which enhances the coupling with light. In the weak coupling regime, for example, the emitters experience a dramatic enhance in decay rate. More pronounced effects can occur when the light-matter coupling rate is faster than the decoherence rates of the system. Here, the light-matter interaction enters the strong coupling regime, where new hybrid states are formed containing both light and matter properties. In this exotic regime, light is thus able to couple in such a strong manner with matter as to completely change its inherent properties, opening routes for potential applications in quantum information technologies, highly efficient lasing and the modification of chemical landscapes.

In this thesis, the strong coupling regime is explored between quantum emitters and plasmonic cavities. More specifically, it will be shown how an ensemble of emitters can couple strongly to top-down fabricated plasmonic nanostructures, forming hybrid polariton states. An experimental set-up has been built which is able to detect the strong interactions in the frequency domain. Furthermore, electromagnetic finite-difference-time-domain simulations are executed, supporting the experimental findings throughout this work. The work performed in this thesis offers a stable and reproducible platform for studying strong-light matter interactions, forming a baseline for future experiments.

Contents

Chapter 1

Introduction

Light is an indispensable tool in our every day lives. The most prominent example is without doubt vision, which allows us to obtain spectrally resolved information about our surroundings, that is, we are able to distinguish objects by their different colors and shades. Here, light is incident on the object, after which the scattered light of the object is detected by two highly sensitive cameras: our eyes. Light is also exploited as a sustainable source of energy. Solar cells, for example, convert the energy of incident sunlight into electricity, providing us with all our daily luxury.

Likewise, in the field of applied sciences, the applications of light are omnipresent. With the use of suitable equipment, for example an optical microscope, the aforementioned example of vision can be expanded to dimensions which are orders of magnitude smaller than our naked eyes can see. This allows us to detect and investigate the complex behaviour of biological cells, bacteria and viruses. Intimately linked to this is the identification of disease or infection, thus allowing light to tell us if we are healthy or sick. Furthermore, light is used as a probe in the detection and quantification of molecular species, where light is able to tell us if a species might be toxic or explosive.

In all the aforementioned examples, we obtain information about a certain object thanks to its interaction with light, where the light probes the intrinsic properties of the specific object. In all these cases, the probing light does not change the intrinsic characteristics of these objects, due to the weak coupling between light and matter. In cases such as molecular species detection, we can consider ourselves fortunate that this is not the case. We would not want the probe light to alter the intrinsic properties of the object we want to investigate! This would also be very concerning in the case of our vision: if light was able to interact with objects in such a strong manner as to change its properties, we would not observe objects as how they intrinsically are.

Suppose, however, that the interaction between light and matter is so strong that it would change the intrinsic properties of matter? This would be a very exciting regime to investigate indeed, not to mention the potential routes for applications it would open up.

This exotic regime is exactly the regime that is investigated in this thesis. It will be shown how light is able to strongly interact with matter as to create hybridized states which contain properties of both light and matter. In this regime, the individual systems describing light and matter are said to be strongly coupled to one another. This first chapter will discuss all the physics and phenomena relevant to this thesis. As the thread of this thesis concerns strongly coupled systems, we will start the discussion of coupled systems from a classical point of view. We then move on to the coupled systems which are investigated in this thesis: the strong coupling between light and matter. After a review of the literature on strong light matter interactions, the state of the art and potential applications of this phenomenon are discussed. Finally, the goal of this thesis will be defined.

1.1 Classically coupled systems

We start the discussion of coupled systems from a classical point of view. It will be seen that many characteristics of the light-matter coupling relevant to this thesis can be understood from a simple classical example, providing a strong intuitive foundation.

Consider the coupled system of two harmonic springs depicted in figure 1.1 a. Another example of a classical coupled system is the coupled pendulum, depicted in figure 1.1 b. The system can be modelled by the following equations of motion [38]:

$$M_1 \frac{d^2x_1}{dt^2} + k_1 x_1 + \kappa(x_1 - x_2) = 0, \tag{1.1}$$

$$M_2 \frac{d^2x_2}{dt^2} + k_2 x_2 - \kappa(x_1 - x_2) = 0. \tag{1.2}$$

Here, $x_1(t)$ and $x_2(t)$ are the displacements in time of the two bodies with respect to their respective equillibrium positions $x_{1,eq}$ and $x_{2,eq}$, M_1 and M_2 the masses of the two bodies, k_1 and k_2 the spring constants of the two springs and κ the coupling constant between the springs. For the moment it is assumed that there is no damping affecting the motion, which will be added later.

Substituting the ansatz $x_i(t) = A_i e^{(i\omega_\pm t)}$ into the coupled system, the following matrix equation is obtained:

$$\begin{bmatrix} k_1 + \kappa - M_1\omega_\pm^2 & -\kappa \\ -\kappa & k_2 + \kappa - M_2\omega_\pm^2 \end{bmatrix} \begin{bmatrix} x_1 \\ x_2 \end{bmatrix} = \begin{bmatrix} 0 \\ 0 \end{bmatrix}. \tag{1.3}$$

In order to obtain non-trivial solutions, the determinant of the coefficient matrix has to be set to zero. This results in the following expression for the hybrid frequencies:

$$\omega_\pm^2 = \frac{\omega_1^2 + \omega_2^2 \pm \sqrt{\omega_1^2 - \omega_2^2 + 4\Omega^2\omega_1\omega_2}}{2}, \tag{1.4}$$

where $\omega_1 = \sqrt{\frac{k_1+\kappa}{M_1}}$, $\omega_2 = \sqrt{\frac{k_2+\kappa}{M_2}}$ and $\Omega = \sqrt{\frac{\kappa^2}{M_1 M_2 \omega_1 \omega_2}}$.

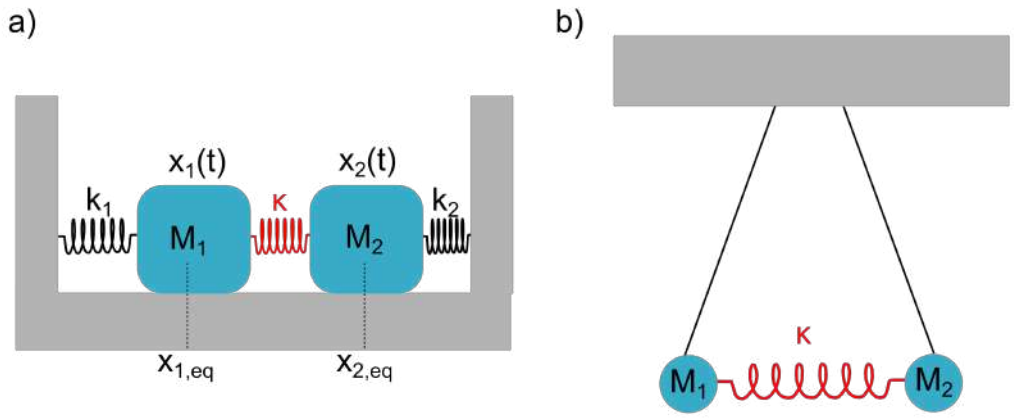

Figure 1.1: Classically coupled oscillator systems. Coupled a) springs and b) pendulums.

For simplicity the masses of the two bodies are set equal ($M_1 = M_2 = M$) and the spring constants are set to $k_1 = k$, $k_2 = k + \Delta k$. Δk thus represents the detuning in natural frequency of the two springs. The following expression is then obtained:

$$\tilde{\omega_{\pm}}^2 = \frac{1}{2}\Delta\tilde{k} + (1+\tilde{\kappa}) \pm \frac{1}{2}\Delta\tilde{k}\sqrt{1+(\frac{4\tilde{\kappa}}{\Delta\tilde{k}})^2}, \tag{1.5}$$

where $\Delta\tilde{k} = \frac{\Delta k}{k_0}$ is the dimensionless detuning, $\tilde{\omega_{\pm}} = \frac{\omega_{\pm}}{\omega_0}$ the dimensionless hybrid frequencies and $\tilde{\kappa} = \frac{\kappa}{k_0}$ the dimensionless coupling strength. For the uncoupled system ($\kappa = 0$), the situation is sketched in figure 1.2a, where the frequency dispersion of the two modes is plotted versus the detuning. Two independent modes are observed which cross at exactly zero detuning, corresponding to the situation of two identical springs.

When coupling is introduced the situation changes, as is seen in figure 1.2b. Two coupled supermodes are distinguished, which no longer cross each other. Instead, a clear splitting in frequency is observed at zero detuning, with magnitude $\mid \omega_+ - \omega_- \mid = \Omega$ and thus proportional to the coupling strength. Furthermore, the solutions of 1.1 and 1.2 can no longer be expressed as a function of two separate springs. It is thus said that the coupled modes are hybridized. Note that for greater detuning magnitudes, the hybrid modes approach the uncoupled modes again.

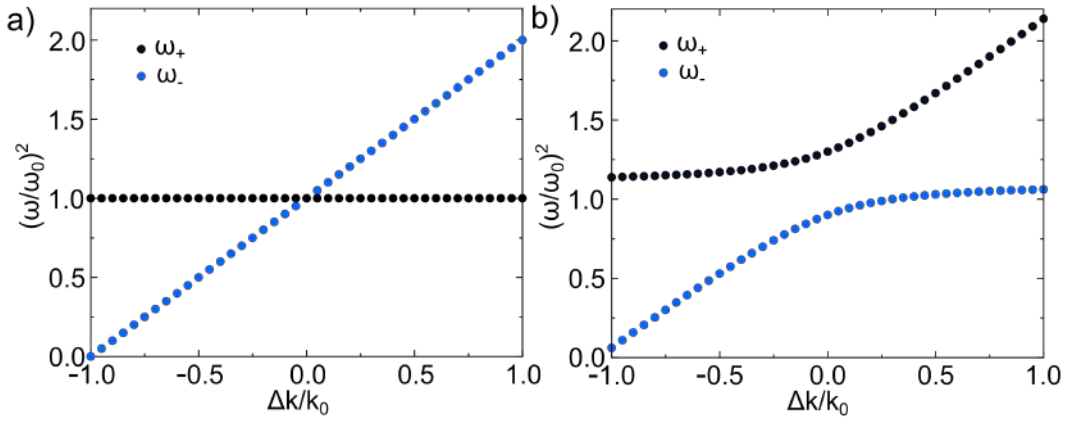

Figure 1.2: Frequency of the hybrid modes of a classical coupled spring as a function of spring detuning for a) $\tilde{\kappa} = 0$ and b) $\tilde{\kappa} = 0.1$

Frictional losses have been completely neglected in the analysis above and can be easily included into equations 1.1 and 1.2 by adding damping terms $\gamma_1 \frac{dx_1}{dt}$ and $\gamma_2 \frac{dx_2}{dt}$ to the respective equations. Here, γ_1 and γ_2 are the friction coefficients of spring 1 and 2 respectively. The hybrid frequencies of the two supermodes now become complex valued, which introduces a linewidth to the solutions represented by the imaginary part of the frequencies. The effect of this linewidth is depicted in figure 1.3. When the coupling is strong enough, the hybrid frequency branches still clearly avoid crossing. However, as the losses of the system are increased, the linewidth of the hybrid frequencies overlap and no clear anti-crossing with corresponding frequency splitting can be observed any longer. Thus, in order to observe the effects of system coupling experimentally, the coupling strength needs to outweigh the losses of the system. For the classical coupled oscillator, this statement can be quantified as follows [38]:

$$\Omega > \frac{\gamma_1}{m_1} + \frac{\gamma_2}{m_2}. \tag{1.6}$$

This expression provides an intuitive requirement for coupled systems. A more precise definition for the coupled systems relevant to this thesis will be given in the next section.

To summarize: When the coupling strength is large compared to the sum of all the losses, the normal modes of the separate oscillators hybridize into two supermodes which show a characteristic anti-crossing with corresponding frequency splitting. When the damping of the oscillators is increased such that the losses start to outweigh the coupling strength, the hybrid frequencies of

the supermodes approach the frequencies of the uncoupled separate oscillators again. An intuitive way to approach this phenomenon is by considering the so called coherence time of the coupling, which is given by $\tau_c = \frac{1}{\Omega}$. For coupling effects to be observable, one would need oscillation times longer than this coherence time. Timescales can also be connected to the losses of the system in the following way: $\tau_l = \frac{1}{\gamma_1} + \frac{1}{\gamma_2}$. When damping is thus increased, the characteristic time of the oscillation is decreased. If the damping is strong enough, the oscillation time would be too fast for coupling to be observable. This corresponds to the overlapping of the linewidths of the frequencies in figure 1.3b.

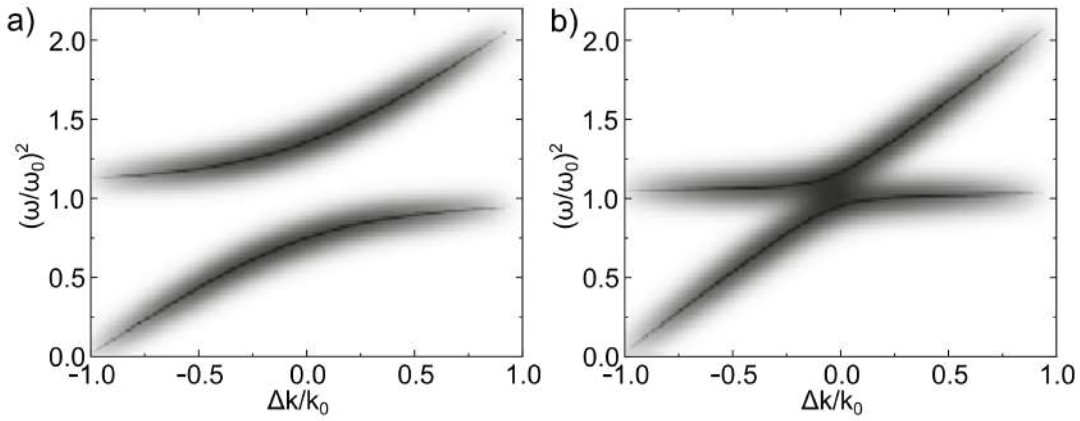

Figure 1.3: Effects of losses on the hybrid modes of a coupled system. In a) the coupling strength is still strong enough to observe a splitting in resonance, but in b) the losses start to overrule the coupling strength such that the splitting disappears.

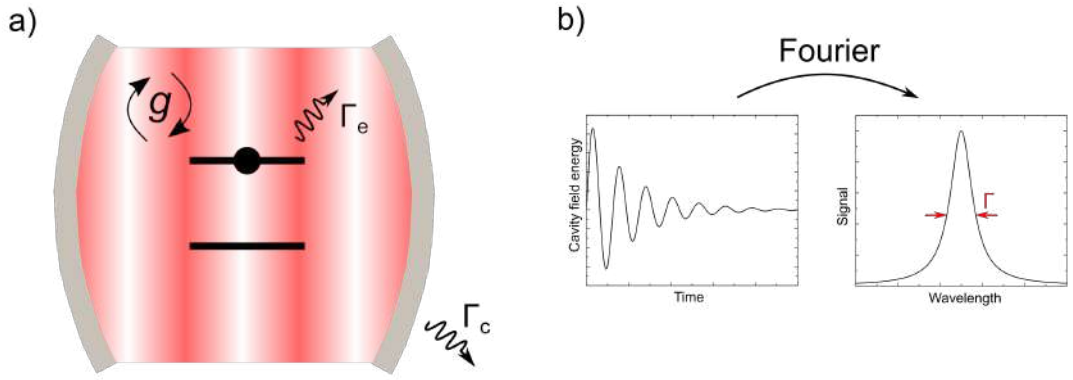

Figure 1.4: Cavity-emitter coupling principles. a) An emitter is coupled to an optical cavity with coupling strength g. The emitter and cavity have intrinsic losses represented by Γ_e and Γ_c respectively. b) The electric field in the cavity is exponentially decaying due to the cavity losses. Fourier transforming the exponentially decaying oscillation obtains a Lorentzian, of which the linewidth represents the losses.

1.2 Light-matter coupling schemes

After the introduction of classically coupled systems and the discussion of its general properties, we will switch gears to the coupling characteristics between light and matter, relevant to this thesis work. Suppose there is an optical cavity, which for simplicity can be considered as two highly reflective mirrors. Light will bounce back and forth between the mirrors and is effectively confined in the region between the mirrors. The cavity has a certain fundamental resonant wavelength, which can be obtained by solving Maxwell's equations and applying the appropriate boundary conditions at the edges of the cavity.

Suppose now that a photon emitter, represented by a two level system, is positioned in the cavity, as shown in figure 1.4a. The emitter also has a resonance, defined by the energy difference between the two levels. If the resonances of the cavity and the emitter are overlapping, the cavity and emitter are coupled to each other. This can be pictured as follows: a two level system can emit a photon by spontaneous emission. This radiated photon is then trapped in the cavity and will remain there until it is re-absorbed by the two level system. Here, there is thus a coherent exchange of energy between the cavity and the emitter, and it is said that cavity and emitter are coupled to each other. The strength of this coupling g is given by the inner product of the dipole moment of the emitter $\vec{\mu}$ and the electric field $\vec{E}$ trapped in the cavity:

$$g = \vec{\mu} \cdot \vec{E}. \tag{1.7}$$

If it is assumed that a single emitter is positioned in the cavity, interacting with one single trapped photon, the electric field $\vec{E}$ simplifies to the "electric field per photon" $\vec{E_0}$, which is given by [20]:

$$E_0 = \sqrt{\frac{\hbar\omega}{\epsilon_0 V}}, \tag{1.8}$$

where $\hbar\omega$ is the photon energy and V the volume of the cavity mode. It is seen here that for smaller mode volumes, the cavity-emitter coupling strength increases. Intuitively, this can be pictured as follows: for smaller mode volumes, the photon needs to cover a smaller traveling distance before it is re-absorbed again, thereby increasing the rate of energy exchange between emitter and cavity and thus the coupling strength.

As said, the description given above is valid for one single emitter positioned in the cavity. When multiple emitters are present, the coupling strength is expected to increase, as there are now more emitters for the cavity to couple to. Indeed, the coupling strength for multiple emitters in the cavity g_n can be extended as [20]:

$$g_n = \sqrt{N} g_0, \tag{1.9}$$

with g_0 the single emitter coupling strength and N the number of emitters in the cavity.

Loss mechanisms

In the discussion above, internal losses have been completely neglected. In reality, however, there will always be loss mechanisms present in the system. The losses are represented by a linewidth Γ, pictured as follows. The oscillating electric field in the cavity decays exponentially in time due to the cavity losses, as shown in figure 1.4b. To illustrate the response in the wavelength domain, the time response is Fourier transformed. The obtained curve is a Lorentzian and the full width at half maximum (FWHM) of this curve is the linewidth, representing the losses. If there were no losses present, the oscillation would not be decaying and the Fourier transform would be a Dirac delta. Thus, the greater the losses, the greater the linewidth. The ability of the cavity to confine the light is represented by a quality factor Q, as

$$Q = \frac{\omega_c}{\Gamma_c}, \tag{1.10}$$

with ω_c the resonant frequency of the cavity. Higher quality factor cavities thus confine the light more effectively. In the same manner, an emitter linewidth Γ_e can be defined, representing the decoherence rate of the emitter.

Strong cavity-emitter coupling

Returning to the picture of a two level emitter positioned in the cavity, the coupling characteristics are changed when the losses are taken into account. Suppose again that a photon is emitted by the two level system. The photon will now only be re-absorbed if the coupling between the cavity and the emitter is faster than the cavity loss rates. The same holds for the re-emission of a photon by the emitter, which will only happen if the coupling to the cavity is faster than any internal losses in the emitter. In short, coherent energy exchange between the cavity and the emitter will take place if the coupling strength outranks the system losses. This regime of coherent energy exchange between cavity and emitter is referred to as the strong emitter-cavity coupling regime. Formally, the strong coupling regime is defined according to [2]:

$$g > \frac{\mid \Gamma_c - \Gamma_e \mid}{4}. \tag{1.11}$$

In this strong coupling regime, the cavity and the emitter become quantum mechanically entangled and thus cannot be viewed as separate objects any longer. This is more intuitively seen in the frequency domain where, characteristic for strongly coupled systems, normal mode splitting occurs. The intrinsic resonances of the cavity and the emitter here split into two branches, ω_+ and ω_-, described by [42]:

$$\omega_\pm = \frac{1}{2}(\omega_c + \omega_e) \pm \Omega_r. \tag{1.12}$$

Here, Ω_r is the Rabi frequency and is given by

$$\Omega_r = \sqrt{g^2 + 1/4(\omega_c - \omega_e)^2}. \tag{1.13}$$

From equation 1.13 it follows that the split modes avoid crossing each other when the frequencies are plotted versus the cavity emitter detuning $\omega_c - \omega_e$. Note the phenomenological similarities between a strongly coupled cavity-emitter system and a classically coupled system as discussed in section 1.1.

In this section, cavity-emitter coupling characteristics are introduced from an intuitive viewpoint. A more precise model, described in appendix A, will treat the strong coupling regime from a quantum mechanical point of view.

Weak cavity-emitter coupling

Besides light confinement, optical cavities alter the photonic environment surrounding an emitter. Here, the emitter experiences an increased local density of optical states (LDOS) with respect to free space at the resonance frequency of the cavity. This enhanced LDOS ensures that the probability of an emitter in the excited state to relax to the ground state increases. Consequentially, the excited state lifetime of the emitter is reduced and thus the spontaneous emission, or fluorescence, is enhanced, which is referred to as the Purcell effect or Purcell enhancement [44]

When the cavity losses are now greater than the coupling strength, a spontaneously emitted photon rapidly leaves the cavity and thus has no time to be re-absorbed by the emitter. In this situation, the emitter is still coupled to the cavity modes (rather than free space modes), but the coupling of the cavity back to the emitter is dominated by the cavity decay. Energy is thus not reversibly exchanged between the two, rather the energy is directed out of the cavity in a unidirectional flow. In this weak coupling regime, the cavity and the emitter remain two separate objects, such that there is no mode splitting and thus the frequency of the enhanced emission of the photons remains unchanged. Weak coupling is an interesting phenomenon where it is desired to enhance the fluorescence signal of emitters with low intrinsic quantum efficiencies [65] or the creation of bright single photon sources.

1.2.1 Strong interactions in diffraction limited cavities

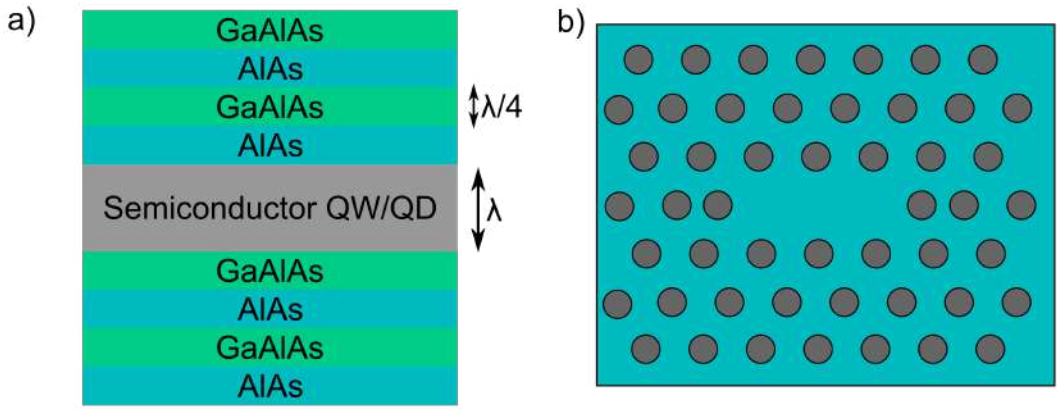

Figure 1.5: Solid state cavities for high Q-factor light confinement based on a) a Bragg reflector and b) a photonic crystal.

Coherent energy exchange between an emitter and a cavity was first experimentally realized in the case of many [28] and single [48] emitters in 1983 and 1987 respectively. As emitters, Rydberg atoms were used, which provide relatively strong interaction strengths due to their high transition dipole moments. Furthermore, they have a long inherent spontaneous emission lifetime, such that the cavity mode is the only relevant mode the atom couples to. For the Rydberg atoms used, the resonant wavelength between adjacent energy levels lies in the millimeter range, which allowed for the use of high Q-factor superconducting microwave cavities. Strong atom-cavity interaction was then pushed into the domain of optical wavelengths, by the observation of normal mode splitting in the frequency domain for many [46] and single [61] atoms in an optical cavity.

In these atom experiments, a high vaccuum environment was required. Strong coupling was reached in condensed matter structures in 1992 [62] by employing a Fabry-Perot microcavity and a semiconductor quantum well as optical material. The cavity is made of two structures consisting of alternating layers of high and low index materials: creating a Bragg reflector as shown in figure 1.5a. In the 2000's, together with the rise of photonic crystals, the design of these solid-state cavities was optimized [1] such that extremely high Q-factors were obtained, while reducing the effective mode volumes. These advances ultimately pushed the strong coupling regime to the single quantum dot level in a semiconductor micropillar [47] and a photonic crystal defect cavity [69].

The bulk of the strong coupling experiments conducted in the microcavities discussed so far are performed at cryogenic temperatures. This is done to decrease the emitter's linewidth as much as possible. In combination with high Q factor cavities, the system losses were supresses suffiently well to observe the mode splitting. Several groups have reported of room temperature strong coupling in solid state microcavities [24] [29] [30] as well, but these were limited to many emitters that coupled to the cavities. Recalling equation 1.9, the coupling strength increases dramatically and here the system ensemble is coupled strong enough in order to overcome the fast decoherence rates of the emitter at room temperature.

Room temperature strong coupling of a single emitter, however, remained to the cryogenic temperature regime, despite the extremely high cavity Q factors reached. To overcome the intrinsic decohorences of an emitter, the coupling strength has to be enhanced even more. Looking at equation 1.7 and 1.8, the only sensible parameter that can be optimized is the electric field mode volume, which has to be reduced to enhance the interaction strength. In solid state micro cavities, however, the wavelength of the confined light imposes a limit to the minimum volume achievable, namely $(\frac{\lambda}{2})^3$ and thus formed a bottleneck in strong coupling research. Different types of cavities, which are able to confine light to the subwavelength lengthscale will be discussed in the next

section. It will be seen that these sub-diffraction limited cavities led to several breakthroughs in the physics of strongly coupled systems.

1.3 Light confinement below the diffraction limit

But how can light be squeezed into volumes smaller than the diffraction limit? Suppose for example we have a photon of energy $\hbar\omega$ and wavevector $k = \sqrt{k_x^2 + k_y^2 + k_z^2}$ connected by the free space dispersion relation $\omega = ck$. Now, Heisenberg's uncertainty principle states that we cannot know the position and momentum of a particle simultaneously with arbitrary accuracy:

$$\Delta(\hbar k_x) \cdot \Delta x \geq \hbar/2, \tag{1.14}$$

or

$$\Delta x \geq 1/2\Delta k_x. \tag{1.15}$$

This states that the amount of confinement in a certain direction is determined by the spread in wavevector component in that same direction. In free space, the maximum spread in wavevector component Δk_x is equal to the magnitude of the total wavevector $k = 2\pi/\lambda$, and so we arrive at the diffraction limit:

$$\Delta x \geq \frac{\lambda}{4\pi}. \tag{1.16}$$

A more precise expression, which takes into account optical parameters such as the numerical aperture of lenses or objectives, will be stated in chapter 2.

But suppose it was possible to increase the spread in wavevector components beyond the length of the total wavevector, for example $k_x > k$. This would mean we could in principle reach arbitrary confinement in the x-direction. At the same time, in order to still fulfil the Pythagoras theorem for the total wavevector, this would mean that the wavevector components perpendicular to the component k_x would become imaginary, for example $k_z = i\kappa$. Recalling the expression for a plane wave in the z-direction $e^{ik_z z}$ and substituting the imaginary wavevector component, we arrive at an exponentially decreasing and increasing field. The exponentially increasing field is non-physical, since it would violate the conservation of energy. The exponentially decreasing field, however, is a physical field which is referred to as the evanescent field or, as it is exponentially decreasing, the near-field. Thus, we see that it is mathematically possible to squeeze light in volumes below the diffraction limit into the near-field.

Localized surface plasmons

But how do we physically access the near field? Suppose there is a metallic structure with a size on the order of tens of nanometers, smaller than the wavelength of light. When a propagating electromagnetic wave is incident on this nanostructure, the free electrons in the metal will start to oscillate. This collective oscillation of free electrons in a nanostructure is called a localized surface plasmon (LSP). The resonance frequency of this oscillation, the localized surface plasmon resonance (LSPR), will depend on the natural frequency of the electrons in the specific metal (the plasma frequency), and the geometry of the structure. Because the structure is smaller than the wavelength of incident light, the k-vectors of these LSP's are very high and thus evanescent fields can be created. Thus, using metallic nanostructures, light can be trapped in sub-diffraction limited near field hotspots. These structures can be engineered in different shapes to modify the LSPR for efficient coupling with light. LSP's are collective electron oscillations confined to the metallic structure and thus cannot propagate, in contrast to surface plasmon polaritons. The ability of metallic nanostructures to confine light into localized hotspots has led to the concept of the optical antenna, which will be discussed in the following section.

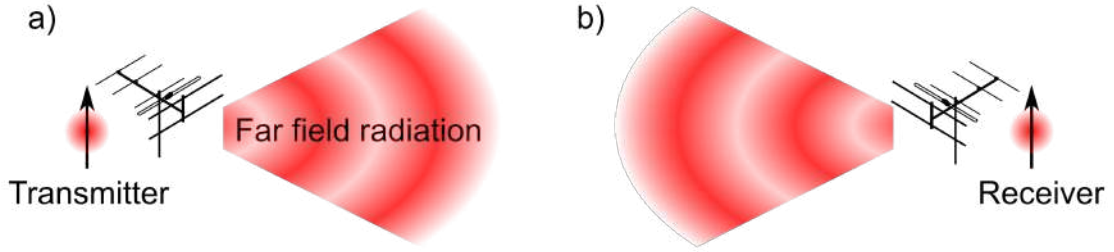

Figure 1.6: Sketch of the working principle of an antenna in the case of a) a transmitter and b) a receiver.

1.3.1 Optical antennas

Antennas are widely familiar in today's society. Operating in the radio frequency regime, antennas are used to convert freely propagating electromagnetic radiation into localized energy hotspots in the case of receivers. Interchanging the fields and the sources by reciprocity, equivalently an antenna is used to transmit localized signals into the far-field. These concepts are sketched in figure 1.6. Antennas are required to have a similar size compared to the wavelength of propagating radiation, which makes them of the order of meters in the case of broadcasting and receiving radio channels. Far field radiation is then coupled to electron oscillations in the antenna which can be received as currents, representing the localized signal.

By arguing that Maxwell's equations are scale invariant, the antenna concept can be scaled down to wavelengths representing visible light. In this regime the antennas, requiring a size of hundreds of nanometers, are called "optical antennas". Many properties that hold for radio wave antennas are also valid for optical antennas. However, as field penetration into the bulk of a radio antenna can be ignored, this is not so in the case of an optical antenna. This non-negligible skin depth and, among others, the altered plasmonic response of metallic nanostructures, imposes critical differences between radio and optical antennas.

As mentioned in the previous section, focusing of optical radiation is limited by the wave nature of light, where diffraction effects prevent localization of electromagnetic energy below approximately half the wavelength, that is, hunderds of nanometers. The length scale of a typical source and receiver of this radiation, for example fluorescent molecules or quantum dots, can be as low as sub-nanometer. There is thus a large mismatch between the diffraction limited localization of optical radiation and the cross section of the respective transmitters and receivers, resulting in inefficient coupling between far-field radiation and quantum emitters. Optical antennas can thereby, by coupling far-field radiation into near-field hotspots of the order of nanometers, overcome the diffraction limit of traditional focusing and increasing the sensing efficiency [60]. Consequently, besides tight focusing, antennas are able to enhance the efficiency of releasing localized energy into the far-field as well. These advantages of optical antennas pave the way to applications ranging from biosensing [3] to spectroscopy [39].

Despite the numerous possibilities and applications offered by optical antennas, they are not yet present in state of the art technological devices. This is explained by the ultra small size requirement of these structures. Although these length scales have become accessible by novel nanofabrication techniques, such as electron beam lithography and focused ion beam milling, the low throughput of these methods imposes a bottleneck in the ultimate breakthrough in devices on the industrial scale. These nanofabrication techniques, along with their strengths and weaknesses, will be further discussed in chapter 2.

1.3.2 Antenna parameters

Antenna efficiency

Suppose an emitter is positioned close to an antenna and the total power radiated by the antenna into the far-field is P_{rad}. Energy can, however, also be dissipated via other channels, such as heat in the metal of the antenna or internal relaxation pathways of the emitter. The amount of power that is lost via these channels is termed P_{loss}. Then, an antenna efficiency or total quantum yield η can be defined as:

$$\eta = \frac{P_{rad}}{P_{rad} + P_{loss}}. \tag{1.17}$$

An internal quantum yield for an emitter can be defined in the same way as:

$$\eta_e = \frac{P^0_{rad}}{P^0_{rad} + P^0_{loss}}, \tag{1.18}$$

where P^0_{rad} is the radiated power of the emitter without the presence of the antenna and P^0_{loss} the internal loss of the emitter. In order to distinguish the internal loss of the emitter and the pure antenna losses $P^{antenna}_{rad}$, equation 1.17 can be recast in the following form using equation 1.18 as:

$$\eta = \frac{P_{rad}/P^0_{rad}}{P_{rad}/P^0_{rad} + P^{antenna}_{rad}/P^0_{rad} + (1-\eta_e)/\eta_e}. \tag{1.19}$$

It is assumed here that the internal emitter losses are not affected by the antenna. For extremely efficient emitters ($\eta_e = 1$), the antenna can only reduce the total quantum yield due to the losses in the antenna. For lower quantum yield emitters, however, the presence of the antenna can boost the total efficiency.

Directivity and gain

The antenna efficiency is also strongly dependent on the direction in which the antenna radiates the energy. This parameter is described by the directivity D(θ,ϕ), given by:

$$D(\theta, \phi) = \frac{4\pi}{P_{rad}} p(\theta, \phi), \tag{1.20}$$

where θ and ϕ are the viewing angles and $p(\theta, \phi)$ the angular power density. It is shown [17], [21] that an optical antenna can accurately tailor the angular emission in a desired direction. The combination of the directivity and antenna efficiency is referred to as the antenna gain G as follows:

$$G = \frac{4\pi}{P_{rad} + P_{loss}} p(\phi, \theta) = \eta D. \tag{1.21}$$

Effective wavelength

The design of an antenna is related to the wavelength of the incoming radiation. For example, in the so called half wave antenna, or $\lambda/2$ antenna, the antenna length is designed such that it equals half the wavelength of the incoming radiation. The electron oscillations excited by the radiation closely follow the incident wave, such that exactly half the wavelength of the electron oscillations fits in the antenna. Higher order electron oscillations can be excited, by choosing for example antenna lengths equal to λ, $3\lambda/2$ etc.

In optical antennas, however, the electron oscillations do not closely follow the incoming radiation, because now the effects of skin depth can no longer be ignored. As fields penetrate the metal, the finite electron density causes a delay between plasma oscillations and the incoming

driving fields. Consequently, the optical antenna is driven by an effective wavelength λ_{eff}, which is given by [37]:

$$\lambda_{eff} = n_1 + n_2 \frac{\lambda}{\lambda_p}, \tag{1.22}$$

where n_1 and n_2 are constants with dimension of length which are determined by the geometry of the antenna and λ_p the plasma wavelength.

Indeed, it is reported [34] that the resonant lengths in plasmonic nanostructures are smaller than conventional antenna theory predicts. How much smaller this effective resonant length is depends on the geometry of the antenna, but in practice it is a factor of 2-5 times smaller than the driving field wavelength.

Electric field enhancement

Optical antennas cannot only confine light into sub-diffraction limited volumes, they are also able to greatly enhance the electromagnetic fields. Field enhancement occurs because electromagnetic energy is now squeezed into very small volumes, such that the spatial mode energy density becomes large. The smaller the effective mode volume V_{eff}, the larger the spatial mode energy density. Besides, it is expected that, in the cavity picture of a nano antenna, the Q-factor, which accounts for the spectral mode energy density, will affect the field enhancement as well. A scaling law, which relates the field enhancement in a plasmonic cavity with the Q-factor and effective mode volume, can be derived as [31]:

$$\frac{\mid E_{loc} \mid^2}{\mid E_i \mid^2} \propto \frac{Q^2}{V_{eff}}, \tag{1.23}$$

where E_{loc} is the locally enhanced electric field and E_i the incoming field.

Additionally, the field enhancement is expected to depend on the frequency of incoming radiation, because the electron oscillations are more efficiently excited at the LSPRs than at other frequencies. Lastly, electric field enhancement depends on the shape of the metallic nanostructures. Sharp edges, for example, lead to a denser crowding of the electric field lines than blunt edges, causing a greater field enhancement, which is known as the "lightning rod effect".

In this section it was seen how optical antennas are able to confine light at sub-diffraction limited volumes. This led to several breakthroughs in strong-coupling research, as will be shown in the following section.

1.3.3 Strong antenna-emitter coupling.

The first experiments involving strong coupling between plasmonic modes and emitters were conducted in planar metal surfaces [5], plasmonic crystals [56] and metal nanostructures [67] [6]. The majority of these early experiments used J-aggregates as optical emitters due to their narrow linewidths, but broadband emitters were also reported [22]. The low effective mode volumes in these plasmonic cavities ensured high interaction strengths, leading to extremely high Rabi splittings up to 600 meV, values considerably higher than those recorded in solid state cavities. These values approached the so called ultra strong-coupling regime, where the energy splitting becomes comparable to the transition energies of the system. The results relied on measuring the extinction spectra of large areas of metallic sheets or arrays of nanostructures. Strong interaction between many emitters and a single plasmonic structure [53], [70], [49] could also be reached by recording the dark-field scattering and even the photoluminescence [63] signals of the single strongly coupled nanostructures.

These high interaction strengths and observed strong interaction in single nanostructures proposed the following question: "can a single quantum emitter be pushed into the strong coupling regime at room temperature?". This achievement would simplify the harsh cryogenic experimental conditions necessary in microcavities considerably and would pave the way for the implementation in future room temperature devices. In 2016, two groups have reported for the first time on a single emitter strongly coupled to a plasmonic cavity. The first group, conducted by *Santhosh et.al*

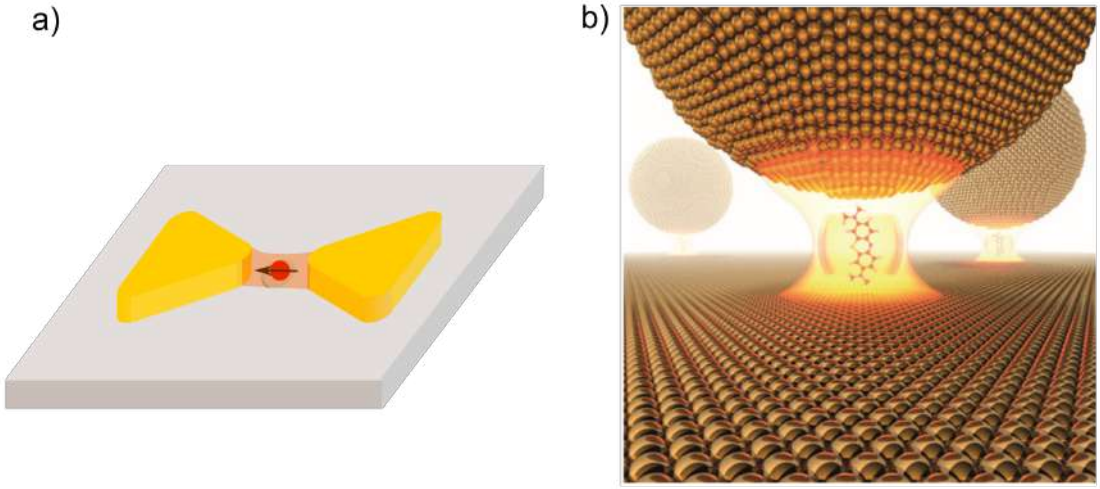

Figure 1.7: Sketches of single emitter strong coupling experiments conducted at room temperature. a) A single quantum dot is placed in the gap of a top down fabricated bowtie antenna. b) A single dye molecule is chemically placed in the gap of a NPoM cavity. (Figure adapted from [12]

[52] claimed to couple a single quantum dot to the plasmon modes of a bowtie antenna structure, as depicted in figure 1.7a. One of the biggest challenges of single emitter strong coupling in these nanocavities is accurately positioning a single emitter in the hotspot of the cavity. *Santhosh et.al* achieved this by using a two step lithography process, where a nanohole is created in the middle of the gap into which the quantum dots can fall into by capillary action.

The second experiment, carried out by *Chikkarady et.al* [12] chose the bottom up self assembly approach of a nanocavity, instead of the direct top down approach by [52]. A basket shaped molecule formed a linker between a gold nanoparticle and a gold layer. In the metallic layer, image charges of the gold nanoparticle are induced, ensuring an effective nanoparticle dimer cavity. The gap between the nanoparticle and the metallic sheet thus creates an intense hotspot. Impressively, a single dye molecule can now be positioned inside the basket shaped linker, which can then couple strongly to the cavity.

These breakthroughs pushed the regime of single emitter quantum coherences, formerly only accessible at cryogenic temperatures, into the room temperature regime and thereby opening up many pathways for potential applications. The most important applications of strongly coupled light matter systems will be discussed in the next section.

1.4 Applications

1.4.1 Quantum information technologies

As discussed earlier, an emitter can coherently exchange energy with an optical cavity when the coupling strength is greater than the losses of the system. Emitter and cavity states can no longer be distinguished and a combined cavity-emitter quantum state is created. Suppose the state of a two level emitter with ground state $|g\rangle$ and excited state $|e\rangle$ can be written in Dirac notation as;

$$|\psi_e\rangle = c_g\,|g\rangle + c_e\,|e\rangle \tag{1.24}$$

Suppose now that there can be either one photon $|1\rangle$ or no photons $|0\rangle$ present in the cavity. The cavity state can thus be expressed in a similar manner as:

$$|\psi_c\rangle = c_0 |0\rangle + c_1 |1\rangle \tag{1.25}$$

Now, an emitter in the excited state $|e\rangle$ is strongly coupled to an empty cavity $|0\rangle$. The population of the excited state of the emitter and the numbers of photons in the cavity will now fluctuate in a vacuum Rabi oscillation with frequency Ω by emitting and re-absorbing a photon, as depicted in figure 1.8a. When the emitter is in the excited state there is no photon in the cavity, while if the emitter is in the ground state there is one photon present. But what happens after exactly one quarter of the oscillation time $1/4\Omega$? In this situation, the coefficients for the populations are all equal to $c_g = c_e = c_0 = c_1 = 1/\sqrt{2}$ and both the cavity photons and the emitter are in a superposition state.

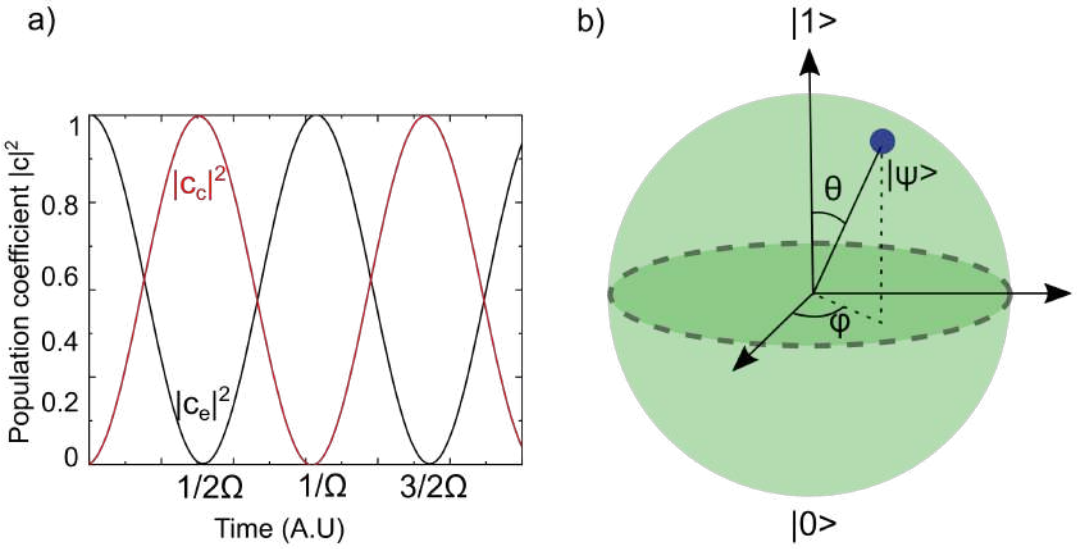

Figure 1.8: a) The evolution of the populations of the number state of the cavity and excited state of the emitter state in a Rabi oscillation. b) Sphere of Bloch, representing the strongly coupled emitter-cavity quantum state.

In strongly coupled systems, quantum states can thus be prepared in a well defined state which is described by Bloch's sphere in figure 1.8b. This superposition state is called a qubit, the quantum mechanical counterpart of the classical bit. The superposition state of a qubit be exploited in quantum information processing. In a processor which operates with qubits, the computational power increases exponentially with the number of qubits, in contrast to a computer operating with classical bits, thus allowing for tremendously enhanced performances. Not only need these qubits be prepared in the desired way, there needs to be a high level of control of these quantum states if quantum computation would ever be a prominent technology. In the field of circuit quantum electrodynamics (QED) [8], extensive efforts have been made in the design of quantum devices with a high level of coherences. A design for a quantum gate which exploits the regime of strong light-matter coupling (in this case ultra strong-coupling regime) has for example been proposed [50], which could potentially offer the desired control of quantum states.

Returning to the cavity-emitter system, the superposition states of the emitter and the cavity are related to each other as can be seen in the system's combined quantum state:

$$|\psi_{comb}\rangle = \alpha_1 |e\rangle |0\rangle + \alpha_2 |g\rangle |1\rangle . \tag{1.26}$$

Here, the total state of the system cannot be factorized in products of the individual states and it is said that the (photon of the) cavity and the emitter are quantum mechanically entangled

to one another. This scheme can be expanded to the quantum entanglement of two emitters as follows. Suppose we have an entangled cavity-emitter state as described by equation 1.26. A second emitter prepared in the ground state ($|g\rangle$) can now be placed in this entangled cavity for a duration of $t = \frac{1}{2\Omega}$. If there would be a photon present in the cavity, it is now absorbed by the second emitter such that it finds itself in the excited state, whereas if no photon was present the second emitter would remain in the ground state. It is seen here that the entanglement of the cavity is transferred to the second emitter, where now the two emitters are entangled as: $|\psi_{comb}\rangle = \alpha_1 |e_1\rangle |g_2\rangle + \alpha_2 |g_1\rangle |e_2\rangle$, where the subscripts 1 and 2 indicate the two entangled emitters.

Due to entanglement, performing a measurement on one state will immediately collapse the other state as well, no matter how far apart the two entities find themselves and could thus provide a scheme in the teleportation of quantum states. Indeed, it has been shown experimentally [11] that such teleportation of quantum states is experimentally possible.

1.4.2 Engineering chemical landscapes

Emitters strongly coupled to a cavity experience a Rabi splitting in their resonant energy levels, where the energies of the new system eigenstates are altered depending on the coupling strength. Strong cavity-emitters interactions thereby modify the energetic landscapes of, for example, fluorescent emitters and can therefore be exploited as a tool to alter the corresponding chemistry of the emitters. Indeed, it has been shown [25] that a chemical reaction can be influenced by strong coupling of the energy pathways, which guide the chemical reaction, to resonant cavity modes.

1.4.3 Polariton lasing

A laser is an oscillator which comprises of an active medium placed inside an optical cavity. When the cavity is modelled by two mirrors, a photon bounces back and forth between the mirrors and is amplified by stimulated emission of the active medium. Making one of the two mirrors partially transparent, a laser beam is thus created.

The active medium can, however, also absorb photons that are trapped in the cavity. Looking at Einstein's rate equation [59] which describe stimulated emission and absorption, it is seen that in order for the system to create gain, there need to be more emitters in the excited state $N_{excited}$ than emitters in the ground state N_{ground} in the active medium: $N_{excited} > N_{ground}$. This is referred to as population inversion. Furthermore, confined photons will eventually leave the cavity due to internal losses. Therefore, there has to be set a certain condition on the amount of emitters in the excited state to compensate for these losses and provide gain. Therefore, a certain threshold has to be reached to acquire population inversion and to overcome the internal losses, such that laser operation is achieved.

In laser operation, the amplified photons by stimulated emission all have the same phase, energy and direction. A laser is thus an example of a coherent state of electromagnetic waves. Likewise, an example of coherent state of matterwaves in termed a Bose-Einstein condensate, in which the energy of the system is so low that individual wavefunctions of atoms all start to overlap to create one coherent atom state. But what happens in the case of particles which are half-matter half-light which also follow boson statistics?

These particles, called polaritons, are exactly the particles which concern strongly coupled systems. When an emitter is strongly coupled to a cavity, the energy levels of both emitter and cavity hybridize, forming a new quantum state: the polariton. In 1996 *Imamoglu et.al* [26] proposed a novel type of laser operation based on a coherent state of polaritons, instead of a coherent state of photons in the conventional laser. They discussed that polaritons can form a condensate via stimulated scattering, which then provide coherent emission of electromagnetic radiation. Due to the intrinsic properties of polariton condensates, polaritons lasing does not rely on population inversion and so the lasing threshold is orders of magnitude lower [13] than in the classical laser. Strong cavity-emitter interactions can thus be exploited in the creation of highly efficient polariton lasers.

1.5 This thesis

This thesis explores the strong interaction between quantum emitters and localized surface plasmons in single metallic nanostructures. More specifically, several designs for these nanostructures are investigated, of which the main results are set out in chapter 5, which could serve as a potential platform for future strong interaction experiments. These plasmonic nanostructures are fabricated with nanolithographic techniques, of which the procedures will be elaborated in great detail in chapter 2. Furthermore, various types of quantum emitters will be considered in the experiments. Advantages, drawbacks and key design considerations are proposed for these different circumstances, which provide crucial knowledge regarding the optimum conditions for achieving strong light-matter coupling.

Proof of strong emitter-antenna interactions will rely on measuring the strong coupling regime in the frequency domain, that is, the observation of mode splitting of the fundamental resonances of the plasmonic cavity and the quantum emitter. To record the resonances of the nanostructures, a home built dark-field scattering microscope is constructed, which is able to characterize the fundamental resonances of single plasmonic cavities through their scattering spectra. The perfomance of the constructed dark-field setup, alongside the optical properties and quality of the fabricated nanostructures, will be discussed in chapter 4. Alongside scattering spectra, the fluorescence spectra of quantum emitters, which provide information about their fundamental resonances, should also show a mode splitting. Therefore, in addition to the dark-field microscope, a confocal fluorescence microscope is built, which is able to record and characterize the fluorescence signal of quantum emitters, down to the single emitter level. More details on the complete home-built experimental setup will be given in chapter 2.

Finally, the experimental results will be thoroughly supported by finite-difference-time-domain (FDTD) simulations, of which the back-bone will be elaborated in chapter 3. In this way, a comparative study between experiment and simulation is set out though out this work. The results of these simulations could then be exploited as a predictive tool to evaluate the performance of future strong emitter-antenna design schemes.

Chapter 2

Experimental setup and techniques

In this chapter, all experimental techniques used in this project will be discussed. First, the home built experimental setup will be thoroughly explained, after which sample nanofabrication and preparation are clarified.

2.1 Experimental setup

In this section, the constructed experimental setup is summarized. It consists of 3 main channels: A dark-field scattering channel, a fluorescence channel and a scanning confocal channel, which will all be separately treated in the coming sections. At the core of this section lies a technique called confocal microscopy, which depends on the rejection of signal that does not lie in the plane of focus. This can be achieved by placing a pinhole in the image plane. Confocal microscopy ensures a higher resolution, but comes at a cost of a limited imaged area. Therefore, to acquire a wide-field image, the illuminated sample needs to be raster scanned through the focus. This is done using a XYZ nanopositioning piezo, as will be discussed in more detail in section 2.1.1.

Diffraction limited resolution

The ultimate resolution of an optical microscope, d, that is, the smallest distance between two point features that can still be discerned, is limited by the diffraction of light. This diffraction limited resolution is given by the following relation:

$$d = \frac{0.61\lambda}{NA}. \tag{2.1}$$

Here, λ is the wavelength of the excitation laser and NA is the numerical aperture of the collection objective, which is a measure of the maximum angle θ of incoming light that can still be accepted by the objective, $NA = nsin(\theta)$, with n the refractive index of the surrounding medium. In order to obtain optimal resolution, a high NA objective is thus required. In this thesis an objective with NA of 1.4 will be used, made possible by immersing the objective in oil ($n = 1.5$). Assuming an excitation wavelength of 680 nm, which will be the primary excitation in this project, the imaging system thus has a lateral resolution of approximately 300 nm.

2.1.1 Scanning confocal microscopy

The first part of the setup is the scanning confocal channel, in which high resolution confocal images of the sample are obtained. A continuous wave (CW) laser, with a main excitation of 680 nm unless otherwise stated, is directed onto the sample via a beamsplitter and an oil immersion

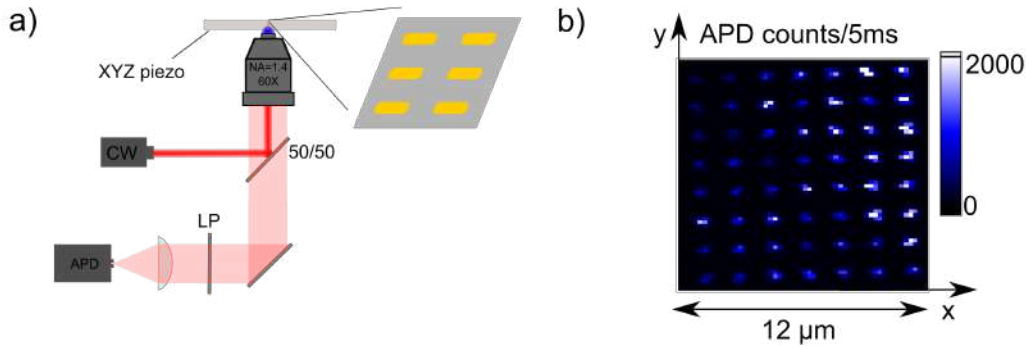

Figure 2.1: Sketch of the scanning confocal channel of the setup. a) A CW laser is tightly focused onto the sample, after which sample signal is collected and imaged onto an APD. b) Example of a scanning confocal image is shown of antenna array showing intrinsic luminescence signal originating from plasmonic structures.

objective (Nikon, Plan-apo 60X / $NA = 1.4$), ensuring tight focusing. Signal originating from the sample is captured by the same objective, after which it is passed through the beamsplitter and subsequently focused onto an avalanche photodiode (APD), where an image of the sample plane is created. The aperture of the APD is a pinhole of approximately 70 μm in radius, ensuring the confocal configuration. A long pass filter can be positioned in between the beamsplitter and the focusing lens when it is desired to block the scattered signal. This is the case if fluorescence signal from quantum emitters, or luminescence signal from plasmonic structures is desired. A sketch of the scanning confocal channel of the microscope is depicted in figure 2.1a. In figure 2.1b, an example confocal image of an antenna array is shown, where intrinsic antenna luminescence is captured.

Confocal images are captured by raster scanning the sample through the diffraction limited spot size. Once the image is taken, accurate (nanometer) control over the position of the sample is possible by placing the sample on a XYZ nanopositioning piezo (Mad City Labs) such as to position single emitters or nano antennas in the focus of excitation.

Alignment

As this channel is extremely sensitive to drift, it is made sure prior to every measurement that all optics are correctly aligned. First it is made sure that the excitation laser is illuminating the sample perpendicularly, after which the collection path is aligned. This is achieved by positioning an emitter or scatterer into the focus of the diffraction limited spotsize and iterative re-positioning of the aperture of the APD in the x-y direction and the focusing lens in the z direction until maximum signal is retrieved. This is of course under the assumption that the optimal focus is positioned at the spot where maximal signal is gathered, which is valid when aberrations are not playing a significant role. Imaging nano structures or quantum emitters after the alignment give diffraction limited bright spots, indicating good alignment

2.1.2 Dark field microscopy

In this section, we will turn our attention to the dark-field scattering channel, which is able to image scatterers in wide-field configuration and spectrally characterize them. A detailed picture of the setup is given in figure 2.2a. The sample is now illuminated from above by a broadband thermal light source by guiding the collimated light through a low NA (Zeiss, Plan-neofluar 20X / $NA = 0.5$) objective. Scattered light from the sample and illumination light from the light source

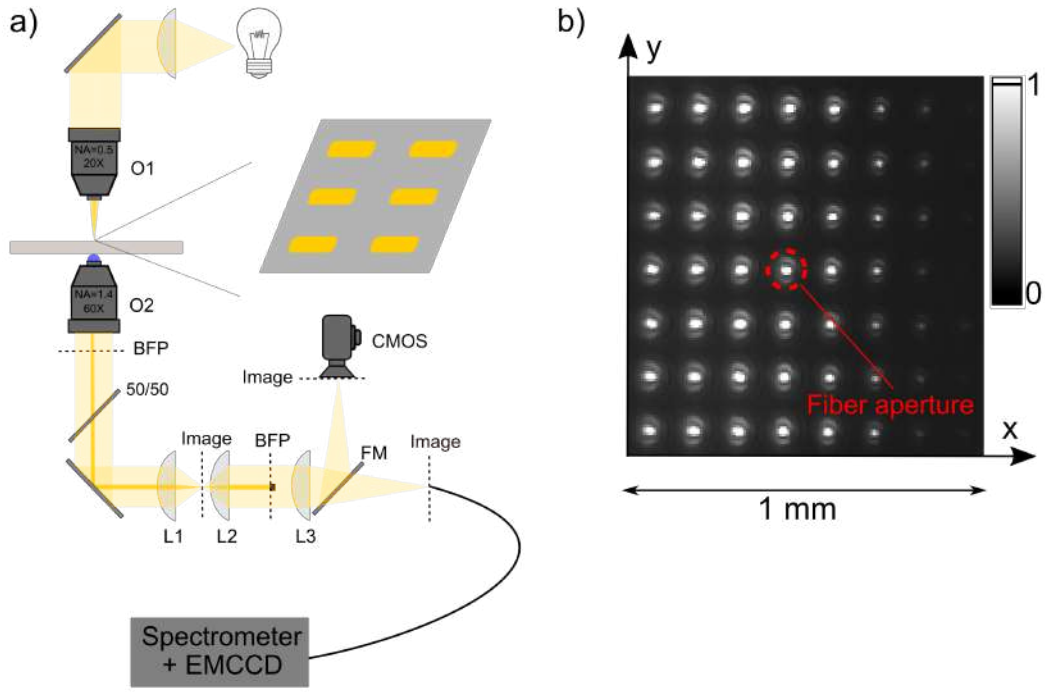

Figure 2.2: Illustration of the dark-field microscope. a) The sample is illuminated from above by a broadband thermal light source through objective 1 (O1), after which scattered and illumination signal are captured by the oil immersion objective 2 (O2). After relaying the image of the back focal plane of the oil immersion objective by lenses L1 ($f = 300mm$) and L2 ($f = 250mm$), illumination light can be filtered out and only scattered signal remains, which is imaged by lens L3 ($f = 150mm$) in wide-field configuration or spectrally characterized by choosing the imaging path with the flip mirror (FM). b) Dark-field image of an antenna array.

are all captured by a high NA (Nikon, Plan-apo 60X / $NA = 1.4$) oil immersion objective. In this configuration, it is possible to filter out the illumination light by positioning a beamstopper in the back focal plane of the oil immersion objective. This would indeed result in a dark-field image of the sample. However, precious fluorescence signal will in that case also be blocked by the beamstopper. Regarding the photon-counting nature of fluorescence signal this is an unacceptable compromise. What is done in the set-up instead is to recreate the image of the back focal plane at a location that does not overlap with the fluorescence channel. 2 lenses (Thorlabs, achromatic doublet, B coated), which are creating a relay imaging system are therefore used. Now the beamstopper can be positioned in the relayed back focal plane of the objective and such only scattered light is passed through. The scattered light is finally imaged in wide-field configuration onto a complementary metal oxide semiconductor (CMOS) (Thorlabs) camera by a final imaging lens (Thorlabs, achromatic doublet, B coated). Focal lengths of the lenses are depicted in figure 2.2

To spectrally characterize nanostructures, light from an individual structure can be guided to a multimode fiber as well. This fiber is then connected to a spectrometer with electron multiplying charged coupled device (EM-CCD) camera (Andor Shamrock 303i). Scattering spectra of individual nanostructures can thus be acquired. This is done by positioning the imaged point spread function (PSF) of the scatterer exactly in the aperture of the fiber with the aid of the nanopositioning piezo. Switching between the wide-field image and spectrometer configuration is done by using a flip mirror.

It should be taken into account that individual scatterers cannot be too close to each other, as the PSF of two individual structures can in that case overlap in the fiber aperture, which will then give the averaged spectrum of two nanostructures. To avoid these complications, the minimum distance which two scatterers should have is calculated as follows. Assuming the diffraction limit as calculated in the previous section, the PSF of a nanoscatterer will be roughly 300 nm in diameter. Now, the total magnification of the imaging system, taking into account all lenses and the objective, is roughly 53X. The imaged PSF thus has a diameter of roughly 20 μm. As the fiber aperture is 50 μm in diameter, this would mean that adjacent PSF's have to be at least 30 μm centre to centre distance apart in order not to give overlapping signals. In the sample plane, this corresponds to a distance of at least 0.6 μm in between scatterers.

2.1.3 Fluorescence microscopy

The final part of the setup is the fluorescence channel, where emitters are spectrally characterized. The principle is similar to the scanning confocal part of the setup. A CW laser source excites emitters to a higher energy state, after which they relax back to the ground state under emission of a redshifted photon. This fluorescence signal is collected by the oil immersion objective and filtered from the excitation light by a longpass filter. Finally the signal is focused onto a fiber aperture and send to a spectrometer with EM-CCD. The difference between the scanning confocal channel and the fluorescence channel is thus that in the former, an APD was positioned in the image plane, whereas in the latter a fiber.

The same multimode fiber is used for directing the dark-field scattering signal and fluorescence signal to the spectrometer. Switching between channels thus means coupling the fiber to the desired channel.

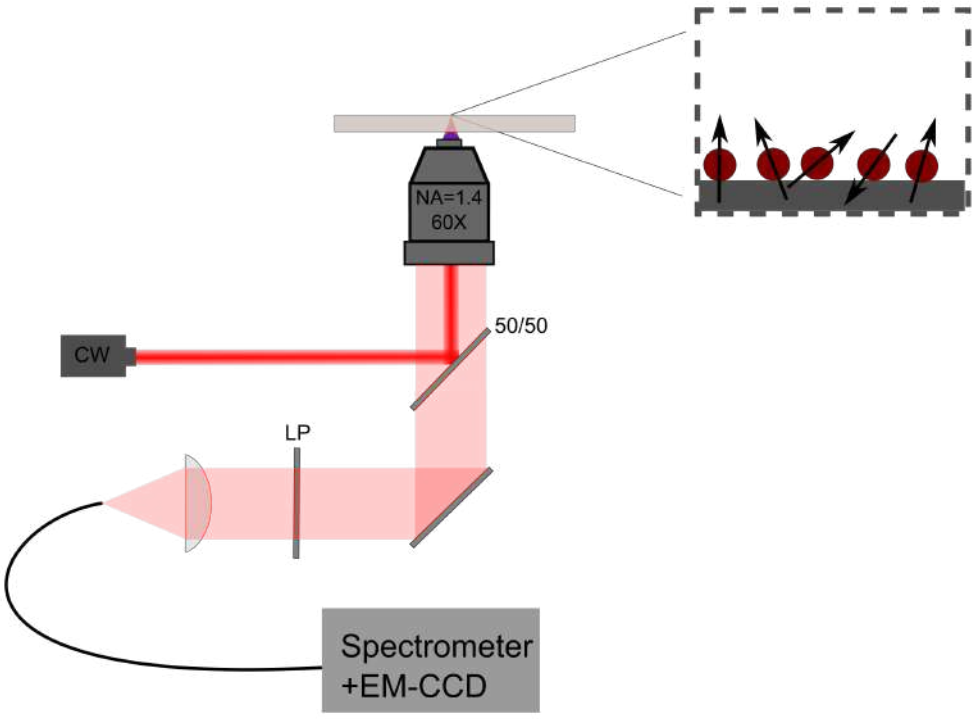

Figure 2.3: Fluorescence channel of the total setup. Emitters are excited by a CW laser source after which fluorescence signal is captured by an oil immersion objective and finally imaged onto a fiber aperture. The signal is send to a spectrometer with EM-CCD camera.

Single emitter sensitivity

The fluorescence channel is highly sensitive and able to capture the fluorescence signal down to the single emitter level, which is illustrated in figure 2.4. Here, the signal of a single carboxyl quantum dot (Qdots 800 ITK) is captured. Figure 2.4a shows the fluorescence signal as a function of time as captured on the APD. Single step blinking of signal is appreciated, confirming the presence of a single emitter in the diffraction limited spotsize. This single emitter signal is spectrally characterized, where the spectrum is shown in figure 2.4b. In the acquisition of this spectrum, the signal was integrated for 10 s. The sharp cut-off in spectrum at roughly 730 nm is due to the longpass filter, which filters out the excitation signal.

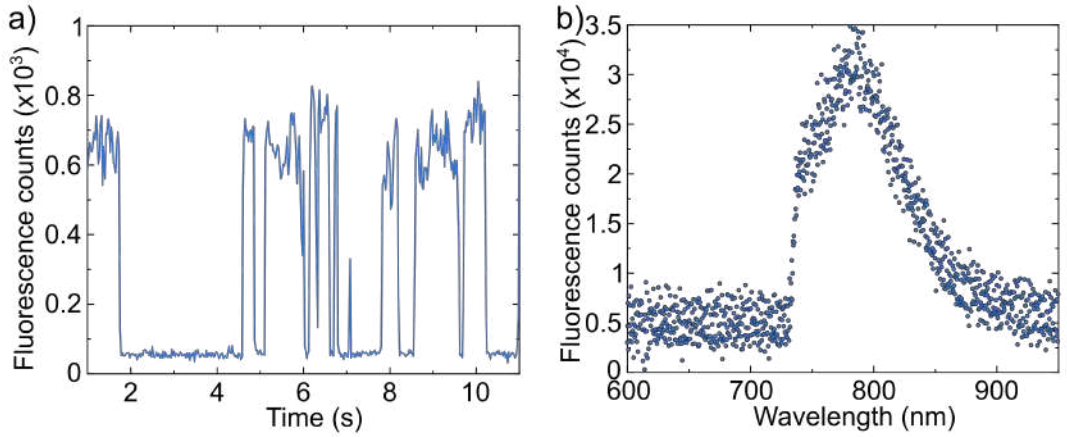

Figure 2.4: Illustration of single emitter sensitivity. a) Blinking of a single quantum dot. b) Fluorescence spectrum of a single quantum dot. Here, the signal is integrated for 10 s.

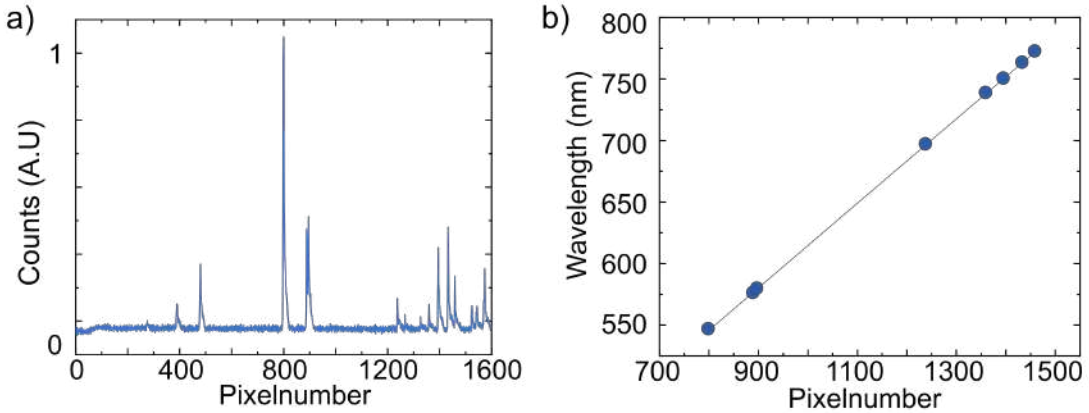

Figure 2.5: Spectrometer calibration. a) Mercury and argon atomic lines. b) Wavelength of the peaks as a function of their pixel position in the EM-CCD camera.

Spectrometer calibration

For correct spectral characterization of the signal, the spectrometer is calibrated using a mercury-argon lamp. Specific atomic lines in mercury and argon lead to well defined peaks in the spectrum,

of which the wavelengths are known. On the EM-CCD camera, these peaks will appear at different pixel positions. In the calibration, we want to assign a wavelength to each pixel position. In figure 2.5a, the peaks as a function of pixel position are shown. The known wavelengths of these peaks are then plotted as a function of their pixel position in figure 2.5b. As a calibration function, a polynomial of order 2 is assumed:

$$\lambda(p) = C_0 + C_1 p + C_2 p^2, \tag{2.2}$$

where p is the pixel number. Fitting of the polynomial through these points gives the following values for the fitting parameters: $C_0 = 256 \pm 23$, $C_1 = 0.37 \pm 0.04$ and $C_2 \approx 0$

2.2 Nanofabrication techniques

The samples fabricated in this project are subject to extremely delicate nanofabrication procedures, of which the techniques will be discussed in this section. We will start the discussion with the two main fabrication techniques applied in this work: electron beam lithography and material deposition, followed by a detailed description of a full sample fabrication cycle.

2.2.1 Electron beam lithography

Electron beam lithography (EBL) [45] is a technique used to create extremely high resolution patterns on a substrate. First, a substrate is covered with a material that is chemically sensitive to electrons, called the resist. An electron beam is now focused onto the substrate with the use of electrostatic lenses, altering the solubility properties of the resist. This exposed area can then be chemically removed, leaving only the area which was exposed to the electron beam. A sketch of the working principle is given in figure 2.6a.

Two general types of resists can be distinguished. In the positive resist, the electron beam alters the chemical properties of the exposed area from insoluble to soluble, whereas in a negative resist the opposite result is obtained. These two types of resist techniques are depicted in figure 2.6c.

Resolution

Similar to photons, electrons are waves to which a wavelength can be assigned. The spot size of the focused electron beam is therefore also limited to the diffraction limit.

For electrons, the wavelength can be determined by the de Broglie relation:

$$\lambda_e = \frac{h}{m_e v_e} = \frac{h}{\sqrt{2 m_e e V}}. \tag{2.3}$$

Here, λ_e is the electron wavelength, h is Plank's constant, m_e and v_e the electron mass and velocity respectively, e the elementary charge and V the acceleration voltage. It is assumed here that the electrons are accelerated from a starting velocity of 0 m/s without any dissipation. Using a typical acceleration voltage of 30 kV, this gives an electron wavelength of approximately 0.007 nm. Thus it would seem that the resolution of EBL is well below the nanometer lengthscale.

Diffraction, however, is not the main limitation of this technique. As electrons strike the substrate, scattering events broaden the exposed area significantly. This effect is depicted in figure 2.6b. Also, initial electrons can dissipate their energy by creating high energy secondary electrons. All these proximity effects degrade the actual resolution of EBL to approximately 10 nm.

2.2.2 Focused ion beam lithography

In order to create features in nanostructures with a higher resolution than that of EBL, a technique called focused ion beam (FIB) lithography can be applied. The principle, sketched in figure 2.7a, is

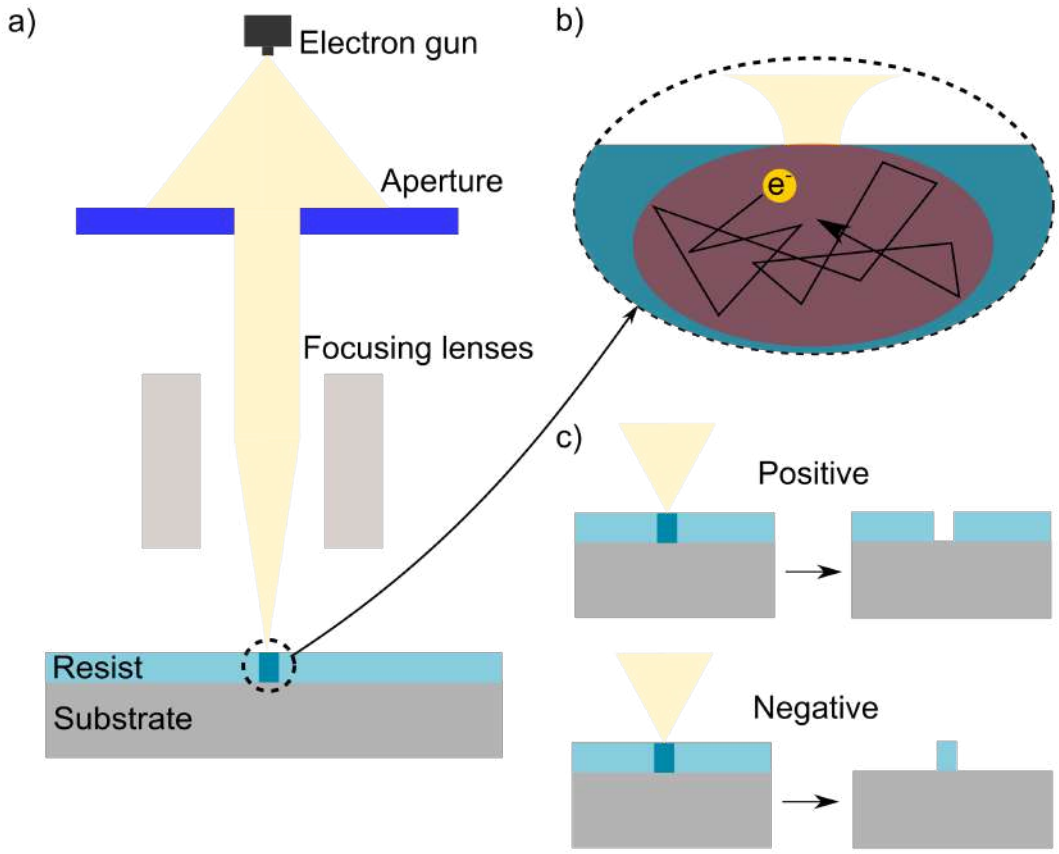

Figure 2.6: Working principles of electron beam lithography. a) An electron beam is focused with high resolution onto the sample covered with a resist, altering the solubility of the resist. b) Proximity effects of scattered electrons broaden the exposed area, degrading the resolution. c) Principles of positive and negative resist EBL.

similar to that of EBL. A helium ion source creates a beam of helium ions, which are subsequently focused onto the desired sample. This focused beam of ions can then physically remove material in the nanostructures and is thus used as a milling tool to create the desired high resolution features. The ions are created by an ionization disk as shown in figure 2.7b, which ionizes neutral helium atoms. The advantage of using a helium FIB with respect to EBL is its higher resolution. As mentioned in the previous section, the resolution of EBL is limited by secondary electron scattering events, which widen the exposed area dramatically. These events are, however, less pronounced in the case of a focused beam of helium ions in the first few nanometers [35] and therefore a higher resolution is obtained. The sample interaction of a focused beam of helium ions is shown in figure 2.7c, which is compared to the interaction of a focused beam of electrons.

Besides the milling of high resolution features in nanostructures, Helium-ion microscopy finds applications in high resolution imaging [9].

2.2.3 Material deposition

Antenna structures will be created by evaporation of the desired material onto the sample. A sketch of the evaporation process is shown in figure 2.8a. A target material contained in a crucible is heated, after which the evaporated material condenses onto the substrate. The material deposition rate is recorded and controlled by a quartz crystal monitor (QCM), which oscillates at a defined

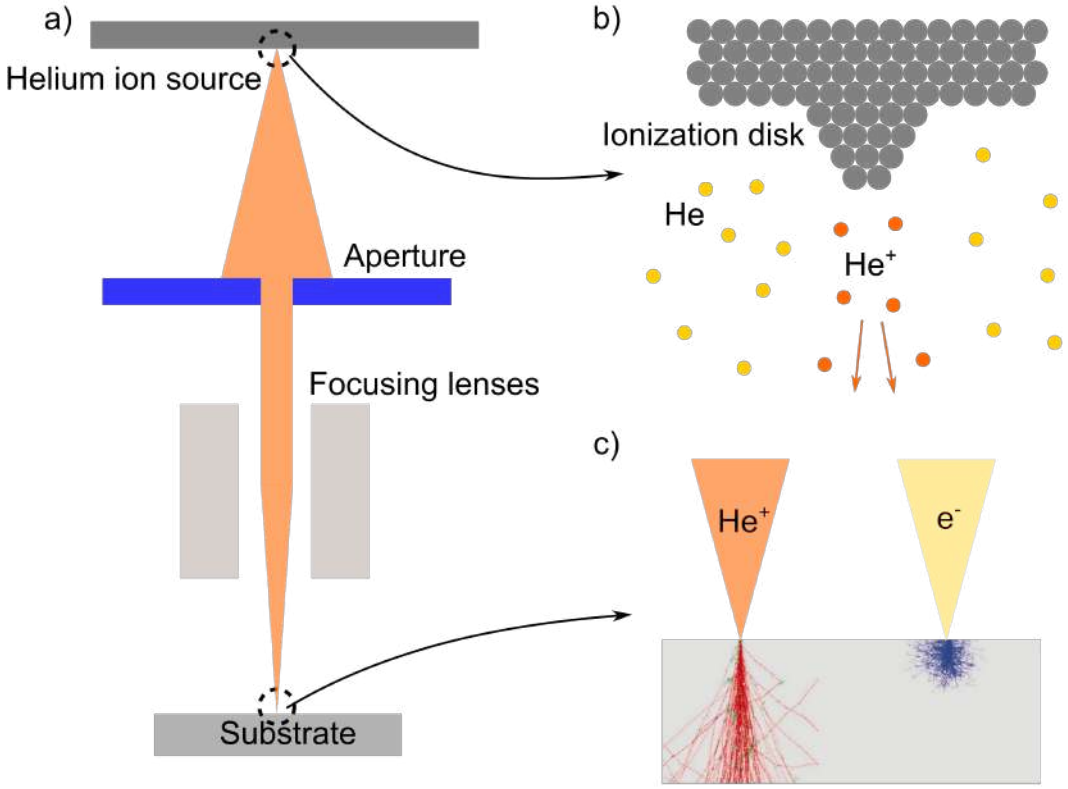

Figure 2.7: Illustration of helium ion focused ion beam lithography. a) General sketch of the helium FIB. b) An ionization disk ionizes the surrounding neutral helium atoms. c) Monte-Carlo simulations (performed by [35]) of the interaction of a silicon substrate with a focused beam of helium ions and electrons (both accelerated by a 30 keV voltage).

frequency by applying an appropriate voltage. The oscillation frequency is subsequently affected by any minuscule mass change in the QCM and thus the deposition rate can be accurately recorded.

Thermal versus e-beam sources

Two kinds of heatsources are mainly used in material evaporation. First, there is the electron beam (e-beam) source, depicted in figure 2.8b. Here, an electron beam is directed onto the material. Kinetic energy of the incoming electrons is converted into heat, causing the target material to be evaporated or sublimated. Finally, there is the resistive thermal evaporation, illustrated in figure 2.8c. Here, the heatsource is provided by energy dissipation in a current conducting channel. Usually, thermal evaporation is used when low melting point materials, such as aluminum or gold, are required. For higher melting point materials, such as metal-oxides, the resistive thermal source is not sufficient and e-beam evaporation is preferred, as the high energy e-beam can be focused on a small spot.

2.2.4 Sample fabrication

Now, we are in a position to discuss in detail all the steps of top-down nanofabrication of an antenna array. First, silicon dioxide substrates are thoroughly cleaned by ultrasonication in subsequently

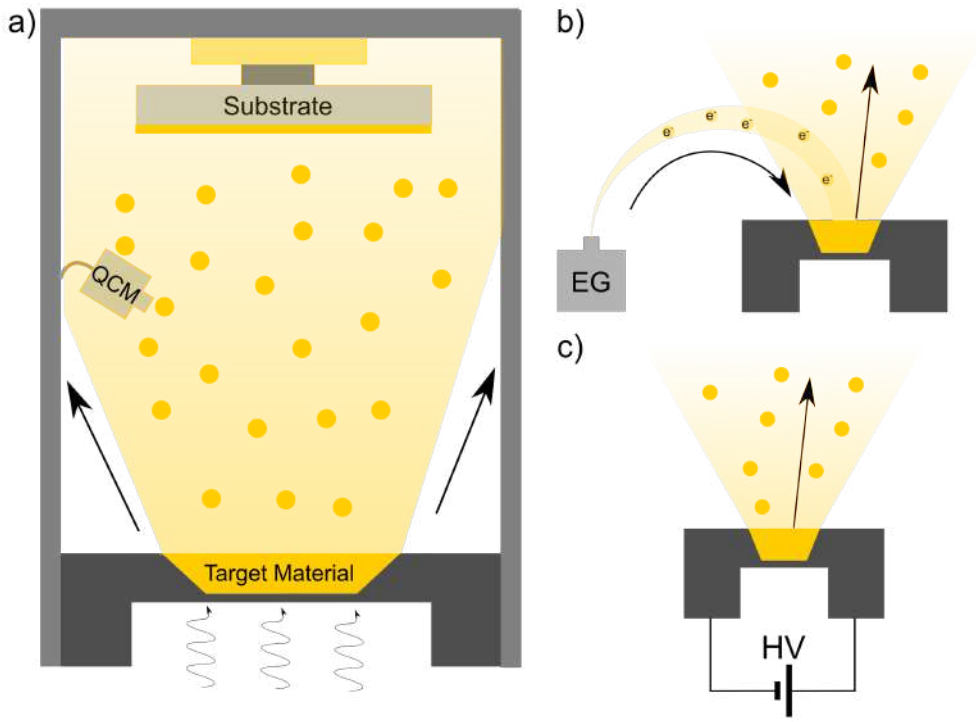

Figure 2.8: Principles of material vapor deposition. a) Heat is added to a target material, which evaporates or sublimates. Material vapor subsequently condensates onto the substrate. Deposition rates are accurately controlled by a quartz crystal monitor (QCM). b) E-beam evaporation: An electron gun (EG) directs electrons onto the target material, where electron kinetic energy is converted into heat. c) Thermal evaporation: heat is now obtained from energy dissipation of a resistive material connected to a high voltage (HV) source.

acetone, ethanol and miliQ water, after which the samples are blown dry with a nitrogen gun. Then, an ultrathin 9 nm layer of indium-tin-oxide (ITO) is deposited onto the substrates by e-beam evaporation with a deposition rate of 2 Å/s. The pressure in all deposition processes was kept below 10^{-6} $mbar$. After the deposition, the ITO covered substrates are baked on a hot plate for approximately 5 minutes with 350 °C . The ITO layer forms an adhesion layer for the gold to bind to. Also, the layer is conducting and thus provides an electrical ground, avoiding charge accumulation in EBL processes.

The substrates are now ready for EBL patterning. A layer of positive resist polymethyl methacrylate (PMMA) is spincoated on the ITO covered substrates with 2000 rpm for 2 minutes. After baking the PMMA covered samples on a hot plate with 150 °C for 2 minutes, the desired structures are patterned with EBL. In all EBL processes, the acceleration voltage was set to 30 kV with an e-beam current of 0.04 nA. After patterning, the samples are developed by immersion in subsequent solutions of methyl isobutyl ketone/isopranol (MIBK/IPA) (1:3) and IPA for 45 and 75 s respectively and blown dry with nitrogen.

Next, a 50 nm layer of gold is deposited onto the sample by thermal evaporation, with a deposition rate of 2 Å/s. Finally, a lift-off process is performed by placing the sample in acetone (50 °C) for approximately 2 hours. A small square around the nano antennas is scratched with tweezers in order for easy entry of the acetone. Excess gold is then easily pipetted off, leaving only the patterned structures on the substrate. A full illustration of the fabrication cycle is depicted in figure 2.9.

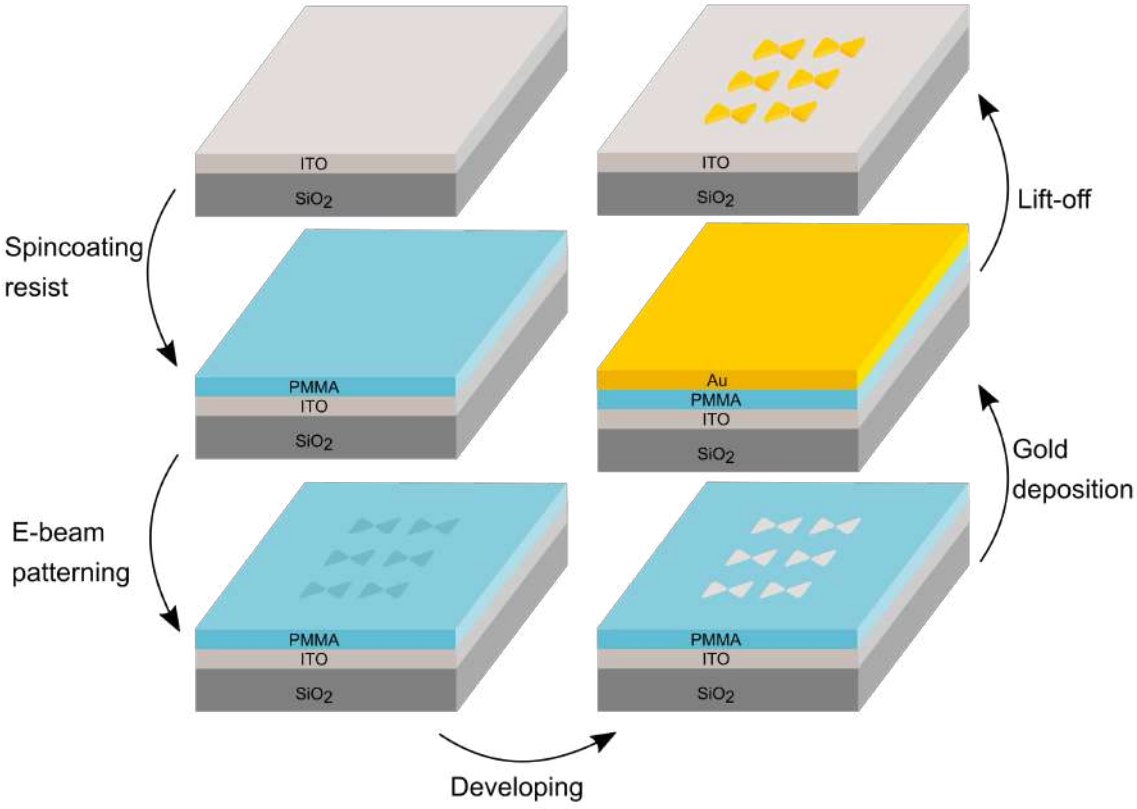

Figure 2.9: Illustration of all steps in a nanofabrication cycle.

Chapter 3

Electromagnetic simulations

In order to investigate the optical response of plasmonic antennas and thereby to engineer their design to fulfil optimal properties, 3 dimensional Finite Difference Time Domain (FDTD) [19] [57] electromagnetic simulations are performed. This state-of-the-art technique offers a direct method in calculating a broad spectrum of optical phenomena, ranging from scattering spectra to field profiles. First, a general introduction to the technique is set out, after which simulation design and preliminary results of plasmonic rod antennas are discussed. In this thesis, the commercial FDTD package "Lumerical" is used in all simulations.

3.1 Introduction

The FDTD method solves the time dependent Maxwell curl equations in every point of a predefined spatial and temporal grid:

$$\frac{\partial \vec{E}}{\partial t} = \frac{1}{\epsilon} \nabla \times \vec{H} \tag{3.1}$$

$$\frac{\partial \vec{H}}{\partial t} = \frac{-1}{\mu} \nabla \times \vec{E}, \tag{3.2}$$

where $\vec{E}$ and $\vec{B}$ are the electric and magnetic fields respectively, μ the permeability and ϵ the permittivity. In order to simulate a finite area, the discretized forms of equations 3.1 and 3.2 need to be solved in this grid. The 1 dimensional discretized versions are given in the central difference scheme (with second order accuracy) as follows:

$$\frac{E_x^{n+1/2}(k) - E_x^{n-1/2}(k)}{\Delta t} = \frac{-1}{\epsilon} \frac{H_y^n(k+1/2) - H_y^n(k-1/2)}{\Delta z}, \tag{3.3}$$

$$\frac{H_y^{n+1}(k+1/2) - H_y^n(k+1/2)}{\Delta t} = \frac{-1}{\mu} \frac{E_x^{n+1/2}(k+1) - E_x^{n+1/2}(k)}{\Delta z}. \tag{3.4}$$

Here, n and k are the number of steps in time and space respectively, with Δt and Δz the corresponding stepsizes. Electric and magnetic field components are thus calculated according to the following algorithm:

$$E_x^{n+1/2}(k) = E_x^{n-1/2}(k) - \frac{\Delta t}{\epsilon \Delta z}(H_y^n(k+1/2) - H_y^n(k-1/2)) \tag{3.5}$$

$$H_y^{n+1}(k+1/2) = H_y^n(k+1/2) - \frac{\Delta t}{\mu \Delta z}(E_x^{n+1/2}(k+1) - E_x^{n+1/2}(k)). \tag{3.6}$$

Each electric field component is thus calculated from the previous electric field component plus an additional contribution from the most recent magnetic fields and vice versa. Besides, it is seen

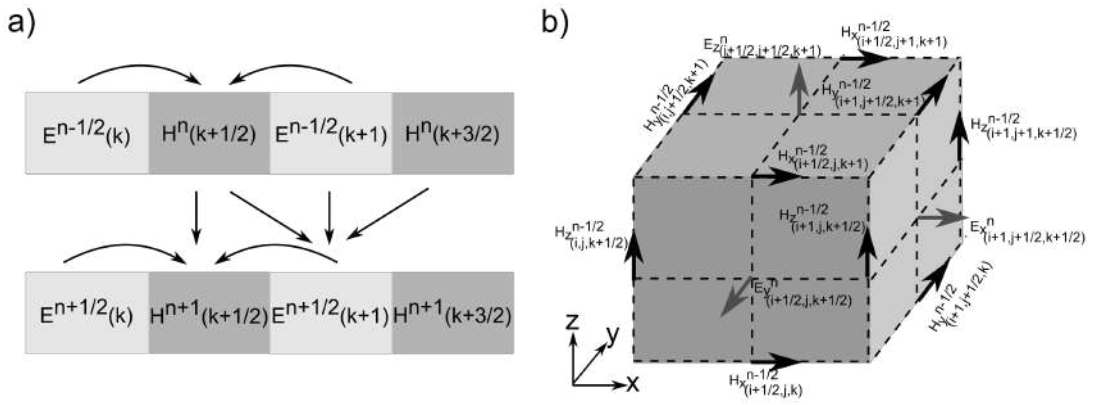

Figure 3.1: Illustration of the FDTD principle in a) 1 dimension and b) 3 dimensions.

that electric (and magnetic) field values are interleaved, that is, located in between each other, between the most recent and most proximate magnetic (and electric) field values in both space and time, as illustrated in figure 3.1a.

The one dimensional idea given above can be expanded into the third dimension, where the 1 dimensional strip as given in figure 3.1a now becomes a 3 dimensional box depicted in figure 3.1b. Again the magnetic and electric fields are interleaved, where it is additionally observed that the magnetic and electric fields circulate around each other. The curl relations are thus directly depicted. This 3 dimensional iterative scheme for solving Maxwell's equations is called Yee's algorithm [68].

3.1.1 Perfectly matched layer

Suppose the computational region is an infinite space: sources inject electromagnetic radiation, which can be scattered by any non-homogenous media inside the region and all fields are simply calculated according to Yee's algorithm. In practice, however, there should be an upper bound on the computational time and thus on the computational region. The transition from an infinite space to a finite region, however, is not trivial and may introduce artifacts. When a computational region is truncated by for example Neumann or Dirichlet boundary conditions, which can be viewed as solid walls, incident radiation will be reflected back into the simulation region, causing unacceptable modifications of the solutions as shown in figure 3.2a. This is especially true for slow decaying solutions. For rapidly (exponentially) decaying solutions, the reflections will impose only minor distortions. Absorbing boundary conditions (ABC) could instead be used to minimize the unwanted reflections, but are still limited to the efficient absorption of waves at specific angles only. It is noted that structures where periodic boundary conditions may be applied will be naturally truncated, and reflections will not cause artifacts.

Rather than using boundary conditions, it was shown that the truncation area of a simulation region could be covered by an absorbing material and hence minimize reflections. The consequences were that the reflections indeed were minimized at the truncation boundaries, but that new reflections were introduced at the interface of the absorbing layer. In 1994, Bérenger showed [7] that a particular absorbing material could be used which has *zero* reflections at the interface. This is called a perfectly matched layer (PML). The PML transformed FDTD simulations into a highly effective method and still is the most robust option of truncating a simulation region to this day. The application of a PML in FDTD simulations is shown in figure 3.2b.

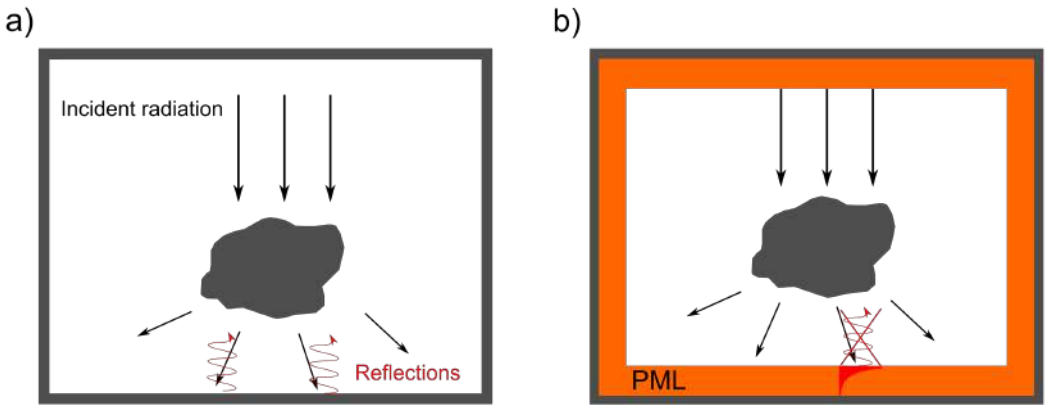

Figure 3.2: Application of a PML in FDTD simulations. a) A truncated simulation region will cause reflections and thus artefacts in the simulation. b) A PML covers the simulation boundaries, minimizing reflections.

3.1.2 Symmetries

Depending on whether the computational region has planes of symmetry, computational time may be significantly reduced by applying (anti)symmetric boundary conditions. This depends on source injection, source polarization and geometry of the structure. (Anti)symmetric boundary conditions mirror the field solutions of one specific halfspace, therefore reducing the effective simulation region and thereby computation time.

In order to correctly apply symmetries in an optical simulation, careful consideration of the vector components of the electric and magnetic fields must be taken into account. Suppose the simulated region has a plane of symmetry, as indicated by the red lines in figures 3.3a and b. Now, due to the symmetry, particular field components must be set to zero at the plane of symmetry. In a symmetric simulation for example, the electric field component normal to the plane of symmetry must vanish, whereas in an anti-symmetric simulation the tangential electric field component vanishes. This principle is indicated in figure 3.3a. Similar symmetry rules for the magnetic field components (indicated by green arrows) are shown in figure 3.3b. Finally, an example of the correct application of symmetries in a FDTD simulation is depicted in figures 3.3c and d.

3.1.3 Total field scattered field source

In the simulations, a special geometry is applied in order to mimic the experimental conditions, where only the dark-field scattered signal of a nanostructure is captured. In this geometry, we will make use of the total-field-scattered-field (TFSF) source. The working principle of this source is shown in figure 3.4. A broadband pulse of plane wave radiation is injected into an area bounded by the blue dashed line as shown in figure 3.4a. Light will scatter of the nanostructure as the excitation radiation strikes the structure. However, excitation signal will still be present in the total signal. The TFSF source, however, is able to filter out the excitation signal and thus only scattered signal of the nanostructure will leave the blue dashed box. More specifically, the TFSF source will subtract any radiation at its boundaries which is transmitted through the source region or reflected from a flat substrate from the total radiation. As such, it is essential that a scattering object is positioned completely inside the TFSF boundaries. In figure 3.4b, the effect of the TFSF source is highlighted, where light is scattered of a gold sphere with a radius of 500 nm. Inside the TFSF boundaries, fringes are observed which are caused by the interference of excitation and scattered signal. Outside this area, the fringes disappear as the excitation signal is filtered out.

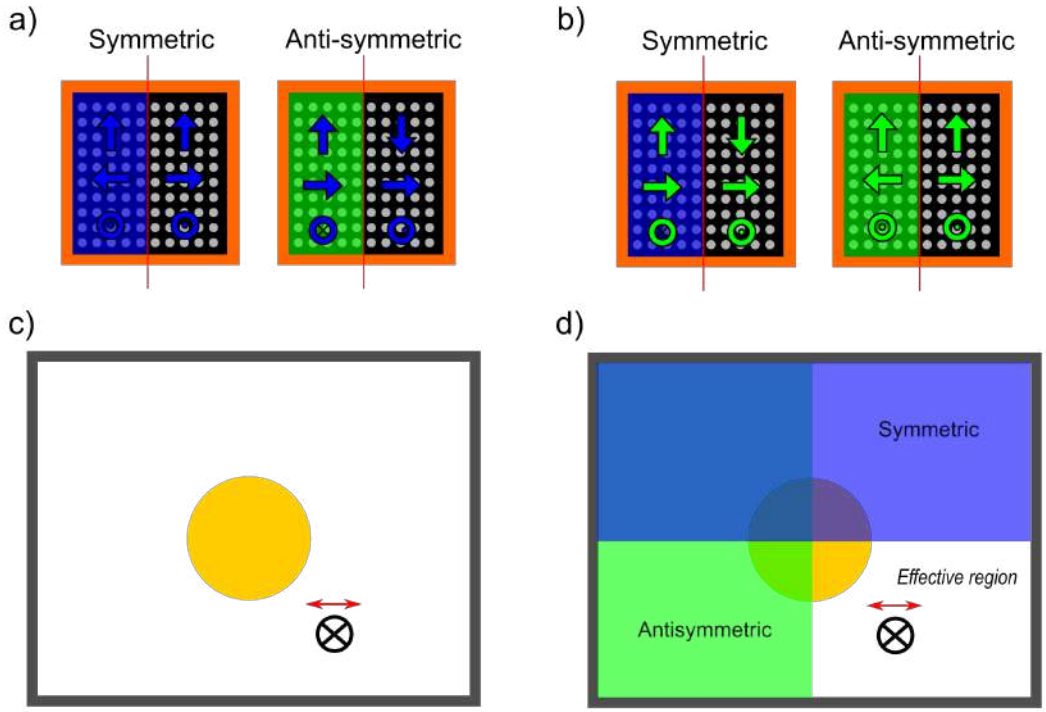

Figure 3.3: Application of symmetric (blue) and anti-symmetric (green) boundary conditions in an optical simulation. Effect of the applied symmetries on the a) electric (blue) and b) magnetic (green) field components in the simulation. c) Simulation without symmetries. d) Simulation with correct application of symmetries, mimicking the simulation of c) while reducing the simulation time. The red arrow shows the direction of polarization of the electric field component of the injected radiation. Figures a) and b) adapted from [58]

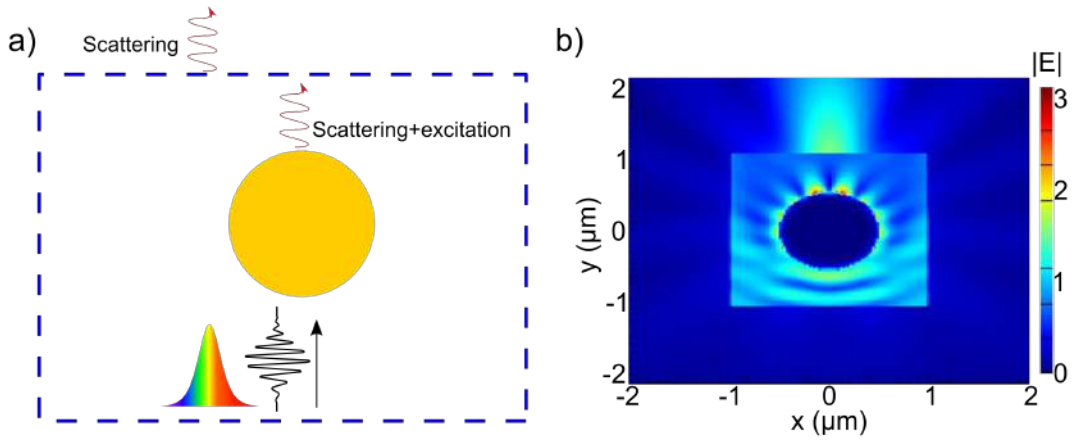

Figure 3.4: Principle of the total-field-scattered-field source. a) A broadband plane wave pulse of radiation is injected in the area bounded by the blue dashed area. This area will filter any excitation light of the total signal that passes this area. b) Effect of the TFSF source when light is interacting with a gold nanosphere.

3.2 Rod antenna simulations

Now that the general principles and techniques of FDTD simulations are introduced, we move on to a more detailed description of the simulations conducted in this thesis. The fundamental plasmonic structure used in this thesis is that of the nanorod. Here, an emphasis is set on general geometrical considerations of the nanostructure and signal collection.

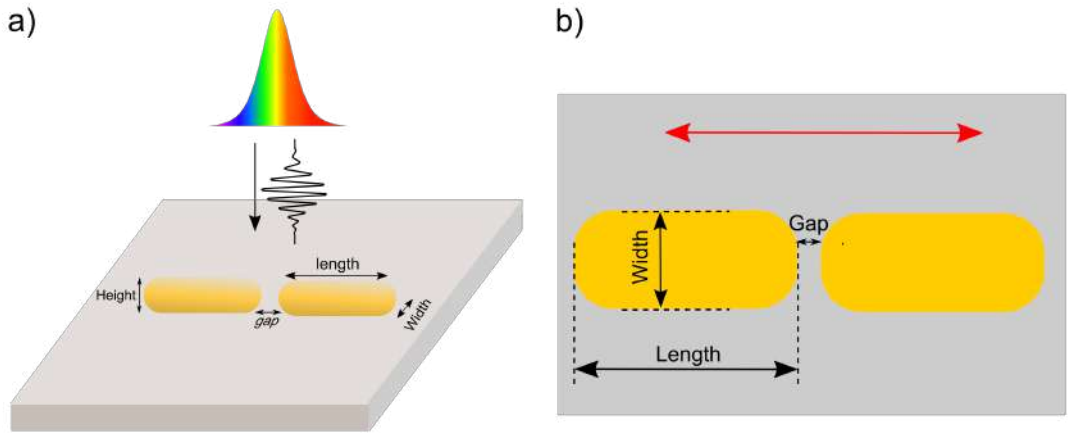

Figure 3.5: General description of all rod antenna simulations. a) A broadband pulse of radiation is injected normally from above onto the structure. b) Top view of the antenna geometry with corresponding controllable parameters. The red arrow indicates the main direction of the polarization.

3.2.1 Simulation design

In figure 3.5a the general design of all simulations is depicted. A broadband (400 - 1100 nm) pulse of TFSF linearly polarized electromagnetic radiation is injected from above under normal incidence onto an antenna structure, which consists of a gold rod antenna on top of an ITO covered silicon dioxide substrate. The polarization of the incident pulse is oriented along the longitudinal antenna axis, unless otherwise stated, in order to excite relevant antenna modes. The substrate is 3000 nm long, 3000 nm wide and 2000 nm thick and can therefore be considered as an infinitely extending plane with respect to the nano antenna. Material properties of gold and silicon dioxide are fitted according to Johnson and Christy's [27] and Palik's [41] data respectively. Controllable antenna parameters such as height, width, length and gap are depicted in figure 3.5b. In order to mimic experimental conditions, which will be more elaborately discussed in chapter 4, all edges of the rods in the simulations are rounded.

3.2.2 Field and power monitors

In order to investigate the scattering cross sections of the antennas, planar monitors that record the power flux of electromagnetic radiation in the frequency domain are positioned as illustrated in figure 3.6a. Here, the planar power flux monitor, indicated in red, is positioned below the sample. This is done to mimic the collection objective in the dark-field microscope, which collects scattered signal from below the structures as well. The monitor is placed outside the TFSF boundaries and thus only the scattered antenna signal strikes the monitor. This collected scattered signal can then be optically characterized as to obtain a simulated scattering spectrum. Scattering spectra of rod antennas with different geometries will be extensively discussed in the next chapter.

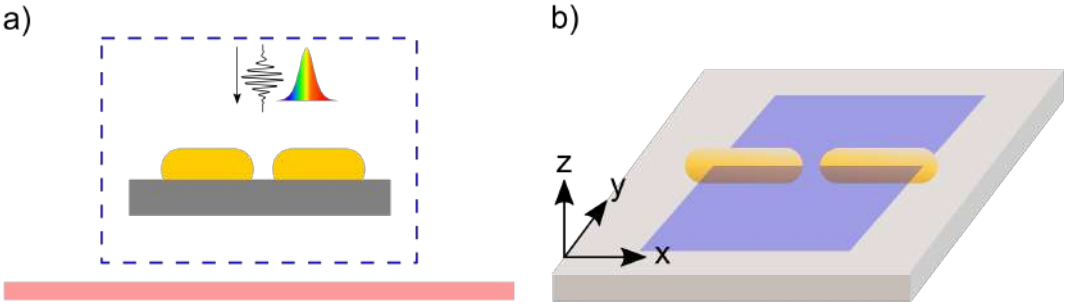

Figure 3.6: Illustration of the types of monitors used in all simulations. a) A power flux monitor (red) placed below the antenna structure is able to record antenna scattering spectra. b) Positions of a field monitor normal to the z-direction, able to record field profiles surrounding an antenna.

Besides scattering spectra, electric field profiles provide crucial information about the electromagnetic environment surrounding a nanostructure, such as field enhancements and confinement of hotspots. These are recorded using 2 dimensional field profile monitors. The geometry and position of such a monitor is shown in figure 3.6b, where a monitor with a normal in the z direction is used.

3.2.3 Electric field profiles

To conclude this chapter, the electric field profiles surrounding rod nanostructures are investigated. In these simulations, the absolute value of the x-component of the electric field is calculated for different geometries. These electric field values are then normalized to the field value of a reference simulation, without the presence of the nanostructure. First, the normalized field surrounding a single gold rod antenna is shown in figure 3.7a, where the rod antenna is excited at resonance. The length and width of the rod are set to 100 and 50 nm respectively. Two electric field hotspots are observed near the end of the rod, decaying rapidly as the distance from the antenna is increased.

In figure 3.7b, the simulation is repeated for the case of a rod dimer structure, where the lengths and widths of the separate rods are again set to 100 and 50 nm respectively. Furthermore, both rods are separated by a gap of 10 nm. The two hotspots at the end of the dimer structure are again observed, accompanied with an intense hotspot in the gap between the two rod antennas. This enhancement of electric field in the gap is a consequence of the reduced mode volume, which increases the spatial energy density of the electric field and thereby the amplitude of the electric field as well. Smaller gaps are therefore expected to cause a greater electric field enhancement. The gap size dependence on electric field enhancement in the gap of a dimer antenna is depicted in figure 3.7c. Indeed, as the gapsize is decreased, the electric field enhancement in the centre of the gap is increased enormously.

These preliminary results already provide insights in the electric field profiles around rod antenna structures. Looking back at equations 1.7 and 1.8 in chapter 1, in order to achieve a high cavity-emitter coupling strength, it is desired to have great electric field magnitudes confined in corresponding small mode volume. As can be seen in figure 3.7c, a dimer structure of two rods with a small gap in between them satisfies these conditions, where smaller gap sizes induce greater electric field strengths and thus provide greater potential coupling strengths.

In the next chapter, the scattering behaviour of rod antennas is extensively discussed, where experiment and simulation are treated in parallel.

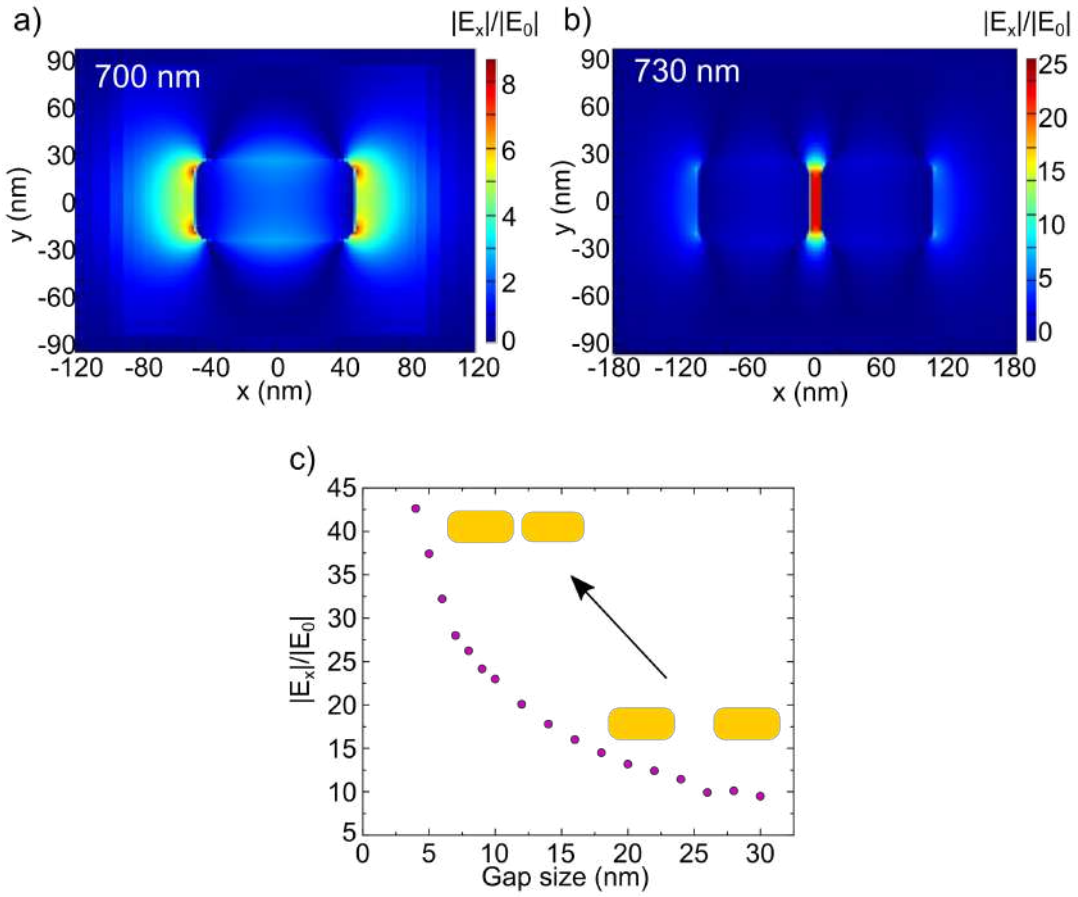

Figure 3.7: Electric field enhancement in rod antenna structures. x component of the electric field surrounding a a) rod and b) dimer antenna. In both structures, the rod lengths are set to 100 nm, while in the dimer antenna the gap between the two rods is set two 10 nm. Excitation wavelengths are shown in white. c) x component of the electric field in the gap of a dimer structure as a function of the gapsize. All electric fields are normalized to a reference electric field E_0 which is obtained in a separate simulation without the presence of the nanostructure.

Chapter 4

Nano-antenna fabrication and characterization

In this chapter, it is shown how single plasmonic nanostructures are fabricated and subsequently characterized. This is done for their geometrical structure by scanning electron microscopy (SEM) and for their optical properties by dark-field spectroscopy. Addionally, the optical behaviour is supported by finite-difference-time-domain simulations.

4.1 Gold nanorods

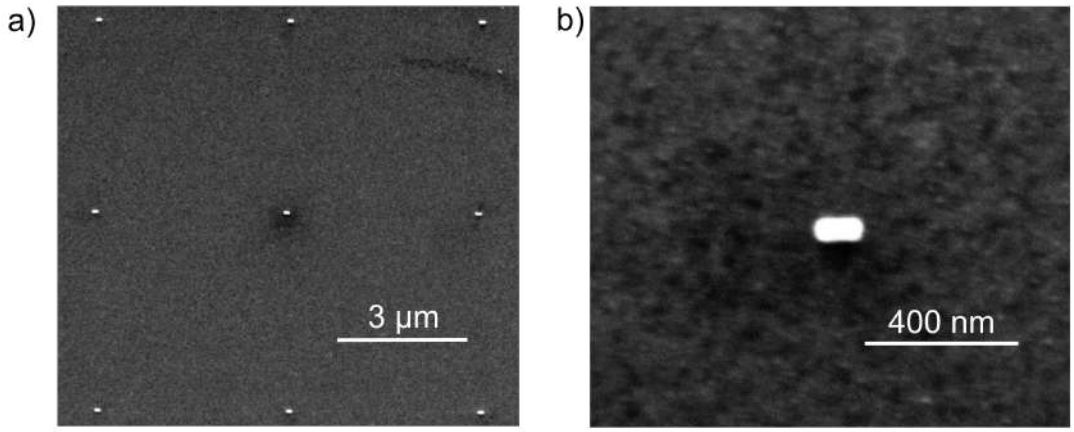

Figure 4.1: Scanning electron microscope images (HV=5 kV) of a) multiple and b) a single gold nanorod

Because of its straightforward nanofabrication procedure, we start this chapter with the characterization of isolated gold nanorods. Later in this chapter, the more complicated rod dimer is discussed. In all fabricated structures, the height and width are set to 50 nm unless otherwise stated. In figure 4.1, SEM images are shown for multiple and single gold nanorods. The designed nanorods are patterned in an array, with a distance of 4 μm between adjacent antenna structures. This distance is more than enough to ensure that scattering signal of single antenna structures is indeed captured by the multimode fiber, as discussed in chapter 2. It is pointed out that a fabricated nanorod has rounded corners, as is clearly shown in figure 4.1b, whereas the pattern

used in EBL is a rectangle with sharp 90 degree corners. This rounding of the corners is an effect of the finite resolution of the electron beam.

4.1.1 Localized surface plasmon resonances

To investigate the geometrical dependence of the gold nanorods on the localized surface plasmon resonances (LSPR) of the structures, an array of gold nanorods is fabricated in which the length of the rods is swept from smaller to greater lengths. The dark-field scattered signal of the nanostrucures in this sweep array should then be highly susceptible to different lengths.

Dark-field scattered signal is recorded for the single nanostructures, of which the raw signal is depicted in figure 4.2a. The raw spectrum of the antenna, however, has to be normalized by the profile of the light source, such that every spectral interval is treated equally. Therefore, the profile of the light source is recorded before every measurement, which is shown in figure 4.2b. Finally, the normalized scattered signal is depicted in figure 4.2c. A clear resonance is visible at roughly 740 nm, which corresponds to the LSPR of the nanorod.

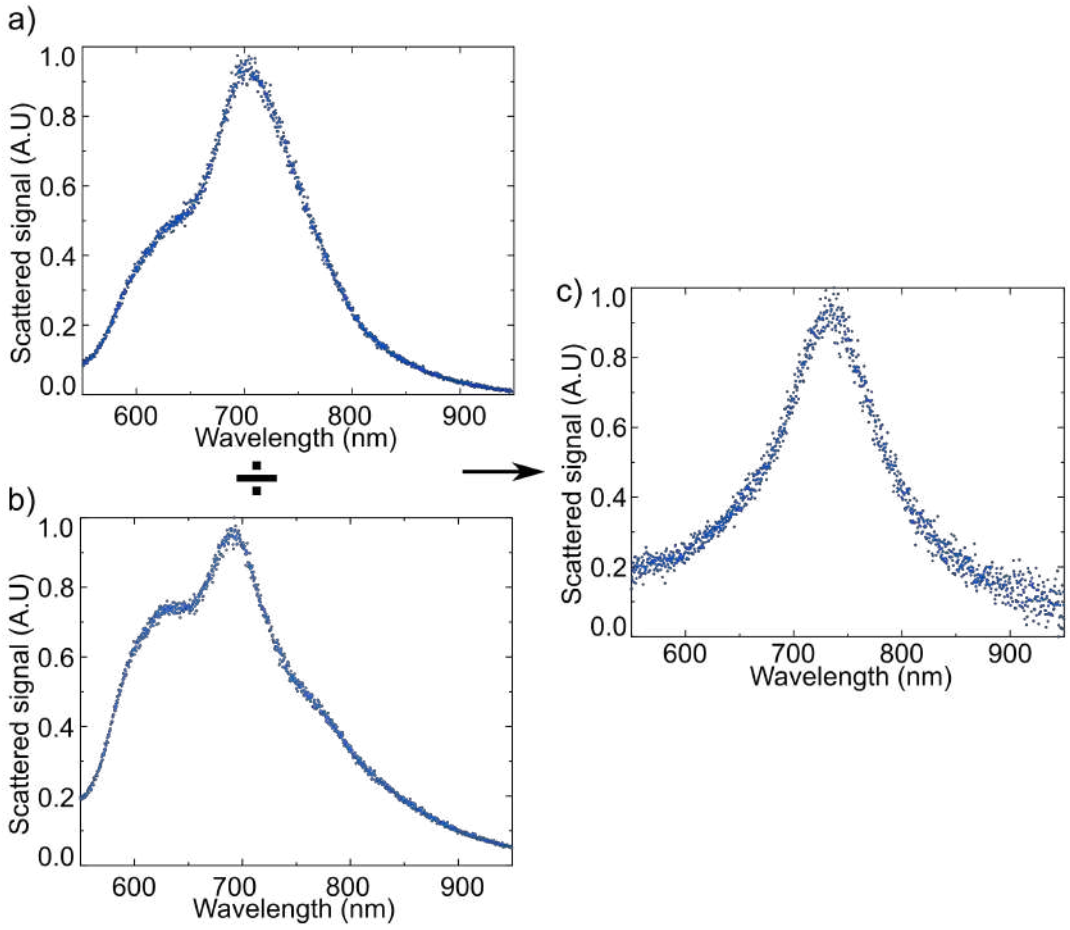

Figure 4.2: Normalization procedure of the scattered signal of a plasmonic nanostructure. a) Recorded raw spectrum of a gold nanorod. b) Spectrum of the light source used to illuminate the nanorods. c) Scattering spectrum of the nanorod after normalization of the light source profile.

Now, we are in a position to characterize the length dependence on the LSPR of the nanorods. To distinguish between longitudinal and orthogonal antenna modes, the scattering spectra are

recorded for illumination with a polarization both parallel and orthogonal to the long antenna axis. The scattered signal is shown in figure 4.3a, where the red and blue signals correspond to the orthogonal and parallel illuminations respectively. The longitudinal antenna resonance shows a clear length dependence, with an increasing resonance wavelength for increasing lengths. For longer rod lengths, the rod is able to accept longer wavelength dipolar electron oscillations, which are responsible for the redshifting of the fundamental antenna resonance. The orthogonal polarization, however, does not show any clear length dependence. As the width of the antenna is kept constant, the electron oscillations in the direction perpendicular to the long antenna axis will be confined to a constant width as well, thus ensuring a constant fundamental resonance for different lengths.

Recorded spectra are compared to FDTD simulation results, which are shown in figure 4.3b. Excellent agreement between simulation and experiment is obtained. It is noted that the simulated linewidth of the antenna resonance seems to be slightly narrower than the experimental spectral linewidths. This might be due to the fact that the simulated spectra are obtained with a plane wave excitation illuminating the structure at a perfect 90 degree angle with respect to the plane of the sample, which does not take the small angular spread in the experimental illumination caused by the 0.5 NA illumination objective into account.

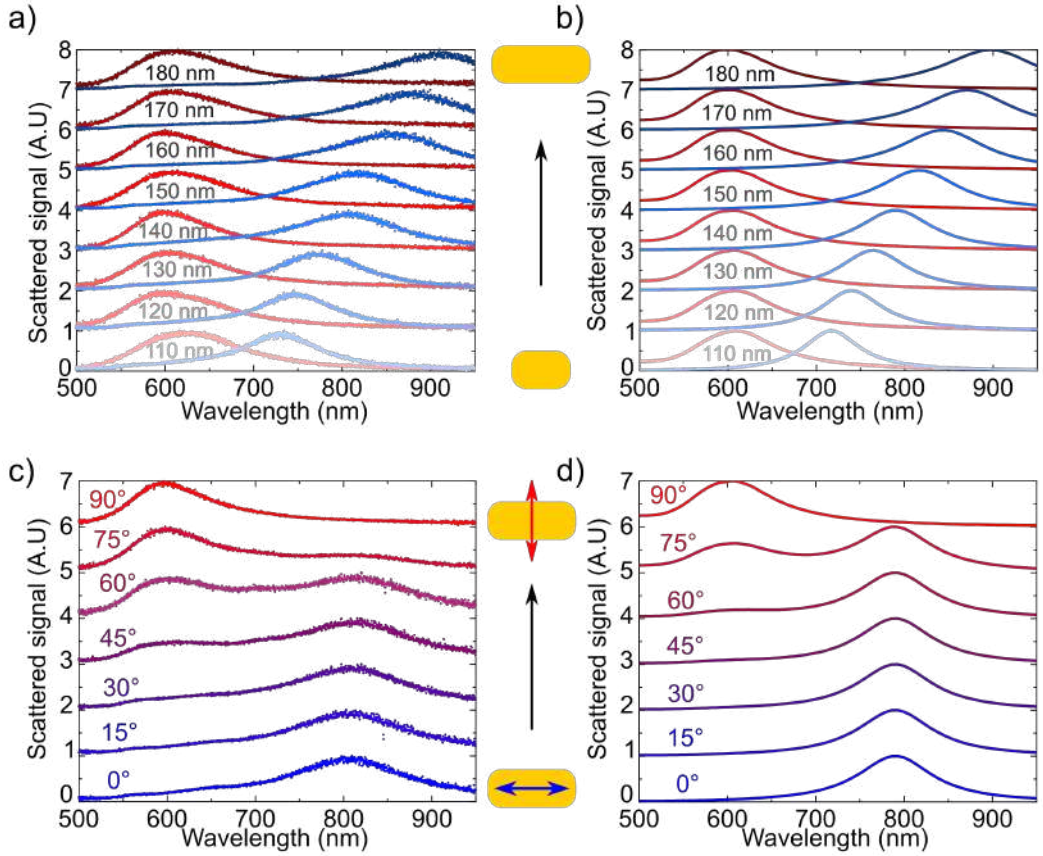

Figure 4.3: Polarization resolved dark-field scattering analysis of gold nanorods of different lengths. a) Experimental spectra of nanorods of different lengths with illumination polarization orthogonal (red) and longitudinal (blue) to the long antenna axis. b) Corresponding FDTD simulation results. c) Polarization resolved experimental scattering spectra of a single gold nanorod, where the polarization angle is swept from 0 (longitudinal) to 90 degrees (orthogonal) in steps of 15 degrees. d) Corresponding FDTD simulation results.

To investigate more closely the response of the nanorod for different excitation polarizations, the scattering spectra of one single nanorod are recorded several times for different illumination polarizations, of which the results are shown in figure 4.3c. A gradual transition between the two antenna modes is observed, where the orthogonal resonance becomes more dominant for increasing angles, whereas the longitudinal resonance slowly disappears. The experimental observations are supported by FDTD simulations, where the same behaviour is seen. The transition from longitudinal to orthogonal resonance in the simulated spectra, however, seems to lag behind the transition in the experimental spectra.

4.1.2 Statistical analysis

To shed more light on the intrinsic plasmonic properties of gold nanorods, a statistical analysis is performed over the recorded scattering spectra of many single structures. The rod antennas are from this point on illuminated with a polarization parallel to the long antenna axis. Now, the scattering spectra of a single gold nanorod are fitted by a Lorentzian function described by:

$$f(\lambda) = A\frac{\delta\lambda/2}{(\lambda-\lambda_0)^2+(\delta\lambda/2)^2} + B, \tag{4.1}$$

with A and B scaling factor and offset respectively. λ_0 and $\delta\lambda$ describe here the antenna fundamental resonance and linewidth respectively, as shown in figure 4.4a.

Now, these properties are extracted from many single rod nanostructures, of which the lengths are accurately determined by a SEM. The fundamental resonance of the rod antenna as a function of rod length is shown in figure 4.4b for both experiment (purple) and simulation (red). Experimental resonances overlap well with those extracted from FDTD simulations. For smaller rod lengths, however, a slight deviation between simulation and experiment is observed. For smaller rod lengths, irregularities in the fabricated rod antennas will have a more pronounced effect as in the case for longer rod antennas.

Additionally, the linewidths of the fundamental longitudinal resonances are plotted versus the antenna length in figure 4.4c. It is seen that with increasing lengths, the antenna linewidth increases. This could already be observed from figure 4.3, where in both experiment and simulation the linewidth of the antenna resonance broadens with increasing antenna length.

To understand this observation better, the different contributions to the total antenna linewidth are examined. The total linewidth Γ_{tot} is given by [36]:

$$\Gamma_{tot} = \Gamma_{bulk} + \frac{Av_f}{L_{eff}} + BV. \tag{4.2}$$

The first term describes the bulk contribution to the total linewidth and is constant. The second term accounts for surface scattering of electrons in the structure, where v_f is the Fermi velocity of the electrons, L_{eff} the effective pathlength of the electrons and A a constant on the order of unity. In this term, the effective pathlength scales as $L_{eff} \sim V/S$ [16], with V and S the total volume and surface area of a plasmonic structure respectively. The last term describes the radiation damping in the antenna and is proportional to the volume V, with B the constant of proportionality.

From equation 4.2 it is seen that there is a competition between surface and volume contributions to the total linewidth. For larger surface to volume ratios S/V, the surface contribution dominates the expression, whereas for smaller ratios the volume contribution becomes the leading term. This competition was directly observed in previous experiments as well [36]. In this work, it is shown that the LSP linewidth in gold nanorods can be minimized by finding an optimal balance between surface scattering and radiation damping contributions. The optimum surface to volume ratio of the rods was found to be equal to $S/V = 0.32$. Since we are working with smaller surface to volume ratios of the nanorods in this thesis, the volume contributions dominate over the surface contributions in this work. Therefore, the observed increase in LSP linewidth with increasing length is attributed to the increased radiative damping in the nanostructures.

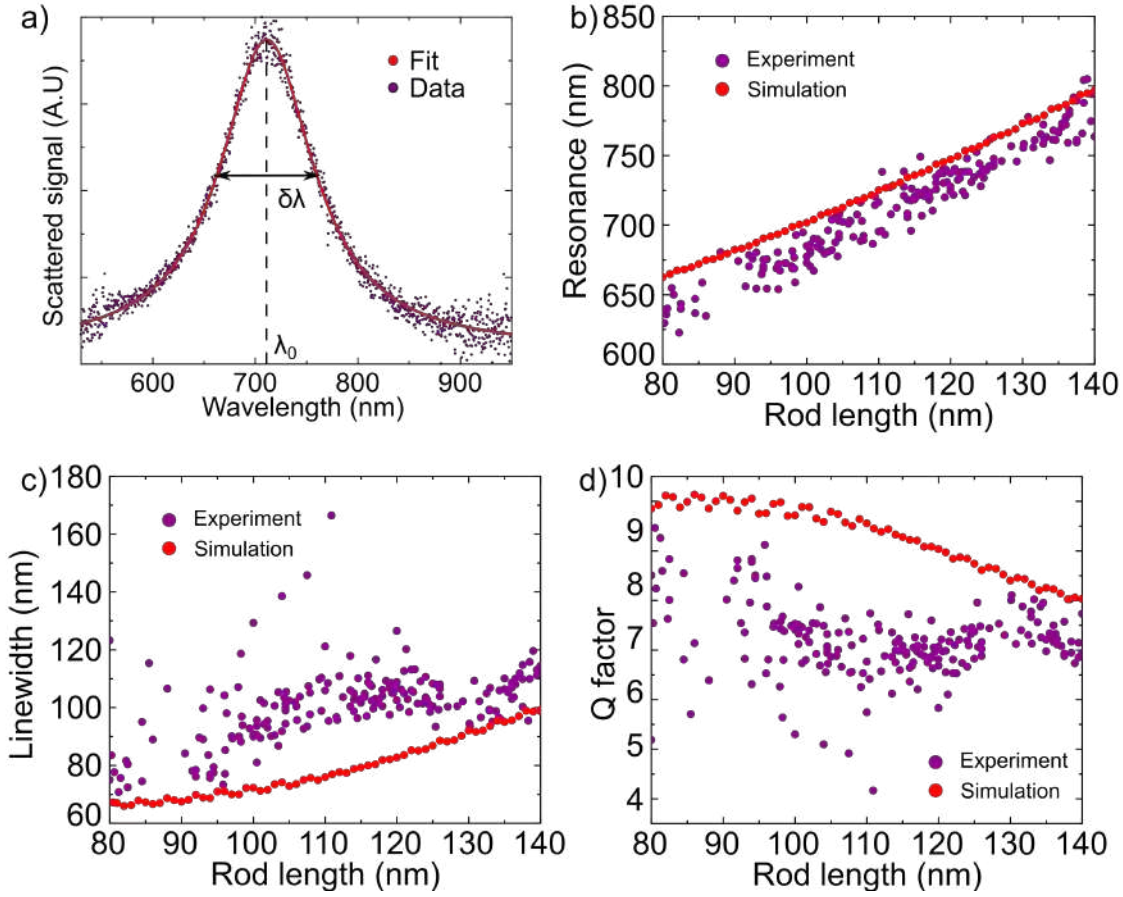

Figure 4.4: Statistical analysis of many single gold nanorod structures. a) A Lorentzian function is fitted through the antenna scattering spectrum. From this fit, resonances and linewidths are extracted which are plotted versus the antenna length in b) and c) respectively. Antenna dimensions are here accurately measured by the SEM. The antenna Q-factor is plotted versus the antenna length in d).

Finally, a quality factor Q can be assigned to each nanostructure by the following relation:

$$Q = \frac{\lambda_0}{\delta\lambda}. \tag{4.3}$$

In figure 4.4d the Q-factors are plotted versus the antenna length. The quantitative values of the quality factors are in reasonable agreement with reported literature values [4]. The difference between the simulated and experimental Q factors originate from the smaller simulated linewidth values with respect to the experimental linewidths as observed earlier.

4.2 Dimer antennas

Now that we have studied the behaviour of isolated gold nanorods in detail, we turn to the behaviour of two nanorods separated by a small gap. Because we are interested in small mode volumes and high electric field enhancement, the gap between the rods is ideally as small as possible, as already shown in chapter 3. Dimer structures where fabricated with EBL and the resulting structures are shown in figure 4.5a for varying designed gap sizes. As can be seen, the finite resolution of EBL imposes a challenge on the smallest possible gap size that can be

fabricated. For designed gap sizes of 20 and 25 *nm*, the dimer structure blends together into one long rod. From experience, a programmed gap size of 30 *nm* allowed for the highest quality dimer structures while maintaining the smallest gap size.

The fabricated gap size in the final dimer structure varies considerably from the designed gap-size of 30 *nm*, as can be seen in figure 4.5b. Here, a histogram plot of fabricated gap sizes, which are accurately measured by the SEM, is shown for multiple dimer structures. First of all, it is observed that there is a big spread in final gap sizes. This is not surprising considering that the dimers are directly patterned with EBL and so are subject to all the delicate fabrication steps. Furthermore, the mean of the final gap sizes is lower than the designed gap size, which is caused

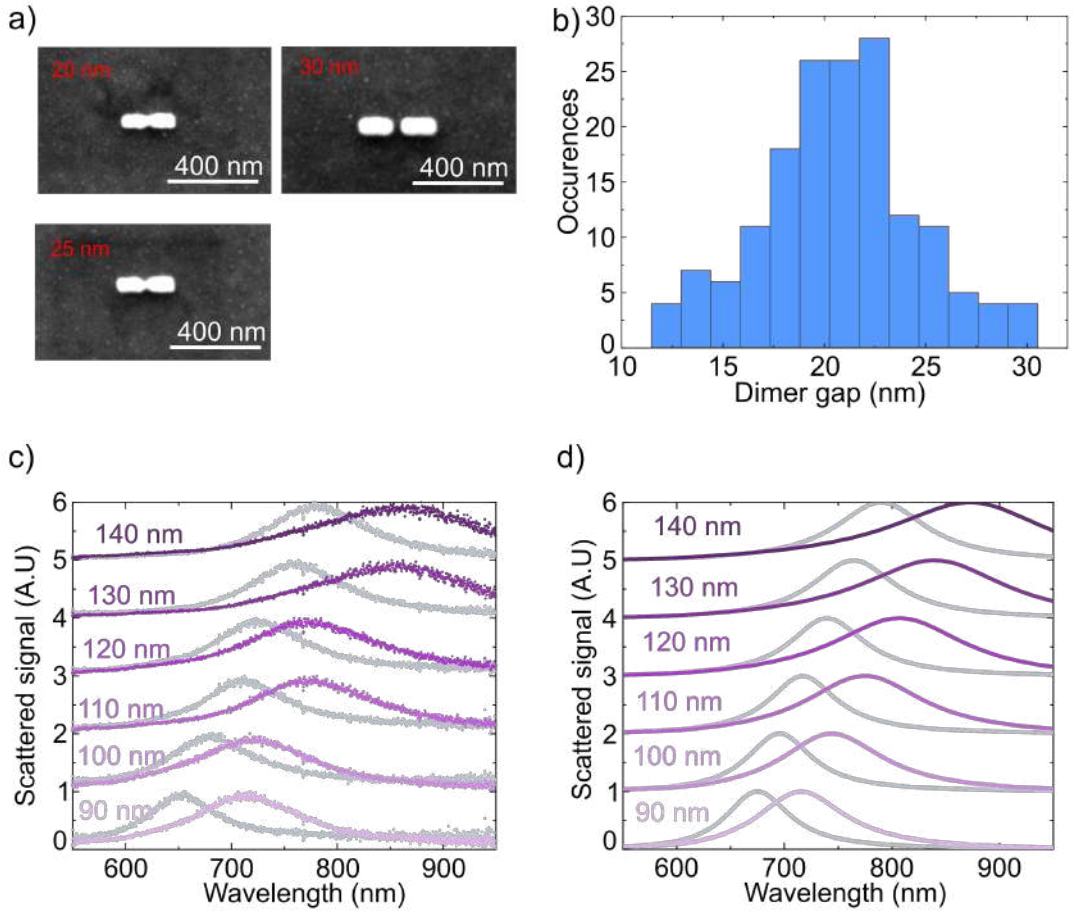

Figure 4.5: Characterization of gold nanodimers. a) SEM images of dimers with designed gap sizes of 20, 25 and 30 *nm*, indicated in red in the figures. b) Histogram plot of the measured gap sizes in the final structures of a dimer with designed gap size of 30 *nm*. c) Scattering spectra of isolated dimer structures (purple) in comparison with isolated rods (grey). d) Corresponding FDTD simulation results.

by the finite resolution of the EBL, where the proximity effect ensures that the exposed area in the gap of the dimer structure widens.

We now turn our attention to the optical characterization of the dimer structures. Again, dark-field spectra of individual dimer structures are captured. Now, the length of the rods which are part of the dimer is varied, while the distribution of the gap size is shown in figure 4.5b. Dark-field spectra of the dimer structures are shown in figure 4.5c in purple. To provide a comparison,

scattering spectra of corresponding isolated rods with the same lengths as the rods in the dimer structure are shown in grey in the same figure. In figure 4.5d, corresponding FDTD simulation spectra are shown. In these simulations, the gap size in the dimer structures is set to 20 nm, in agreement with the distribution of figure 4.5b.

We observe a red shift in resonance for all dimer structures with respect to the corresponding rod spectra. As two individual antennas are brought extremely close together in the dimer structure, the coupling between individual antennas in the dimers becomes an important factor. The effect is explained by looking at the energy diagram of two rod antennas brought closely together, as shown in figure 4.6.

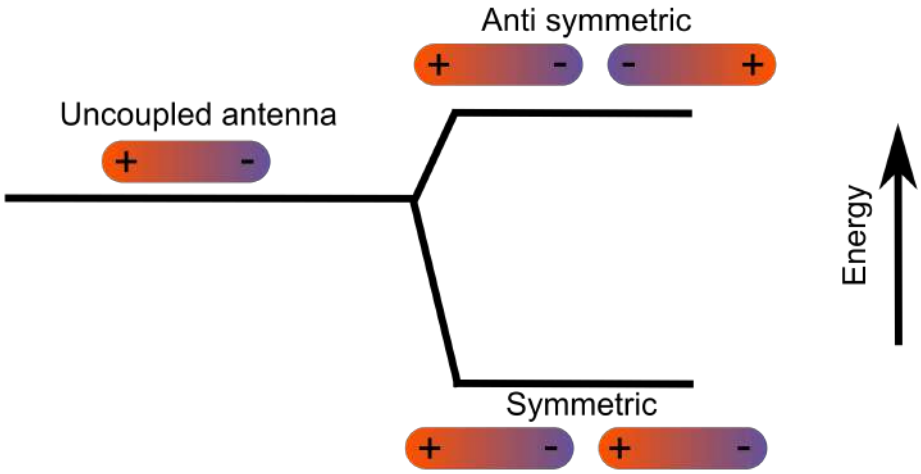

Figure 4.6: Symmetric and anti-symmetric modes of electron oscillations in an antenna-antenna coupled system with corresponding energies. The uncoupled antenna is shown as well.

As the rods are brought closer together, coulomb forces of the oscillating electrons in one rod are starting to influence the oscillation of the electrons in the other. Now, the two antennas are coupled to eachother, much like the situation of two coupled springs. Likewise, the dipolar eigenmode of the isolated rod now splits into a symmetric and an anti-symmetric supermode, where the antisymmetric mode is higher in energy than the symmetric mode. The coupled dimer antenna thus contains two fundamental resonances. The anti-symmetric mode, however, cannot couple to the far-field because of destructive interference and is thereby a dark mode. The symmetric mode, on the other hand, does not suffer from destructive interference. This bright mode is then the only mode that can couple to the far-field and is indeed the mode that is measured in the dark-field scattering spectra. As the energy of this eigenmode is lower than the energy of the uncoupled rod, a redshift in resonance is therefore expected, pricisely what is seen in the measured spectra.

Measured spectra are in good agreement with the FDTD simulation results. The slight deviations in resonance positions in the measured scattering spectra of the dimer rods can be attributed to the large distribution in gap sizes, thereby causing a distribution in redshifts as well.

Finally, it can be seen that the linewidth of the dimer structure is greater than the linewidth of the individual rods. This is again a result of the increased radiative damping, as now the total volume of the structure is increased.

Helium-FIB dimers

Dimer structures directly fabricated by EBL are prone to large deviations in the gap size, as was seen in figure 4.5b. Furthermore, the minimal gap size that can be fabricated in this direct way is limited by the finite resolution of EBL, which limited the gap size in this report to approximately 20 nm. Helium FIB milling can be used as a secondary step in the fabrication process, in which

dimers are formed by milling a gap in the centre of a long rod antenna. HIM images of a dimer fabricated in this way are shown in figure 4.7a and b, where the antennas were milled by *Monserrat Alvarez*. Due to the increased resolution of the helium FIB with respect to EBL, smaller and more controlled gap sizes can now be attained. In the following, antennas with different lengths were again fabricated and a gap of 8 nm was milled to form a dimer structure. Scattering spectra of the individual dimers are again measured and shown in purple in figure 4.7c. As a reference, the spectra of isolated rods with the same lengths are shown in the same figure in grey. Corresponding FDTD simulation results are shown in figure 4.7d.

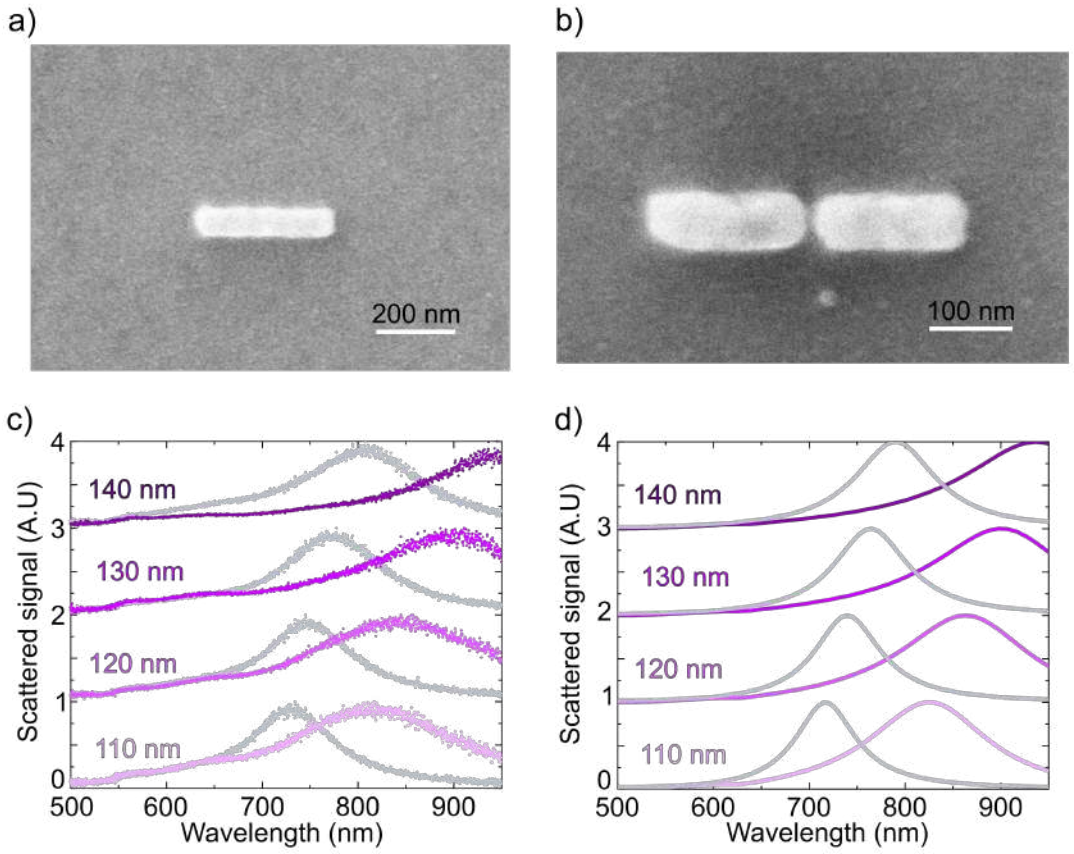

Figure 4.7: Characterization of helium FIB milled dimer structures. HIM images of a rod before and after FIB milling are shown in a) and b) respectively. c) Dark-field scattering spectra of helium FIB milled dimers (purple) in comparison to single rods. d) Corresponding FDTD simulation spectra. (Dimers are fabrication by Monserrat Alvarez.)

The redshift in resonance and broadening of the linewidth are again appreciated and more pronounced as in the case of the EBL fabricated dimers. The narrower gap in these dimer structures ensure a greater antenna-antenna coupling and therefore a greater split in fundamental resonances. The redshift in the bright anti-symmetric mode is therefore more pronounced as well, explaining the enhanced redshift in resonance in helium FIB milled dimer structures. Again, there is good agreement between experiment and simulation.

Bowtie antennas

As an alternative to rod antennas, other geometries might be used in experiments regarding strong light-matter interactions. It is shown [54] for example that, besides rods, bowtie antennas are able

to achieve extremely high field enhancements in their gaps as well.

SEM images of bowtie antennas are shown in figure 4.8. Bowtie antennas are a more complicated structure than rod antennas, hence the fabrication imposed some difficulties. The antennas were designed as triangles with infinitely sharp corners, hence rounding of the corners is a more pronounced issue with respect to rod antennas. The rounding of the corners therefore also influences the final antenna length and gap size tremendously. Therefore, in the remainder of this work, the rod antennas are preferred over the bowtie structure.

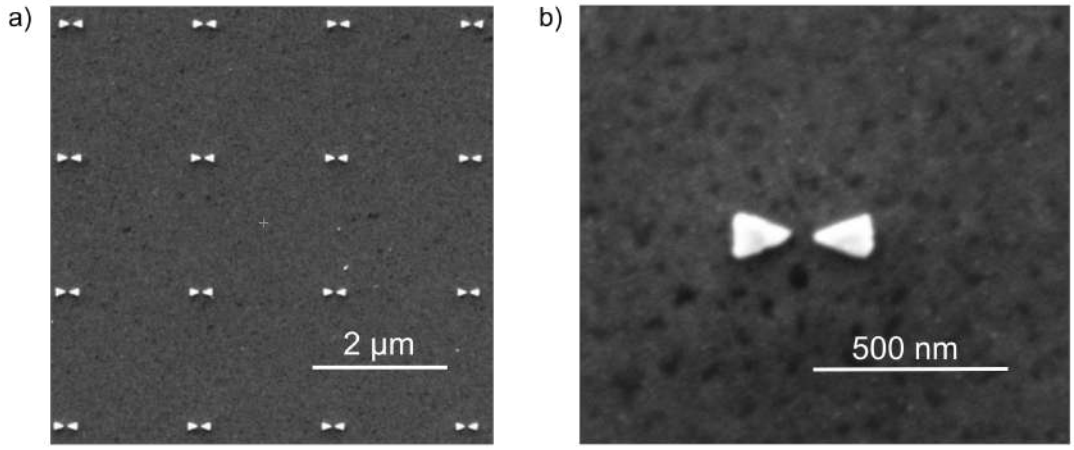

Figure 4.8: Sem images of a) an array and b) a single bowtie antenna structure

Chapter 5

Emitter-antenna interactions

In this chapter, the emitter-antenna coupling will be investigated. It will be shown how an ensemble of fluorescent dye molecules can induce mode splitting in both a dimer and a single rod antenna. These observations are supported by FDTD simulations. Next, fitting of the results to a theoretical model is discussed. Finally, experiments regarding the coupling of other emitters are described.

5.1 Rhodamine 800

In this section, all experiments are performed with the fluorescent dye emitter Rhodamine 800 (Rho. 800) (Sigma-Aldrich), of which the molecular structure is shown in figure 5.1a. Rho. 800 is an interesting choice for studying strong emitter-antenna interactions due to its high inherent transition dipole moment [14]. Looking back at equation 1.9, it is seen that the coupling strength increases as more molecules are coupled to the cavity mode volume. As a first approach, it is thus desired to couple as many molecules as possible to the antenna structures in order to increase the probability of observing strong interactions. Hence, a high concentration (0.01 mM) of Rho. 800 molecules in a solution of ethanol in spincoated onto the antenna covered glass coverslip, as sketched in figure 5.1c. This is done with a revolution speed of 4000 rpm for 30 seconds. In this way, it is ensured that molecules are dispersed in a homogeneous manner over the antenna covered area, such that single antennas can couple to an ensemble of Rho. 800 molecules.

In figure 5.1b, the absorption and fluorescence of Rho. 800 are shown. As a Rho. 800 molecule absorbs a photon, it promotes the molecule to a higher energy state. The energy states of a molecule consist of a manifold of vibrational states and the molecule will also find itself in a higher vibrational state in this excited state manifold. After relaxation of the molecule to a lower vibrational state, the molecule can return back to the ground state by emitting a photon. As the molecule has lost energy by internal relaxation, the emitted photon will be redshifted with respect to the absorbed photon. This is also observed in figure 5.1, where the maxima of the main fluorescence band is redshifted with respect to the main absorption band.

There needs to be a reasonable overlap between the transition of the dye molecule and the resonance of the antenna in order to efficiently couple both resonators to one another. As main resonance of the molecule, the absorption maxima of the main transition is taken. This choice, however, is open for discussion, as will be done later in this section. For the moment, however, we follow literature convention and assign the molecular resonance to the absorption maximum of the main transition.

As said, the molecular resonance has to have sufficient overlap with the resonance of the cavity, in this case the nano-antenna resonance, in order to maximize the probability of observing strong interactions. In figure 5.1d, a series of scattering spectra of nano-antenna dimer structures with increasing lengths are depicted. The figure illustrates the ability to controllably sweep the resonance of a nano-antenna through the molecular resonance by changing its length.

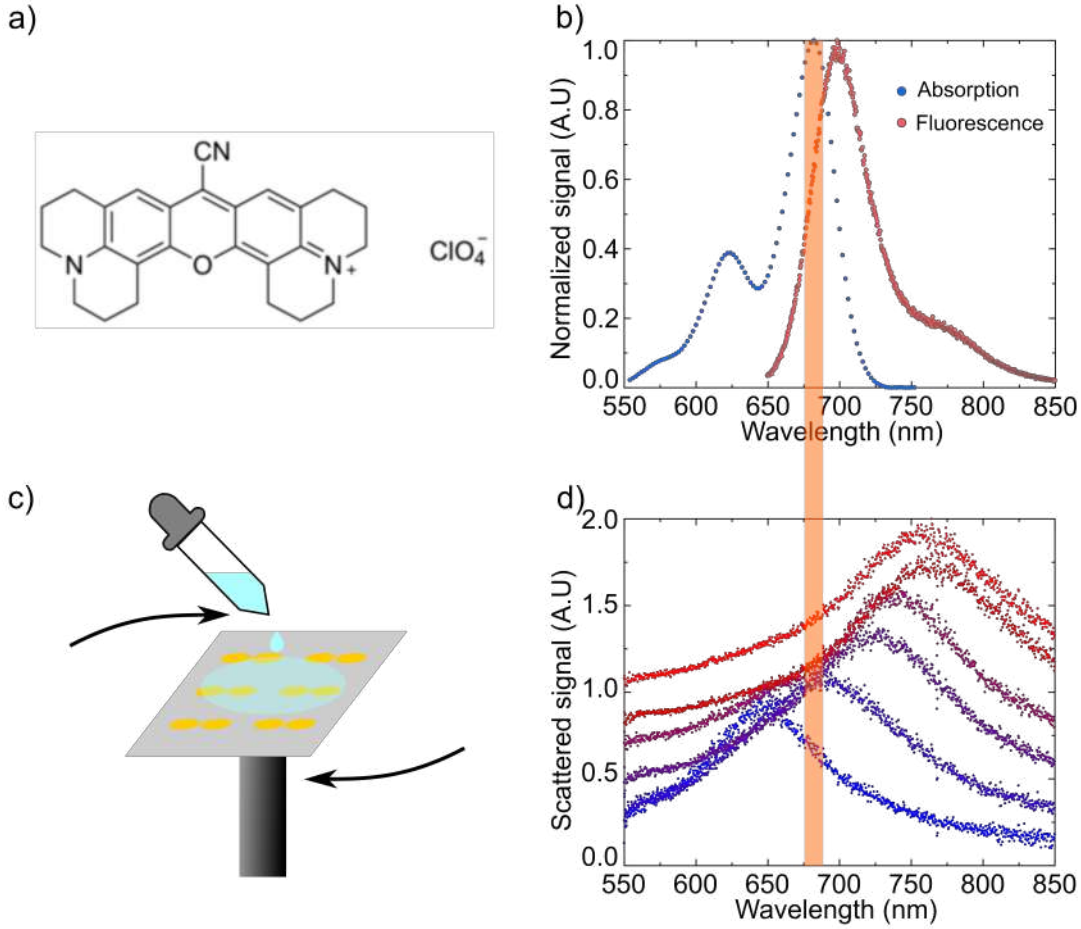

Figure 5.1: Concept of the emitter-antenna coupling experiments. a) Molecular structure of Rho. 800. (adapted from [55]) b) Absorption and fluorescence spectra of Rho. 800. c) Sketch of the sample preparation. d) Illustration of how the antenna resonance can be swept through the transition of the dye molecule by changing the length of the antenna.

5.1.1 Mode splitting

Before the main emitter-antenna interaction results are discussed, it is stressed again that scattering spectra of single isolated nano-antennas are captured. With the help of alignment markers on the nano-antenna sample, the position of each isolated antenna is known and thus a correlative single antenna study can be performed. In the following experiments, scattering spectra of isolated nano antennas are captured before and after molecules are spincoated onto the sample.

In figure 5.2a, an antenna luminescence scan captured by the APD is shown for a bare antenna sample, which shows the luminescence signal of an array of nano-antennas. The same scan is performed after molecules are spincoated onto the sample. A clear enhancement in signal is observed in the scan, originating from the fluorescence of the dye molecules. The signal originating from the antennas is not intrinsic antenna luminescence, but rather fluorescence enhancement of dye molecules in the vicinity of the nano-antenna. As described in chapter 1, a nano-antenna can enhance the local density of optical state of an emitter and so enhance its fluorescence.

A scattering spectrum of a single nano-antenna is captured before (blue) and after (purple) spincoating the solution of dye molecules, as depicted in figure 5.2d. The antenna resonance clearly splits into two modes after the molecules are added to the antenna, indicating strong

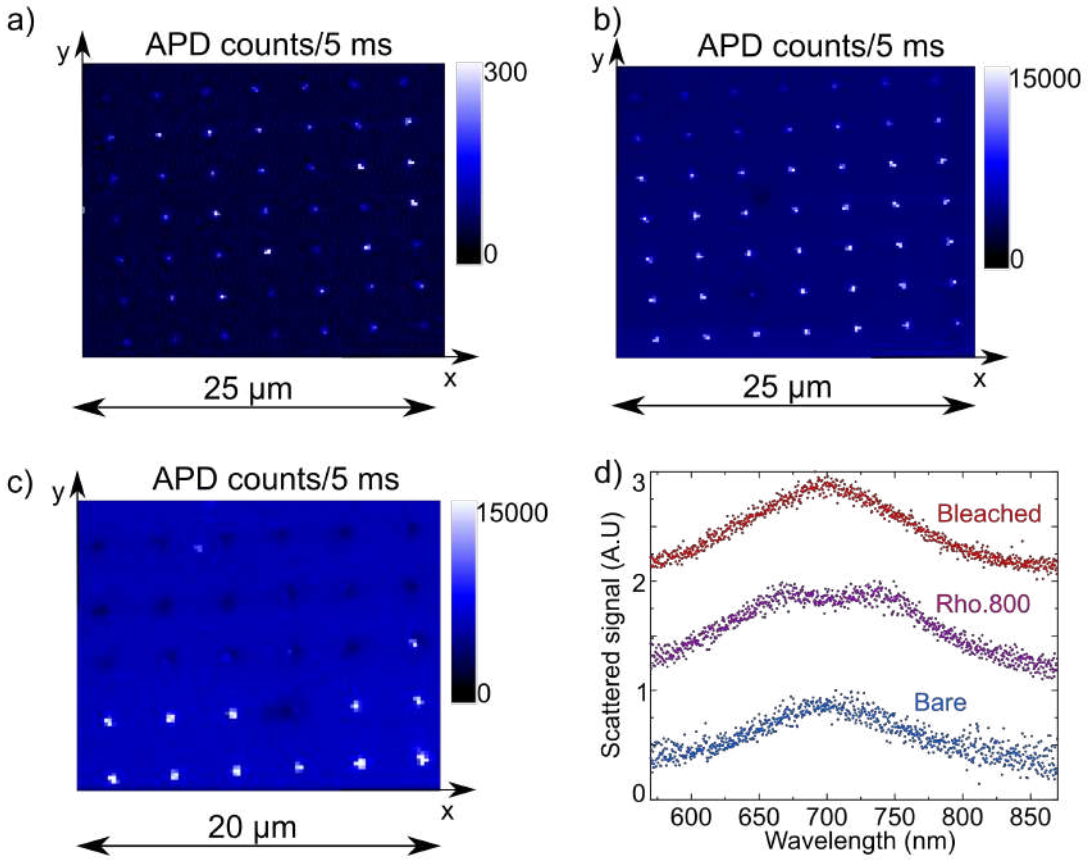

Figure 5.2: Mode splitting in a nano-antenna. APD scans a) before and b) after spincoating dye molecules onto the antenna sample. c) APD scan of a partially bleached antenna array. d) Scattering spectra of a nano-antenna before (blue) and after (purple) spincoating dye molecules. A scattering spectra of the same antenna after photobleaching all molecules in its vicinity is shown in purple.

antenna-emitter coupling. To confirm that the molecular resonance is responsible for the change in scattering spectra, all molecules in the vicinity of the respective antenna are photobleached by laser illumination (CW, 685 nm). Figure 5.2c illustrates the idea, where the dark spots on the scan show the areas of the photobleached molecules. The scattering spectra of the antenna is captured once more and shown in red in figure 5.2d. The splitting of the antenna resonance vanishes and the antenna resonance with bleached molecules coincides with the original uncoupled (blue) spectrum. Note that the 3 spectra captured in figure 5.2d are of the same isolated antenna. These results indicate that it is indeed the molecular resonance that is responsible for the mode splitting in antenna resonance, hence an ensemble of dye molecules strongly interacting with a single nano-antenna.

5.1.2 Rods vs Dimers

Next, it is described how the antenna resonance is swept through the transition resonance of the molecule. This is done by changing the length of the antenna, as described in the previous section and done for both single rod and dimer antennas. Figure 5.3 summarizes the effect the Rho. 800 molecules have on rod antennas with different lengths. In figures 5.3a and c, the dark-field

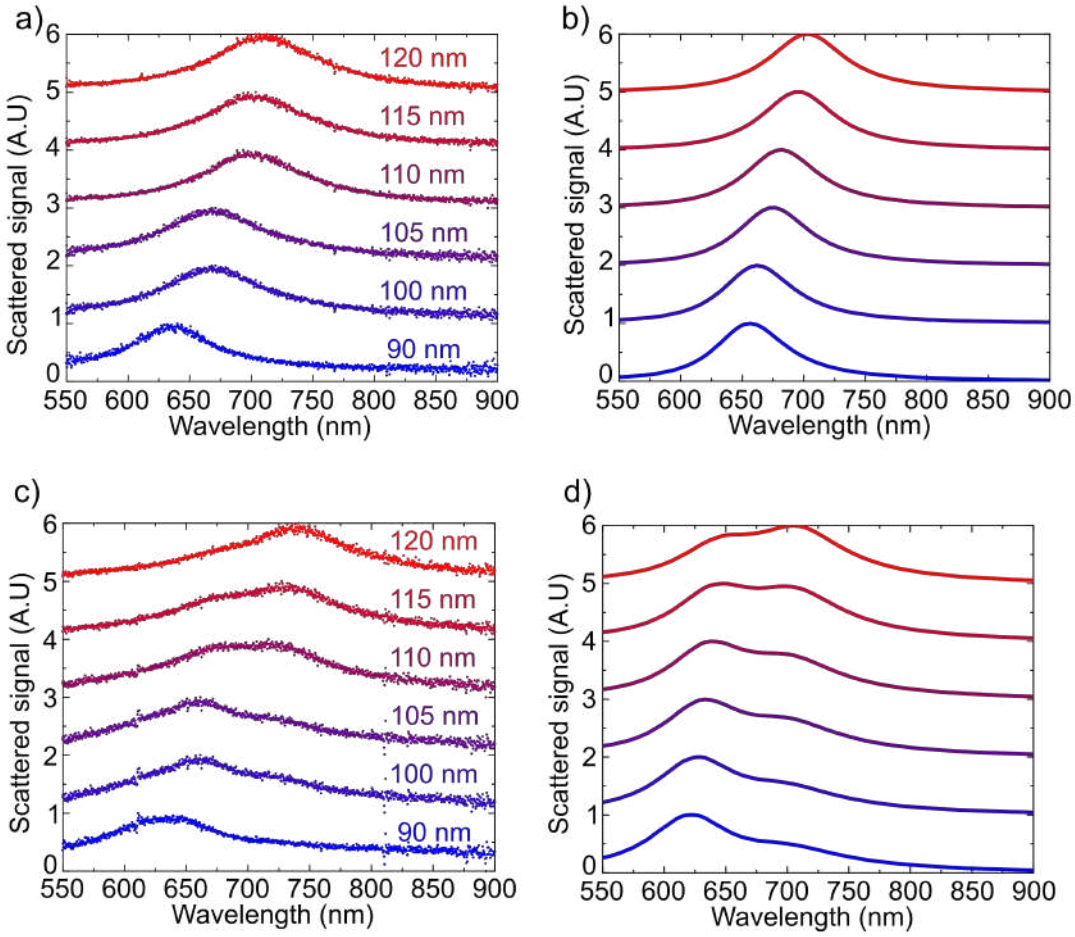

Figure 5.3: Effect of dye molecules on rods with varying resonances. Dark-field scattering spectra of rod antennas a) before and c) after spincoating the sample with Rho. 800 dye molecules. Corresponding colors here are the same antennas. b) and d) show FDTD simulation results.

spectra of isolated rods are captured before and after spincoating the antennas with Rho. 800 dye molecules. In this figure, corresponding colors indicate the exact same antennas. As the antenna resonance is swept through the molecular transition, the antenna resonances again split into two modes after the addition of the molecules. Taking a closer look at figure 5.3c, an indication to anticrossing can be observed, where the splitting is most clear around the molecular resonance. As the detuning between antenna and molecular resonance is increased, the mode splitting becomes more asymmetric, where the stronger scattered mode approaches the uncoupled antenna resonance as shown in figure 5.3a again. FDTD simulations spectra, shown in figures 5.3b and d, follow the same qualitative behaviour as for the experimental spectra. Details on how the experiment is modelled in the simulations are explained in appendix B.

The same experiment is repeated for dimer antennas, where the results are summarized in figure 5.4. The gap in these dimer structures is described by the distribution as shown in figure 4.5b. The same anticrossing behaviour is appreciated as the antenna resonance is swept through the molecular transition. The splitting in the dimer is, however, more pronounced compared to the rod antenna. This is a result of the reduced mode volume created by the gap of the dimer structure, leading to a stronger coupling between the molecules and thus a greater mode splitting. Corresponding FDTD simulations again follow the same qualitative behaviour.

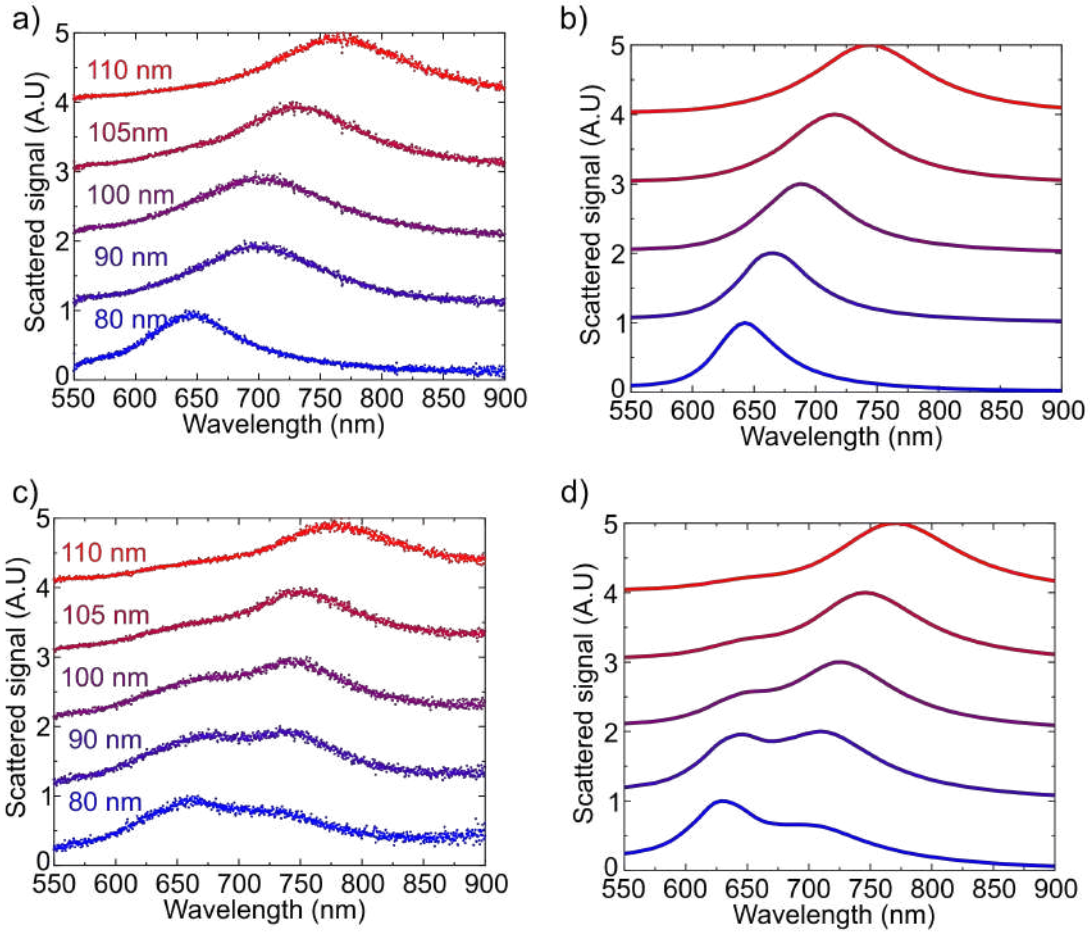

Figure 5.4: Effect of dye molecules on dimers with varying resonances. Dark-field scattering spectra of dimer antennas a) before and c) after spincoating the sample with Rho. 800 dye molecules. Corresponding colors here are the same antennas. b) and d) show FDTD simulation results.

Transition from coupled to uncoupled

Finally, the gradual transition from a coupled to an uncoupled nanoantenna is visualized by performing a stepwise bleaching experiment. In this experiment, a portion of the molecules in the vicinity of the nanostructure is bleached, after which a spectrum of the antenna is obtained, after which another portion of molecules is bleached, etc. This experiment is done in 6 bleaching steps and the results are summarized in figure 5.5. A gradual transition from modesplitting to single antenna resonance is observed. This is in accordance with the expectations, as a stepwise photobleaching of the molecules induces a gradual decrease in strongly coupled dye molecules and therefore a gradual decrease in mode splitting.

5.1.3 Theoretical fitting

In this section, we will interpret the results in more detail with the aid of a theoretical model, which is able to describe the scattering spectra of a strongly coupled nano-antenna. It is remarked that this theoretical model is different from the simulated model that is already shown in figures 5.4 and 5.3. First, a derivation of the fitting formula and description of the model are proposed,

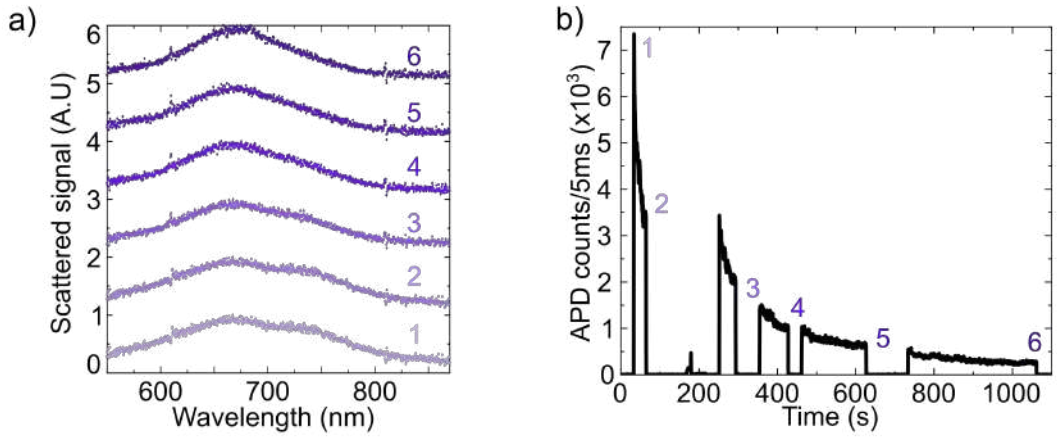

Figure 5.5: Stepwise bleaching of strongly coupled dye molecules. a) Gradual disappearance of modesplitting in the scattering spectra of a dimer antenna. b) A timetrace visualizing the stepwise decrease in fluorescence signal from the dye molecules. Bleaching steps are indicated with the numbers.

after which the fitting quality and results are discussed.

A strongly coupled nano antenna

The model [66] described here proposes a phenomenological description of strong coupling, describing the nanoantennas and emitters as two damped coupled oscillators. This model has been previously exploited to describe strong antenna-emitter interactions in single plasmonic nanostructures [52]. We start by writing down the equations of motions of two coupled damped oscillators under influence of external forces:

$$\frac{d^2x_p(t)}{dt^2} + \gamma_p \frac{x_p(t)}{dt} + \omega_p^2 x_p(t) + g\frac{dx_e(t)}{dt} = F_p(t), \tag{5.1}$$

$$\frac{d^2x_e(t)}{dt^2} + \gamma_e \frac{x_e(t)}{dt} + \omega_e^2 x_e(t) - g\frac{dx_p(t)}{dt} = F_e(t). \tag{5.2}$$

In these equations, x, γ and ω denote the positions, dampings and natural frequencies of the oscillators respectively. Subscripts p and e indicate plasmon and emitter respectively. Finally, the oscillators are coupled to each other by a coupling strength g.

The forces $F_e(t)$ and $F_p(t)$ represent external forces on the emitter and the plasmons respectively induced by the electromagnetic field. As the extinction cross section of the emitter is negligible compared to the plasmon cross section in the antenna, such that $F_e(t) << F_p(t)$, the force exerted on the emitter is set to zero: $F_e(t) = 0$. Furthermore, we assume a time harmonic driving field with frequency ω, such that the external force on the plasmon can be written as: $F_p(t) = F_p e^{-i\omega t}$. The plasmons and emitters will then follow this driving force and the system can be solved to obtain expressions for the coordinates as:

$$x_p(t) = \mathrm{Re}\,\frac{(\omega_e^2 - \omega^2 - i\gamma_e\omega)F_p(t)}{(\omega^2 - \omega_p^2 + i\gamma_p\omega)(\omega^2 - \omega_e^2 + i\gamma_e\omega) - \omega^2 g^2}, \tag{5.3}$$

$$x_p(t) = \mathrm{Re}\,\frac{-ig\omega F_p(t)}{(\omega^2 - \omega_p^2 + i\gamma_p\omega)(\omega^2 - \omega_e^2 + i\gamma_e\omega) - \omega^2 g^2}. \tag{5.4}$$

The energy lost by the electromagnetic driving field is represented by the extinction cross section of the plasmonic structure, which can thus be described by the total work done by the

external driving field as $C_{ext}(\omega) \sim \langle F_p(t)\frac{dx_p(t)}{dt}\rangle$. here, the brackets indicate the average over one period of oscillation. Thus, the following expression for the extinction cross section of the nanostructure can be derived:

$$C_{ext} \propto \omega \,\mathrm{Im}\,(\frac{\omega_e^2 - \omega^2 - i\gamma_e\omega}{(\omega^2 - \omega_p + i\gamma_p\omega)(\omega^2 - \omega_e^2 + i\gamma_e\omega) - \omega^2 g^2}) \tag{5.5}$$

This expression thus describes the combined effect of absorption and scattering in a plasmonic nanostructure. In the experiments, however, only the scattering contribution of the nanostructures is measured. The scattering cross section can be calculated by considering the polarizability α of the nanostructure and can then be calculated according to:

$$C_{sca}(\omega) \sim k^4 \mid \alpha \mid^2, \tag{5.6}$$

with k the magnitude of the k-vector. In the quasistatic limit of small structures with respect to the wavelength of incoming radiation, the extinction cross section can be written as [10]: $C_{ext} \sim k\,\mathrm{Im}(\alpha)$. Now, the polarizability can be extracted from equation 5.5 and so the final expression for the scattering spectra of a coupled antenna can be written as:

$$C_{scat} \propto \omega^4 \mid \frac{\omega_e^2 - \omega^2 - i\gamma_e\omega}{(\omega^2 - \omega_p^2 + i\gamma_p\omega)(\omega^2 - \omega_e^2 + i\gamma_e\omega) - \omega^2 g^2} \mid^2 \tag{5.7}$$

It is remarked that the coupling terms in this derivation assume a coupling proportional to the derivatives of the positions of the oscillators. Other coupling terms, for example couplings proportional to the positions of the oscillators, as discussed in equations 1.1 and 1.2, could be applied as well. However, it can be shown [42] that if these modifications were applied to equations 5.1 and 5.2, this would only transform the last term in the denominator in equation 5.7 as $\omega^2 g^2 \rightarrow \omega_e\omega_p g^2$. In the regime of $g, \gamma_e, \gamma_{pl} << \omega$, which applies to the work performed in this thesis, the two models give generic results and therefore we will continue the analysis with formula 5.7.

Unit conversion

In order to fit the data to the theoretical model described in the previous section, the scattering spectra have to be represented as a function of a frequency, or energy, instead of a wavelength. We thus have to convert the spectra from the wavelength to the energy domain. This unit conversion uses the familiar expression for the energy of an electromagnetic wave:

$$E = \frac{hc}{\lambda}. \tag{5.8}$$

However, we have to be very careful in converting data between the wavelength and energy domain. Due to the inverse relationship, the bin size in the energy domain, or rather the "signal per unit energy" will no longer be evenly spaced as was the case for the bin size in the wavelength domain. The issue is sketched in figures 5.6a and b, where the difference in binsize is highlighted.

We thus cannot simply use equation 5.8 to convert the wavelength to energy. The signal itself must be normalized as well to compensate for the unequal binsizes. The recorded signal in an infinitesimal range must be the same in the energy and wavelength domain in order to satisfy the conservation of energy: $f(\lambda)d\lambda = f(E)dE$. So, for signal values $f(E)$ in the energy domain, we can write down the following relation by using equation 5.8:

$$f(E) = f(\lambda)\frac{d\lambda}{dE} = -f(\lambda)\frac{hc}{\lambda^2}, \tag{5.9}$$

where the minus sign is a consequence of the integration direction and can be ignored. It is seen that besides the conversion of wavelength to energy, the signal values themselves must be scaled by a factor $\frac{hc}{\lambda^2}$ in order to correctly switch between wavelength and energy domain. An antenna spectrum in both wavelength and energy domain is shown in figures 5.6c and d respectively.

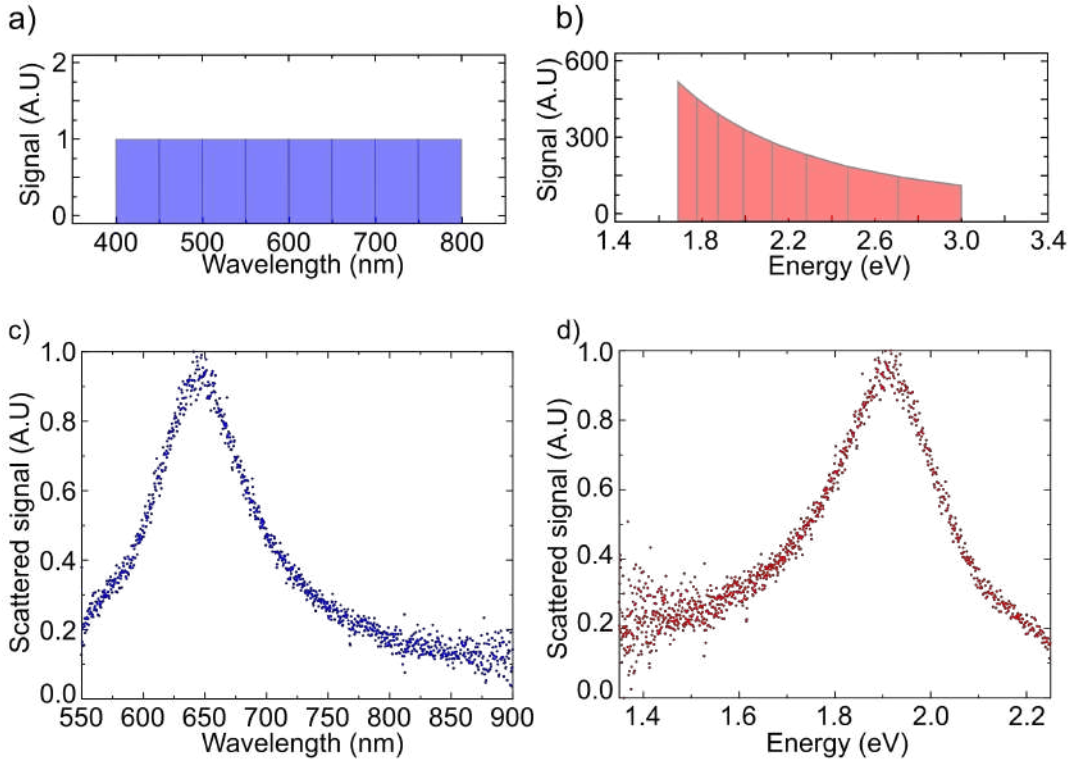

Figure 5.6: Converting data between wavelength and energy domain. Binsize in the wavelength (a) and energy (b) domain, adapted from [33]. Scattering spectra in the wavelength (c) and energy (d) domain.

Fitting analysis

Equipped with a theoretical formula describing the scattering spectrum of a strongly interacting nano-antenna as described in equation 5.7, we are in a position to fit the scattering spectra of the antennas interacting with the ensemble of dye molecules. Looking again at the fitting formula 5.7, it is seen that there are 5 adjustable parameters, namely $\omega_e, \omega_p, \gamma_e, \gamma_p$, which represent the uncoupled molecular and antenna resonances and linewidths respectively and the coupling constant g. The uncoupled resonances and linewidths are all a priori known parameters, because the uncoupled antenna spectra are measured before the dye molecules were added and the molecular transition is determined by the absorption spectrum. These four parameters should thus ideally be kept fixed in the fitting, and the only parameter set free would be the coupling strength g, which could then be obtained for each coupled antenna. If the spectra are fitted in this way, the theoretical fit does not match the measured spectrum. The unsatisfying fitting result will be clarified later in this section. In order to obtain better fits, all 5 parameters are set free in the fitting from now. Unsurprisingly, the spectra and fit, which are shown in figure 5.7a, now are in good agreement with one another.

From these fits, a set of coupling strengths can be extracted for both the rod and dimer antennas. The results are shown in figure 5.7b, where the coupling strengths are plotted in a histogram distribution. First, it can be observed that the coupling strengths for the dimer antennas are slightly greater than for the rods. This is again a result of the reduced mode volume created by the dimer structure, hence leading to a stronger coupling with the dye molecules. This result could already be anticipated by looking back at figures 5.3 and 5.4, where the mode splitting is more pronounced in the case of the dimer antennas compared to the rods. Second, the

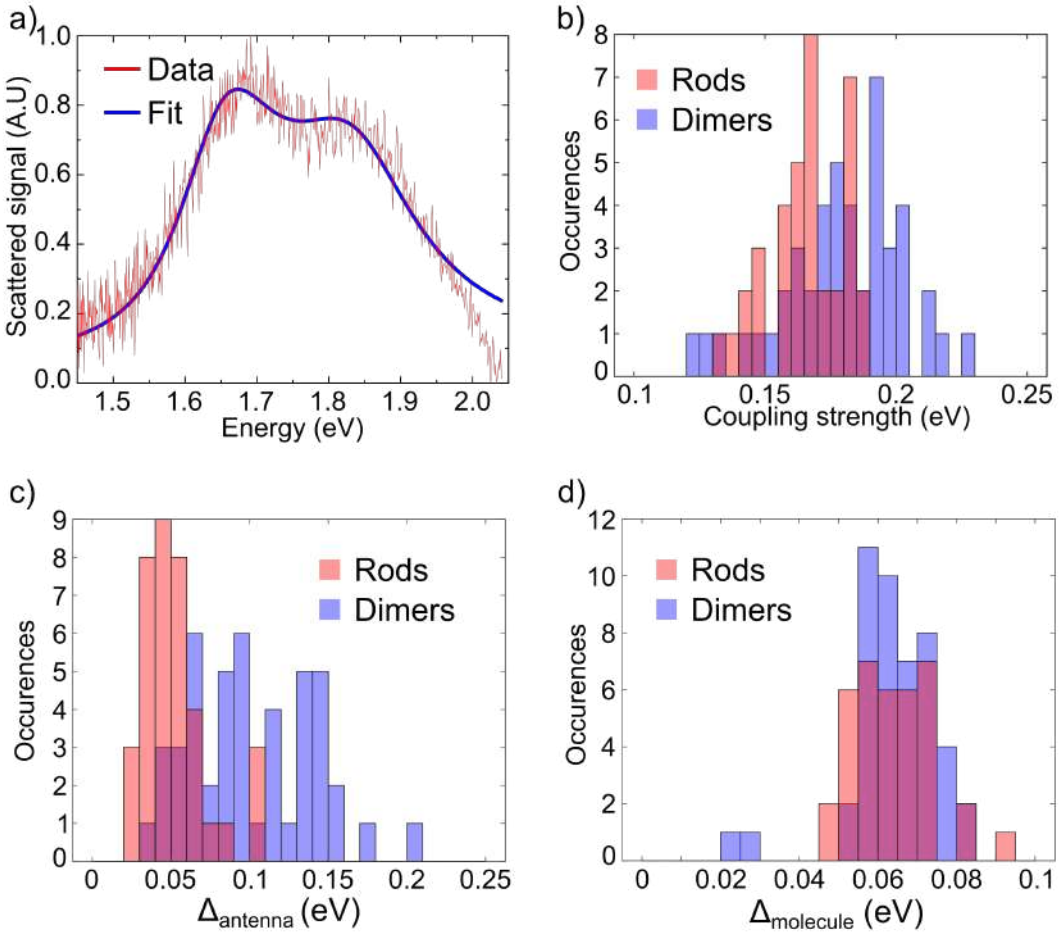

Figure 5.7: Fitting analysis of strongly coupled scattering spectra. a) measured scattering spectrum of an antenna interacting with dye molecules with theoretical fit. In the fit, all fitting parameters are set free. b) Extracted coupling strength for rods (red) and dimers (blue) from the fits described in a). c) Deviation of the fitted uncoupled antenna resonance from the uncoupled value as measured in the dark-field spectra. d) Deviation of the fitted uncoupled molecular resonance from the uncoupled value as measured in the absorption spectra.

distribution of coupling strengths in the case of the dimers seems to be wider than for the rods. This could be a result of the big variation in dimer gap sizes as shown in the distribution of figure 4.5b. The variation in gap sizes causes a variation in mode volume and thus in coupling strength as well, whereas for a rod antenna this variation is expected to be less.

As mentioned previously, all parameters in the fitting have been set free. We will now discuss how much the fitted molecule and antenna resonances deviate from the measured resonances. The deviations are shown in figure 5.7c and d for antenna and molecular resonances respectively. Here, the deviation Δ, defined as the measured resonance value minus the fitted resonance value $\Delta = E_{measured} - E_{fit}$, is shown in histogram distributions. As can be seen, all the antenna and molecular resonance values extracted from the fit are redshifted with respect to the resonances obtained from the measurements.

Indeed, by closer inspection of figure 5.5, it can be seen that the mode splitting is not symmetric. It is hypothesised that the ensemble of dye molecules not only induces a splitting in antenna resonance due to the strong interaction, but causes a redshift in uncoupled antenna resonance as

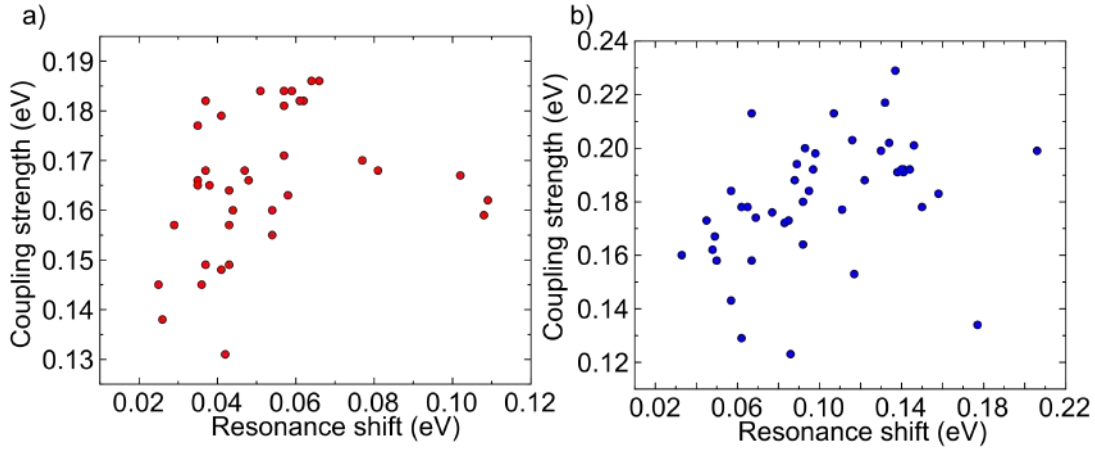

Figure 5.8: Correlation between redshifted antenna resonance and coupling strength for a) rod and b) dimer antennas.

well. The ensemble of dye molecules causes a change in dielectric environment in the vicinity of the nano antenna, thereby redshifting the fundamental antenna resonance. Indeed, it has been shown that even single molecules [71] can induce a shift in the fundamental resonance of a rod antenna, which forms the basis of plasmonic sensing applications. It should be marked here that the resonant character of the dye molecules is essential here. Apparently, an antenna covered in photo bleached molecules does not cause this shift. This is explained by arguing that an optically active molecule will induce a different dielectric environment compared to a photobleached molecule.

The shift in uncoupled resonance is proportional to the number of dye molecules in close vicinity to the nano-antenna. To further support the hypothesis of the molecule induced redshift in uncoupled antenna resonance, the coupling strength can thus be scatterplotted versus the shift in antenna resonance. There should be a correlation between coupling strength and redshifted resonance, as both quantities depend on the number of molecules in the vicinity of the antenna. These plots are shown in figure 5.8, for both the rod and dimer antennas. Indeed, the coupling strength seems to increase for increasing resonance redshifts. This indicates that the difference between fitted and measured uncoupled antenna resonance can be explained by the change in dielectric environment cause by the ensemble of dye molecules, effectively redshifting the antenna resonance.

Besides the redshift of fitted antenna resonance with respect to the measured antenna resonance, the same behaviour can be observed for the molecular resonance. It is stressed again that the measured molecular resonance is assumed to be represented by the maximum of the main transition in the absorption spectrum, following literature convention. But does it suffice to say that the resonance of an emitter is solely represented by the absorption spectrum? Take for instance a strong coupled quantum dot. A quantum dot does not have a clear absorption lineshape as dye molecules have. One can think about this problem in the time domain, where there is a coherent energy exchange between emitter and cavity. The emitter will absorb a trapped cavity photon, re-emit the photon etc. Here, fluorescence and absorption of the molecule are thus equally important in the strong interaction, hence there needs to be sufficient overlap between both absorption and fluorescence of the emitter in order for the strong interaction to manifest itself. When the effect of redshifted fluorescence of the emitter is taken into account in the assignment of emitter resonance, the overal resonance will thus be redshifted with respect to the resonance defined by absorption alone. The shift between absorption and fluorescence maxima as shown in figure 5.1b can be calculated to be 0.05 eV, which compares reasonably well to the distribution as shown in figure 5.7d.

Anticrossing dispersion

To conclude the fitting analysis, the maxima of the split modes can be extracted from the fits, which represent the upper ω_+ and lower ω_- polariton modes of the coupled antenna-emitter system. These hybrid modes can then be plotted versus the antenna-emitter detuning δ defined as $\delta = \omega_{pl} - \omega_{mol}$, with ω_{pl} and ω_{mol} the plasmon and molecular resonance respectively. Both these uncoupled resonances are taken to be equal to the values as extracted from the fitting. The uncoupled and hybrid modes are depicted in the dispersion plot in figure 5.9, for both rod (a) and dimer (b) antennas. Anticrossing behaviour of the hybrid modes is appreciated, characteristic for strongly interacting systems.

These hybrid modes can now be fitted with a coupled oscillator model [51], which describes the polariton energies $E_\pm$ by the following relation:

$$E_\pm = \frac{\delta}{2} + E_{mol} \pm \frac{1}{2}\sqrt{(\hbar\Omega_R)^2 + \delta^2}, \tag{5.10}$$

with δ the detuning as defined above, E_{mol} the energy of the molecular resonance and Ω_R the Rabi splitting. The molecular resonance in this relation is set equal to the average of the fitted energies of the molecular resonances and is kept fixed in the fitting. Fitting curves are added to the data in figure 5.9. From the fits, Rabi splittings can be extracted for both rod and dimer antennas. These are equal to $\hbar\Omega_R = 0.15eV$ and $\hbar\Omega_R = 0.10eV$ for dimer and rod antennas respectively. Again, the dimer antennas show a greater Rabi splitting caused by the reduced mode volume in comparison to the rod antennas.

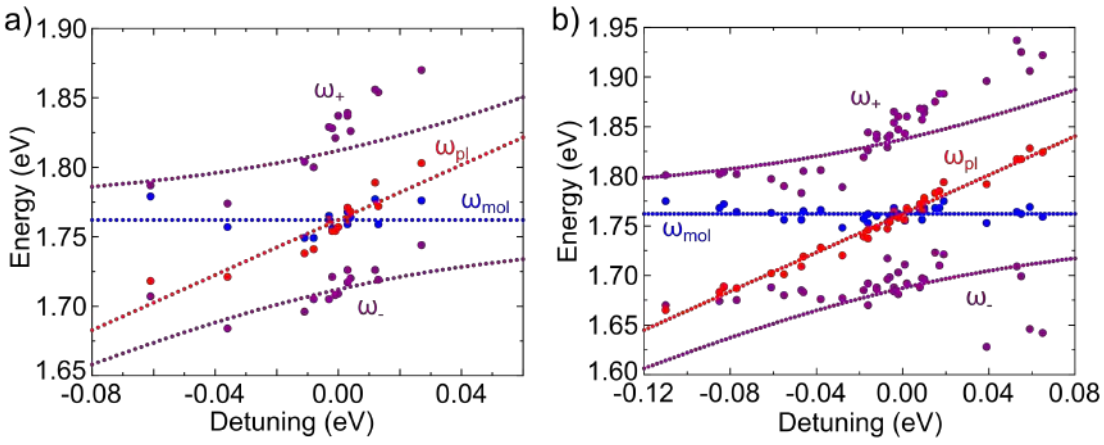

Figure 5.9: Dispersion diagram with corresponding coupled oscillator fits of the hybrid polariton modes for a) rod antennas and b) dimer antennas.

5.1.4 Fluorescence detection

Besides scattering detection, the fluorescence signal of the strongly coupled dye molecules should also show a mode splitting in their resonance. Indeed, splitting in fluorescence spectra has been reported in earlier work [63] [40] and provides additional information about the strong antenna-emitter interaction.

In the experiment, the molecule covered antenna is excited by a CW laser of 633 nm and fluorescence signal is recorded over time. Figure 5.10a the time evolution of the recorded fluorescence spectra is shown. The signal decreases over time, as we are photobleaching the system during laser excitation. Now, to ensure the least amount of molecules are bleached, we investigate a slice of

the fluorescence map at an early time. In these conditions, the coupling is expected to be highest, hence a split in fluorescence signal the most probable. A fluorescence spectrum of Rho. 800 molecules close to an antenna at an early time is shown in purple in figure 5.10b. As a reference, the fluorescence spectrum of Rho. 800 molecules on a glass coverslip without antennas in shown as well in red. As can be seen, no mode split in fluorescence spectrum is observed. This might have several reasons. First of all, dye molecules in close vicinity to the antenna couple the strongest, yet it is for molecules in these areas that fluorescence signal can be significantly suppressed by non-radiative quenching of fluorescence into dark modes of the antennas [18] [43].

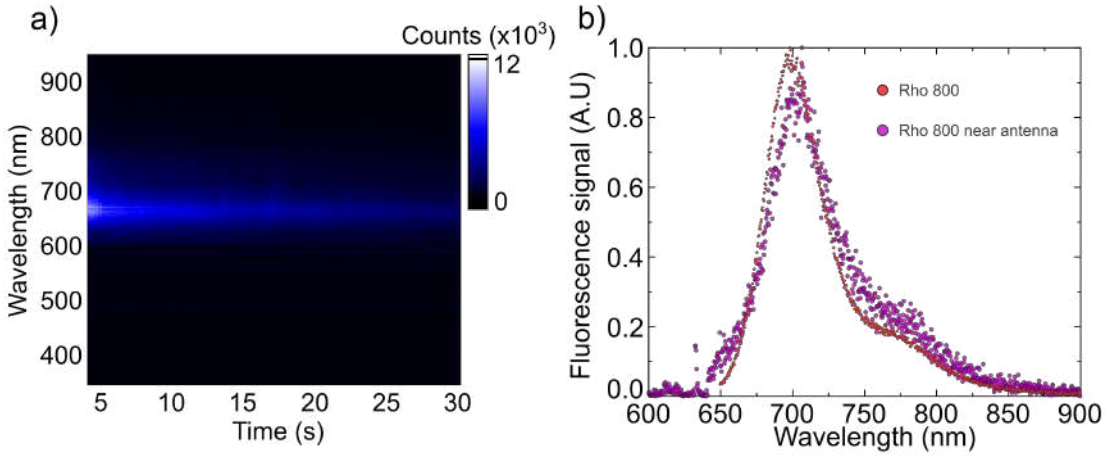

Figure 5.10: Fluorescence signal of Rho. 800 dye molecules in the vicinity of a nano-antenna. a) Evolution of the fluorescence signal in time. b) Fluorescence signal of Rho. 800 molecules close to an antenna (purple) at an early time. As a reference, the fluorescence spectrum of Rho. 800 molecules on glass (without nano antennas) is shown as well.

A second reason of the absence of mode splitting in the fluorescence spectrum is the high background fluorescence of uncoupled dye molecules. Assuming that mode splitted dye molecules are only present in the hotspots of the antenna structure, where the electric field amplitude is highest, this mode splitted signal can easily be overshadowed by the fluorescence of all the uncoupled molecules excited in the diffraction limited spotsize.

5.2 Quantum dots

Apart from coupling Rho. 800 dye molecules, other emitters have been attempted to couple to nano-antennas. Quantum dots for example, contain high absorption cross sections. Furthermore, they are very robust and photostable, making them suitable candidates to study antenna-emitter interactions.

In this attempt, an antenna fabricated glass coverslip is spincoated with a high concentration of carboxyl (Qdot 800 ITK) quantum dots in solution of MiliQ water. Again, APD fluorescence scans are taken before and after the sample is spincoated with quantum dots and are shown in figures 5.11a and b respectively. As was the case in figure 5.2, intrinsic antenna luminescence is detected when no quantum dots are present. After quantum dots are spincoated, the recorded signal increases, resulting from the fluorescence of the spincoated quantum dots. In contrast to figure 5.2, however, no antenna enhanced fluorescence is observed here.

Scattering spectra of an antenna before and after the addition of the quantum dots are shown in figure 5.11c in red and purple respectively. No splitting in antenna resonance is observed here. Instead, an enormous redshift in resonance is seen of the quantum dot covered antenna with respect to the bare antenna.

These results are explained as follows. By spincoating a high concentration of quantum dots onto the antennas, a thick layer of quantum dots is created, completely covering the antennas. As such, the background fluorescence emitted by this thick layer now overshadows the enhanced fluorescence of quantum dots close to an antenna, explaining why no antenna enhanced fluorescence is recorded. As a consequence of this thick layer, the dielectric environment is changed tremendously, which causes the redshift in fundamental antenna resonance.

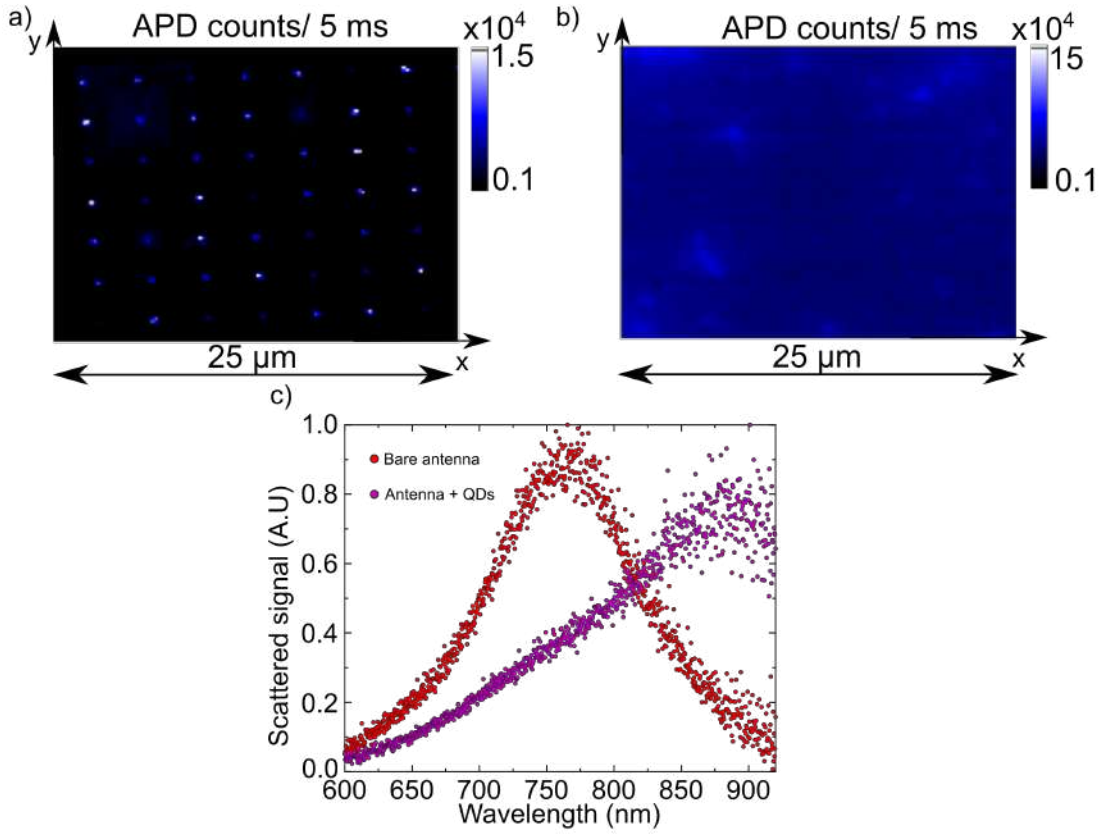

Figure 5.11: Coupling an ensemble of quantum dots to nano-antennas. a) APD scan of a bare antenna array showing intrinsic antenna luminscence b) APD scan after the addition of the quantum dot ensemble. c) Scattering spectra of a nano-antenna before (red) and after (purple) the addition of the quantum dots.

Chapter 6

Conclusions and outlook

By coupling quantum emitters to the sub-diffraction limited mode volumes of a plasmonic cavity, an exotic regime of light-matter interactions can be accessed, important for both fundamental research interest and potential applications. The work performed in this thesis explored this regime, by coupling an ensemble of quantum emitters to the electric near field of rod nano antenna structures.

It is shown how these nano structures were fabricated by top-down nanofabrication techniques, such as electron beam lithography and material deposition. Furthermore, an experimental setup has been built which is able to characterize these nanostructures by dark-field spectroscopy, where the plasmonic response of single nanorod structures was extensively studied. Experimental results were in good agreement with FDTD simulations, verifying the high performance of the setup.

In addition to dark-field characterization of plasmonic nanostructures, a fluorescence microscope has been constructed which was able to characterize fluorescent quantum emitters. Single step blinking of the recorded fluorescence signal confirmed that the setup was sensitive enough to measure and characterize optical properties down to the single quantum emitter level.

After the basic characterization of isolated antenna structures and quantum emitters, it was shown that coupling an ensemble of fluorescent dye molecules to the near fields of rod nano antenna structures could indeed induce strong light-matter interactions. Proof of strong antenna-emitter coupling relied on the observation of mode splitting in the fundamental resonance of single antenna structures after the addition of the dye molecules. By photobleaching the emitters in the vicinity of the nano structures, the splitting disappeared, confirming that indeed the resonant character of the quantum emitters induced the splitting. Furthermore, by varying the detuning between the resonances of the plasmonic cavity and the emitter, an anticrossing of the hybrid modes could be observed, which is a fingerprint of strongly-coupled systems.

Fitting of the results with a theoretical model revealed that emitters coupled to rod dimer structures lead to greater coupling strengths than emitters coupled to a single rod structure. This is caused by the reduced mode volume of the electric near field in dimer structures with respect to single rod structure, where in the former an intense electric field hotspot is induced in the gap of the dimer. Further analysis of the results indicate that the coupling of quantum emitters not only induced a mode splitting in antenna resonance due to the strong interaction, but cause a redshift in uncoupled antenna resonance as well. This redshift was interpreted as a change in dielectric environment surrounding the antenna structures after the addition of the emitters. Besides a redshift in uncoupled antenna resonance, it was seen that the uncoupled molecular resonance was redshifted with respect to the assigned absorption resonance of the emitters as well.

The results discussed in this work offer a straightforward and reproducible platform for studying strong light-matter interactions. Furthermore, the observations provide crucial insights for future designs and experiments concerning strong emitter-antenna coupled systems. In the following, examples of such potential experiments are explored.

6.1 Outlook

6.1.1 Helium FIB milled dimers

As discussed in chapter 2, a helium FIB can be used as a nanofabrication technique where features in nanostructures with a resolution superior to EBL can be milled. Therefore, dimer structures with smaller and more controlled gapsizes can be fabricated in this manner. Indeed, it is shown in chapter 3 that dimers fabricated with a helium FIB can create stable gapsizes down to 8 nm, a factor of 3 smaller than the dimer gaps fabricated directly with EBL. The electric field mode volume V in these helium FIB milled dimers is then significantly reduced as well, with a corresponding sharp increase in electric field enhancements as shown in figure 3.7c. Looking back at the expression for the coupling strength, which scales as $g \propto \frac{1}{\sqrt{V}}$, it is expected that the coupling strength increases sharply in these structures. The sharp redshift in fundamental cavity resonance should then be taken into account in the design and fabrication of these helium FIB milled nanostructures.

6.1.2 Light harvesting complexes

Apart from emitters with high intrinsic transition dipole moments (dye molecules) and large absorption cross sections (quantum dots), which are ideal properties for studying strong light-matter interactions, more biologically relevant molecules could be studied as well. One can think for example of light harvesting complexes, which are complexes of proteins structured in such a way as to collect and transfer solar energy in a highly efficient manner and thus are important molecules in photosynthetic processes. One of these complexes is the light harvesting complex 2 (LH2) of purple non-sulphur bacteria, where in this case the complex consists of a cylindrical protein structure containing 27 sub units, the bacteriochlorophyll a (Bchl-a), depicted in figure 6.1a. Together, these Bchls-a form two concentric rings termed the B800 and B850 rings, with absorption maxima at 800 and 850 nm respectively as shown in figure 6.1b. After a photon is absorbed in the B800 ring, the energy in transferred to the B850 ring, after which relaxation and funneling of the energy to a reaction centre occurs, where the photosynthetic process takes place [15]. LH2 thus provides a biologically relevant molecule for studying strong interactions, as the energy levels and thus photosynthetic chemistry can be altered.

Initial experiments with the LH2 molecules has been attempted. In these experiment, the molecules are encapsulated in a polyvinyl alchohol (PVA) matrix, increasing the photostability of the molecules. Again, an ensemble of these molecules is spincoated onto the nano-antenna structures and scattering spectra are captured, of which the results are shown in figures 5.11d. Here scattering spectra of the bare antennas and antennas covered with LH2 molecules in PVA are shown in red and purple respectively. A large redshift is again observed, which is assigned to the change in dieelectric environment caused by the PVA layer. This shift in antenna resonance increases the detuning between the resonance of LH2, which lies around 800 nm as shown in figure 6.1, and the uncoupled antenna resonance. This increased detuning decreases the probability of observing a splitting in antenna resonance and indeed no such split in observed. An advantage of encapsulating emitters in a PVA matrix is that PVA can be easily washed off the antennas by emersing the sample in water. After this is done, all the PVA with LH2 molecules will be removed from the sample. An antenna scattering spectra is again captured after the PVA is removed from the structure shown in figure 6.1c in blue. Due to the disappearance of the PVA matrix, the fundamental antenna resonance shifts back and overlaps with the uncoupled antenna resonance again.

In future experiments, this shift in uncoupled antenna resonance has to be taken into account when adding an ensemble of LH2 molecule encapsulated in a PVA matrix to plasmonic structures. Apart from encapsulating the LH2 in a PVA matrix, it could be possible to chemically bind the LH2 to the nano structures by surface functionalization, as has been done in previous work [64]

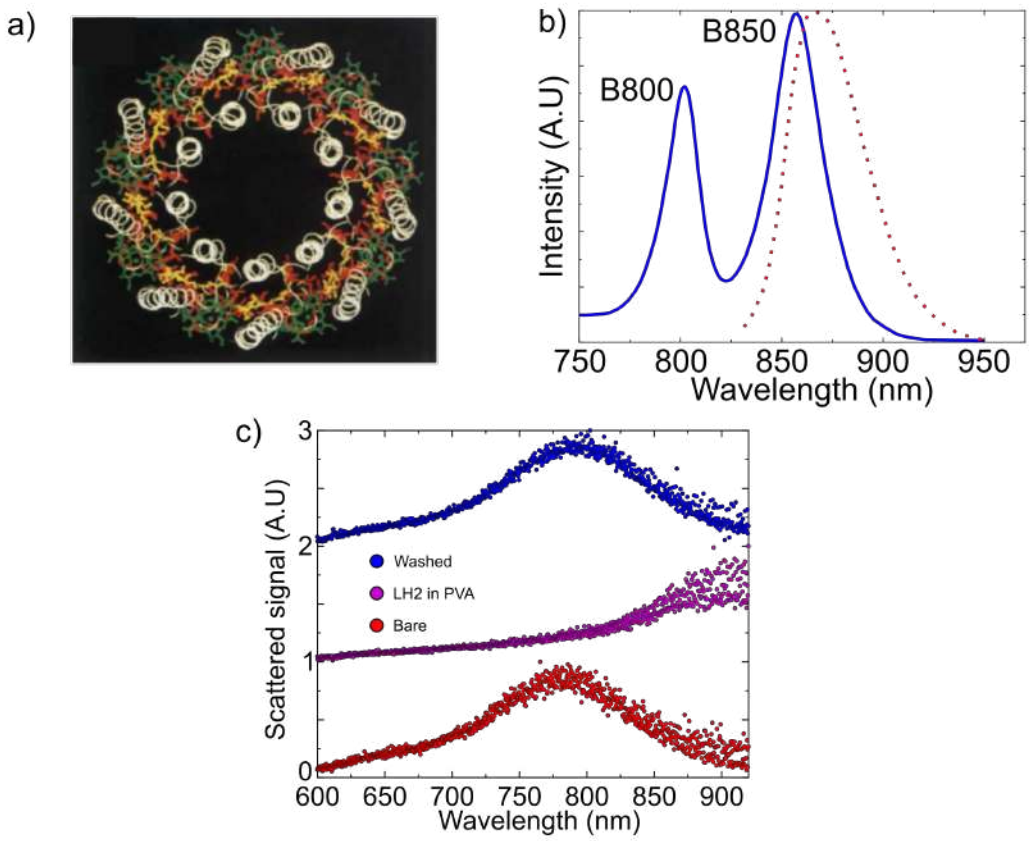

Figure 6.1: a) Structure of LH2 with proteins (white), B800 ring (green), B850 ring (red) and carotenoid (yellow). Figure adapted from [32]. b) Absorption (solid line) and fluorescence (dashed line) spectrum of LH2, adapted from [23]. c) Scattering spectra of a nano antenna before (red) and after (purple) the addition of LH2 molecules in PVA. The scattering spectra of the same antenna after the LH2 in PVA is washed of is shown in blue.

6.1.3 Second step lithography

In this thesis, the strong interaction is studied between an ensemble of quantum emitters and plasmonic nanostructures by spincoating a high concentration of emitters onto the whole sample. While this brute force method ensures that there are indeed emitters present in the near field hotspots of the nano antennas, it is not a very controlled method. Ideally, we would only want to have the quantum emitters present in the hotspots of the antennas. This control of the positioning of quantum emitters can be achieved by performing a secondary EBL step in the nanofabrication. In brief, the first EBL step defines the antenna structures as discussed extensively in chapter 2. After this, the fabricated antenna sample can again be covered by an electronic resist in which patterns can be developed by EBL. These patterns can be chemically functionalized, to which emitters can bind to. After lift-off of the remaining resist, quantum emitters are present only in the predefined patterns as defined in the secondary EBL step. Indeed, this method has been exploited previously to accurately position a single quantum emitter [17] in the vicinity of a nano antenna.

Appendix A

Jaynes-Cummings model

A.1 Jaynes-Cummings model

The model described in this section provides a framework which is able to explain strong cavity-emitter interaction from a purely quantum mechanical picture. We start by writing the Hamiltonian of the full system, which is the sum of the uncoupled emitter and cavity hamiltonians and an interaction term:

$$H_{tot} = H_{emitter} + H_{cavity} + H_{interaction}. \tag{A.1}$$

Next, a two level system is assumed for the emitter with a ground $|g\rangle$ and excited state $|e\rangle$ separated in energy by $E = \hbar\omega_e$. Here, the energy zero point is set halfway between these two levels. The Hamiltonian of the uncoupled emitter may then be described by:

$$H_{emitter} = \frac{1}{2}\hbar\omega_e\hat{\sigma}, \tag{A.2}$$

Where $\hat{\sigma}$ is referred to as the inversion operator, defined to be $\hat{\sigma} = |e\rangle\langle e| + |g\rangle\langle g|$. The emitter is interacting with an electric field $\vec{E}$ confined in a cavity

It is assumed that the cavity field is of single-mode nature. The Hamiltonian of this cavity field can then be written as:

$$H_{cavity} = \hbar\omega_0\hat{a}\hat{a}^\dagger. \tag{A.3}$$

Here, ω_0 is the eigenfrequency of the cavity mode, while $\hat{a}^\dagger$ and $\hat{a}$ are the photon creation and annihilation operators respectively. Because constant terms in a Hamiltonian will only contribute to a phase change, the zero-point energy has been omitted.

In the dipole approximation, which applies when the dimensions of the emitter are small compared to the wavelength, the interaction Hamiltonian can be simplified to:

$$H_{interaction} = -\vec{\mu}\cdot\vec{E}, \tag{A.4}$$

with $\vec{\mu}$ the dipole moment of the emitter. We now introduce the atomic transition operators $\sigma_+ = |e\rangle\langle g|$ and $\sigma_- = |g\rangle\langle e|$. A final simplification can be made by dropping all terms in the interaction Hamiltonian which are oscillating rapidly. Applying this rotating wave approximation, the interaction Hamiltonian finally transforms to:

$$H_{interaction} = \hbar g(\sigma_+\hat{a} + \sigma_-\hat{a}^\dagger), \tag{A.5}$$

with $g = \frac{2\mu\cdot\vec{E}}{\hbar}$ the coupling strength. The total Hamiltonian that is retrieved now is referred to as the Jaynes-Cummings Hamiltonian:

$$H_{JC} = \frac{1}{2}\hbar\omega_e\hat{\sigma} + \hbar\omega_0\hat{a}\hat{a}^\dagger + \hbar g(\sigma_+\hat{a} + \sigma_-\hat{a}^\dagger) \tag{A.6}$$

In order to obtain the eigenfrequencies of the coupled system, the Jaynes-Cummings Hamiltonian can be diagonalized. The following hybrid frequencies $\omega_\pm$ are obtained:

$$\omega_\pm = \frac{1}{2}(\omega_c + \omega_e) \pm \Omega_R, \tag{A.7}$$

where Ω_R is the vacuum Rabi frequency given by:

$$\Omega_R = \sqrt{g^2 + \frac{1}{4}(\omega_c - \omega_e)^2}. \tag{A.8}$$

We now turn to the behaviour of the system in the time domain. When the emitter is in the ground state it is assumed that there are $n+1$ photons present in the cavity and when an emitter is excited the cavity loses one photon in the process. The cavity states can now be described by the number states $|n+1\rangle$ and $|n\rangle$, for ground and excited state respectively. The total states of the cavity-emitter system can now be written as a product of the cavity and emitter states $|0\rangle = |g\rangle\,|n\rangle$ and $|1\rangle = |e\rangle\,|n-1\rangle$, both with energy $E_{tot} = (n + \frac{1}{2})\hbar\omega$. As these form a basis of the system, the wavefunction can be expanded in these states as

$$|\psi(t)\rangle = C_0(t)\,|0\rangle + C_1(t)\,|1\rangle\,. \tag{A.9}$$

By substitution of equation A.9 in the Schrödinger equation $i\hbar\frac{d\Psi(t)}{dt} = H_{JC}\Psi(t)$ we obtain differential equations of the coefficients which can be solved:

$$C_0(t) = cos(\Omega_R t\sqrt{n+1}), \tag{A.10}$$

$$C_1(t) = -isin(\Omega_R t\sqrt{n+1}). \tag{A.11}$$

Here we have assumed that initially the system is in the state $|e\rangle\,|n-1\rangle$ such that $C_1(0) = 1$ and $C_0(0) = 0$. The probabilities that the system is in state $|1\rangle$ or $|2\rangle$ can now be calculated from these coefficients as:

$$P_0(t) = \mid C_0(t) \mid^2 = cos^2(\Omega_R t\sqrt{n+1}), \tag{A.12}$$

$$P_1(t) = sin^2(\Omega_R t\sqrt{n+1}) \tag{A.13}$$

respectively.

It is observed that the state populations are oscillating in time, which are referred to as Rabi oscillations with frequency $\Omega\sqrt{n+1}$, which describes the periodic process of absorption and re-emission of a photon by the emitter in the cavity field. Even when there are no photons initially present in the cavity, oscillations are still predicted by the model. These are the vacuum Rabi oscillations, which is the result of the emitter interacting with the vacuum field fluctuations allowing for spontaneous emission of a photon. This photon is then trapped in the cavity, after which it is reabsorbed, re-emitted etc. The vacuum Rabi frequency thus represents the frequency at which energy is coherently exchanged in a coupled cavity-emitter system.

Appendix B

Simulating antenna-emitter interactions

In the following, it is described in detail how the experimental conditions regarding strong emitter-antenna interactions are mimicked in the FDTD simulations. First, the main model that is able to describe the absorbing nature of an ensemble of emitters is laid out, after which the structure of the simulations are illustrated.

B.1 The Lorentz permitivitty

The Drude model covers the optical response of a free electron gas, which is able to describe the behaviour of metals well for low frequencies. For high frequencies, however, interband transitions cause a significant deviation in the optical behaviour from the free electron gas. The Lorentz model therefore gives an extension to the Drude model, able to account for these interband transitions in metals for higher frequencies. We start the derivation of the lorentz permitivitty from the metal point of view as well, where an electron with mass m_e is subject to dissipation γ, an external driving field $E(t)$ and a harmonic trap with resonance frequency ω_o. The equation of motion for the position $x(t)$ of the electron is then given by:

$$m_e \frac{d^2x(t)}{dt^2} - m_e\gamma\frac{dx(t)}{dt} + m\omega_o^2 x(t) = -eE(t). \tag{B.1}$$

We assume a time harmonic driving field $E(t) = E_0 e^{i\omega t}$ and that the electrons follow this driving field as $x(t) = x_0 e^{i\omega t}$. Substitution of both ansatze into equation B.1 gives the following expression for the position of the electron:

$$x(t) = -\frac{eE}{m_e}\frac{1}{\omega_o^2 - \omega^2 - i\gamma\omega}, \tag{B.2}$$

where the prefactor represents any phase shifts between electron position and driving field. Macroscopically, the displaced electrons contribute to a polarization $P(t)$ of the metal as $P(t) = -nex(t)$:

$$P(t) = \frac{ne^2E}{m_e}\frac{1}{\omega_o^2 - \omega^2 - i\gamma\omega}. \tag{B.3}$$

Now, polarization and electric field are connected by the electric susceptibility χ as $P(t) = \epsilon_0\chi E(t)$, while the dielectric constant ϵ is given by $\epsilon = 1 + \chi$. From these relationships, an expression for the dielectric constant can be written down as follows:

$$\epsilon = 1 + \frac{\omega_p^2}{\omega_0^2 - \omega^2 - i\gamma\omega}, \tag{B.4}$$

where $\omega_p = \sqrt{\frac{ne^2}{\epsilon_o m_e}}$ defines the plasma frequency of the metal.

In the high frequency limit $\omega >> \omega_p$ it is seen that the dielectric function approaches unity. While this is true for a free electron gas, it is not so in the case of noble metals, where the ion cores cause a residual polarization for high frequencies. It is therefore possible to add a background term $P_\infty = \epsilon_0(\epsilon_\infty - 1)E$ to the total polarization, after which the dielectric function transforms to:

$$\epsilon = \epsilon_\infty + \frac{\omega_p}{\omega_0^2 - \omega^2 - i\gamma\omega}. \tag{B.5}$$

In metals, the interband transitions are thus accounted for by adding a harmonic trap term with resonance frequency ω_0 to the equation of motion of a free electron gas. Any number of transitions can be added by extending the expression for the dielectric function into a sum:

$$\epsilon = \epsilon_\infty + \sum_{i=1}^{N} \frac{\omega_p}{\omega_i^2 - \omega^2 - i\gamma_i\omega}, \tag{B.6}$$

where the summation runs over all the interband transitions.

B.2 Simulating emitters

The absorbing nature of the Lorentz model can, however, also be exploited by describing absorbing molecules. This is a very crude approximation indeed, as molecular properties as blinking, bleaching and internal quantum efficiency have been completely omitted. For simulating light matter interactions, however, the transition of the molecule is the most important property and is well covered by this description. Furthermore, as we are coupling an ensemble of emitters to the nanostructures, the approximation is justified.

In the simulations, the dielectric function is described by a Lorentz permitivitty of the form:

$$\epsilon = \epsilon_\infty + \frac{f\omega_0^2}{\omega_0^2 - \omega^2 - i\gamma\omega}, \tag{B.7}$$

where ω_0 and γ are now the molecule resonance and linewidth respectively and ϵ_∞ is again the background permitivitty. A new dimensional quantity f is added here, which describes the strength or probability of absorption. This new factor thus contains information about the inherent dipole and the density of absorbing molecules.

Using formula B.2, we can thus model the dielectric properties of Rho. 800, where ω_0 and γ are extracted from the absorption spectrum of Rho. 800 shown in figure 5.1b as resonance and linewidth respectively. Here, only the absorption of the main transition is taken into account and the weaker sideband is ignored. The background permitivitty ϵ_∞ is assumed to be 1, as the layer of molecules on the sample are immersed in air. The precise value of ϵ_∞ could however be determined using spectroscopic ellipsometry, where the real part of the dieelectric function is measured as a function of the wavelength.

Real and imaginary part of the modelled Rho. 800 molecules are shown in figures B.1a and b. It is seen that the imaginary part, which describes the absorbing (or gain) properties of a medium, is in good agreement with the absorption spectrum of Rho. 800. The simulations are now modelled as a sheet of this medium covering the antenna structure as shown in figure B.1c, of which the thickness can be varied. Finally, the absorption strength of this medium can be varied by changing the parameter f in equation B.1. Figure B.1d shows a series of scattering spectra for a dimer structure covered in an absorbing medium with a thickness of 50 nm. For high values of f, it is seen that the fundamental antenna resonance splits into two hybridized modes, indicating strong interaction between the dimer and the absorbing medium. As f decreases gradually, the splitting vanishes gradually, in agreement with expectations. It is noted that here the splitting is asymetric as well, following the same trend as shown in figure 5.5.

The experiments as described in figures 5.3 and 5.4 are now modelled as follows. The value of f of the absorbing material is chosen such that best overlap is reached with simulation and experiment for the case of rod antennas. The experimental scattering spectra shown in figure 5.3 are thus simulated by fitting of the best value of f, which is $f = 0.1$. Now, all 4 parameters ($\omega_0, \gamma, \epsilon_\infty$ and f are determined and kept fixed in the simulations of the dimer structures shown in figure 5.4.

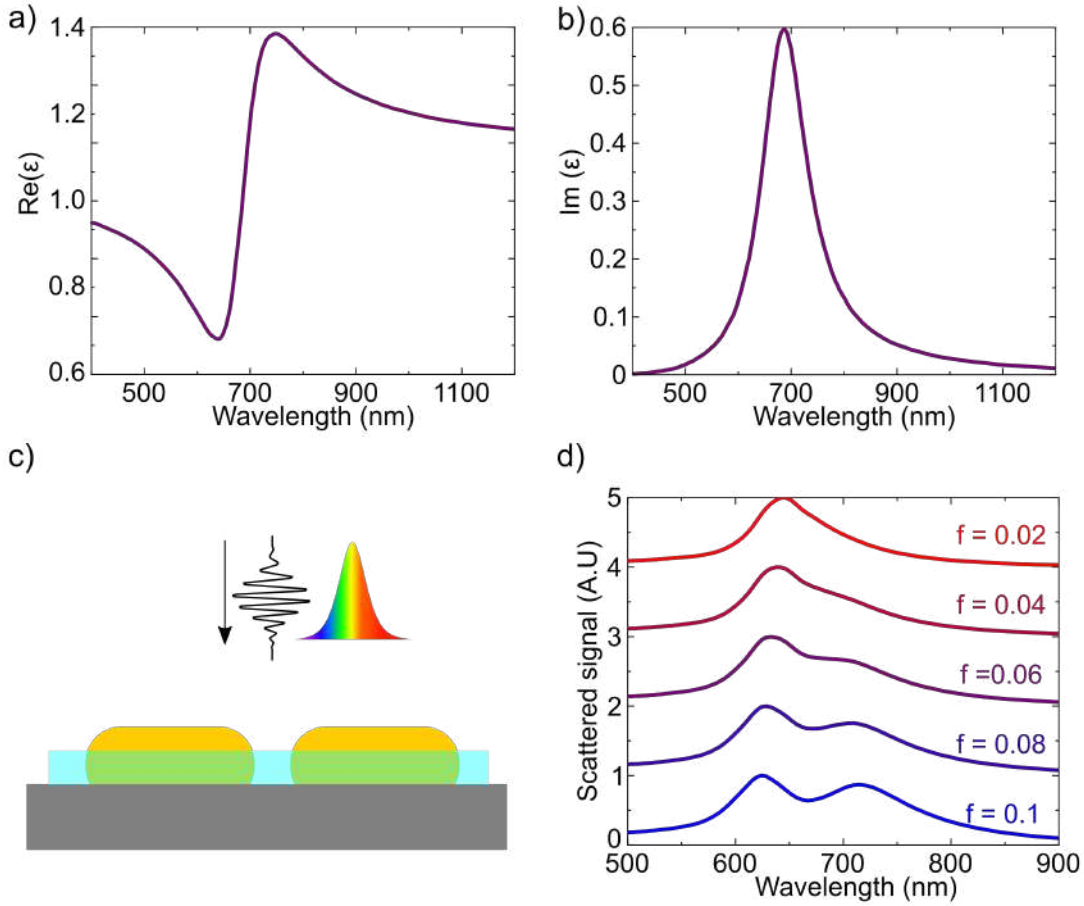

Figure B.1: Simulating antenna-emitter interactions. Real (a) and imaginary (b) part of the dielectric function used to model the ensemble of Rho. 800 dye molecules. c) Structure of the simulations, where a sheet of an absorbing medium is added to the antenna structure. d) Simulated scattering spectra of a dimer structure covered in the Lorentz absorbing material for different absorption strengths f.

Bibliography

[1] Y. Akahane, T. Asano, B.-S. Song, and S. Noda. High-q photonic nanocavity in a two-dimensional photonic crystal. *Nature*, 425(6961):944–947, 2003. 7

[2] L. C. Andreani, G. Panzarini, and J.-M. Gérard. Strong-coupling regime for quantum boxes in pillar microcavities: Theory. *Physical Review B*, 60(19):13276, 1999. 6

[3] J. N. Anker, W. P. Hall, O. Lyandres, N. C. Shah, J. Zhao, and R. P. Van Duyne. Biosensing with plasmonic nanosensors. In *Nanoscience and Technology: A Collection of Reviews from Nature Journals*, pages 308–319. World Scientific, 2010. 9

[4] J. Becker, A. Trügler, A. Jakab, U. Hohenester, and C. Sönnichsen. The optimal aspect ratio of gold nanorods for plasmonic bio-sensing. *Plasmonics*, 5(2):161–167, 2010. 38

[5] J. Bellessa, C. Bonnand, J. Plenet, and J. Mugnier. Strong coupling between surface plasmons and excitons in an organic semiconductor. *Physical review letters*, 93(3):036404, 2004. 11

[6] J. Bellessa, C. Symonds, K. Vynck, A. Lemaitre, A. Brioude, L. Beaur, J. Plenet, P. Viste, D. Felbacq, E. Cambril, et al. Giant rabi splitting between localized mixed plasmon-exciton states in a two-dimensional array of nanosize metallic disks in an organic semiconductor. *Physical Review B*, 80(3):033303, 2009. 11

[7] J.-P. Berenger et al. A perfectly matched layer for the absorption of electromagnetic waves. *Journal of computational physics*, 114(2):185–200, 1994. 28

[8] A. Blais, J. Gambetta, A. Wallraff, D. I. Schuster, S. M. Girvin, M. H. Devoret, and R. J. Schoelkopf. Quantum-information processing with circuit quantum electrodynamics. *Physical Review A*, 75(3):032329, 2007. 13

[9] S. A. Boden, A. Asadollahbaik, H. N. Rutt, and D. M. Bagnall. Helium ion microscopy of lepidoptera scales. *Scanning*, 34(2):107–120, 2012. 23

[10] C. F. Bohren and D. R. Huffman. *Absorption and scattering of light by small particles*. John Wiley & Sons, 2008. 49

[11] D. Bouwmeester, J.-W. Pan, K. Mattle, M. Eibl, H. Weinfurter, and A. Zeilinger. Experimental quantum teleportation. *Nature*, 390(6660):575–579, 1997. 14

[12] R. Chikkaraddy, B. De Nijs, F. Benz, S. J. Barrow, O. A. Scherman, E. Rosta, A. Demetriadou, P. Fox, O. Hess, and J. J. Baumberg. Single-molecule strong coupling at room temperature in plasmonic nanocavities. *Nature*, 535(7610):127–130, 2016. 12

[13] S. Christopoulos, G. B. H. Von Högersthal, A. Grundy, P. Lagoudakis, A. Kavokin, J. Baumberg, G. Christmann, R. Butté, E. Feltin, J.-F. Carlin, et al. Room-temperature polariton lasing in semiconductor microcavities. *Physical review letters*, 98(12):126405, 2007. 14

[14] P.-H. Chung, C. Tregidgo, and K. Suhling. Determining a fluorophore's transition dipole moment from fluorescence lifetime measurements in solvents of varying refractive index. *Methods and Applications in Fluorescence*, 4(4):045001, 2016. 43

[15] R. J. Cogdell, A. Gall, and J. Köhler. The architecture and function of the light-harvesting apparatus of purple bacteria: from single molecules to in vivo membranes. *Quarterly reviews of biophysics*, 39(3):227, 2006. 58

[16] E. A. Coronado and G. C. Schatz. Surface plasmon broadening for arbitrary shape nanoparticles: A geometrical probability approach. *The Journal of chemical physics*, 119(7):3926–3934, 2003. 37

[17] A. G. Curto, G. Volpe, T. H. Taminiau, M. P. Kreuzer, R. Quidant, and N. F. van Hulst. Unidirectional emission of a quantum dot coupled to a nanoantenna. *Science*, 329(5994):930–933, 2010. 10, 59

[18] B. Dubertret, M. Calame, and A. J. Libchaber. Single-mismatch detection using gold-quenched fluorescent oligonucleotides. *Nature biotechnology*, 19(4):365–370, 2001. 54

[19] S. D. Gedney. Introduction to the finite-difference time-domain (fdtd) method for electromagnetics. *Synthesis Lectures on Computational Electromagnetics*, 6(1):1–250, 2011. 27

[20] C. Gerry, P. Knight, and P. L. Knight. *Introductory quantum optics*. Cambridge university press, 2005. 5

[21] H. Gersen, M. F. García-Parajó, L. Novotny, J. Veerman, L. Kuipers, and N. F. van Hulst. Influencing the angular emission of a single molecule. *Physical review letters*, 85(25):5312, 2000. 10

[22] T. Hakala, J. Toppari, A. Kuzyk, M. Pettersson, H. Tikkanen, H. Kunttu, and P. Törmä. Vacuum rabi splitting and strong-coupling dynamics for surface-plasmon polaritons and rhodamine 6g molecules. *Physical review letters*, 103(5):053602, 2009. 11

[23] R. Hildner, D. Brinks, J. B. Nieder, R. J. Cogdell, and N. F. van Hulst. Quantum coherent energy transfer over varying pathways in single light-harvesting complexes. *Science*, 340(6139):1448–1451, 2013. 59

[24] R. Houdré, R. Stanley, U. Oesterle, M. Ilegems, and C. Weisbuch. Room-temperature cavity polaritons in a semiconductor microcavity. *Physical Review B*, 49(23):16761, 1994. 7

[25] J. A. Hutchison, T. Schwartz, C. Genet, E. Devaux, and T. W. Ebbesen. Modifying chemical landscapes by coupling to vacuum fields. *Angewandte Chemie International Edition*, 51(7):1592–1596, 2012. 14

[26] A. Imamog, R. Ram, S. Pau, Y. Yamamoto, et al. Nonequilibrium condensates and lasers without inversion: Exciton-polariton lasers. *Physical Review A*, 53(6):4250, 1996. 14

[27] P. B. Johnson and R.-W. Christy. Optical constants of the noble metals. *Physical review B*, 6(12):4370, 1972. 31

[28] Y. Kaluzny, P. Goy, M. Gross, J. Raimond, and S. Haroche. Observation of self-induced rabi oscillations in two-level atoms excited inside a resonant cavity: The ringing regime of superradiance. *Physical review letters*, 51(13):1175, 1983. 7

[29] D. G. Lidzey, D. Bradley, M. Skolnick, T. Virgili, S. Walker, and D. Whittaker. Strong exciton–photon coupling in an organic semiconductor microcavity. *Nature*, 395(6697):53–55, 1998. 7

[30] D. G. Lidzey, D. D. Bradley, A. Armitage, S. Walker, and M. S. Skolnick. Photon-mediated hybridization of frenkel excitons in organic semiconductor microcavities. *Science*, 288(5471):1620–1623, 2000. 7

[31] S. A. Maier. Plasmonic field enhancement and sers in the effective mode volume picture. *Optics Express*, 14(5):1957–1964, 2006. 11

[32] G. McDermott, S. Prince, A. Freer, A. Hawthornthwaite-Lawless, M. Papiz, R. Cogdell, and N. Isaacs. Crystal structure of an integral membrane light-harvesting complex from photosynthetic bacteria. *Nature*, 374(6522):517–521, 1995. 59

[33] J. Mooney and P. Kambhampati. Get the basics right: Jacobian conversion of wavelength and energy scales for quantitative analysis of emission spectra, 2013. 50

[34] F. Neubrech, D. Weber, R. Lovrincic, A. Pucci, M. Lopes, T. Toury, and M. L. de La Chapelle. Resonances of individual lithographic gold nanowires in the infrared. *Applied Physics Letters*, 93(16):163105, 2008. 11

[35] J. Notte, B. Ward, N. Economou, R. Hill, R. Percival, L. Farkas, and S. McVey. An introduction to the helium ion microscope. In *AIP Conference proceedings*, volume 931, pages 489–496. American Institute of Physics, 2007. 23, 24

[36] C. Novo, D. Gomez, J. Perez-Juste, Z. Zhang, H. Petrova, M. Reismann, P. Mulvaney, and G. V. Hartland. Contributions from radiation damping and surface scattering to the linewidth of the longitudinal plasmon band of gold nanorods: a single particle study. *Physical Chemistry Chemical Physics*, 8(30):3540–3546, 2006. 37

[37] L. Novotny. Effective wavelength scaling for optical antennas. *Physical Review Letters*, 98(26):266802, 2007. 11

[38] L. Novotny. Strong coupling, energy splitting, and level crossings: A classical perspective. *American Journal of Physics*, 78(11):1199–1202, 2010. 2, 3

[39] L. Novotny and S. J. Stranick. Near-field optical microscopy and spectroscopy with pointed probes. *Annu. Rev. Phys. Chem.*, 57:303–331, 2006. 9

[40] O. S. Ojambati, R. Chikkaraddy, W. D. Deacon, M. Horton, D. Kos, V. A. Turek, U. F. Keyser, and J. J. Baumberg. Quantum electrodynamics at room temperature coupling a single vibrating molecule with a plasmonic nanocavity. *Nature communications*, 10(1):1–7, 2019. 53

[41] E. D. Palik. *Handbook of optical constants of solids*, volume 3. Academic press, 1998. 31

[42] M. Pelton, S. D. Storm, and H. Leng. Strong coupling of emitters to single plasmonic nanoparticles: exciton-induced transparency and rabi splitting. *Nanoscale*, 11(31):14540–14552, 2019. 6, 49

[43] T. Pons, I. L. Medintz, K. E. Sapsford, S. Higashiya, A. F. Grimes, D. S. English, and H. Mattoussi. On the quenching of semiconductor quantum dot photoluminescence by proximal gold nanoparticles. *Nano letters*, 7(10):3157–3164, 2007. 54

[44] E. M. Purcell. Spontaneous emission probabilities at radio frequencies. In *Confined Electrons and Photons*, pages 839–839. Springer, 1995. 6

[45] P. Rai-Choudhury. *Handbook of microlithography, micromachining, and microfabrication: microlithography*, volume 1. Iet, 1997. 22

[46] M. Raizen, R. Thompson, R. Brecha, H. Kimble, and H. Carmichael. Normal-mode splitting and linewidth averaging for two-state atoms in an optical cavity. *Physical review letters*, 63(3):240, 1989. 7

[47] J. P. Reithmaier, G. Sek, A. Löffler, C. Hofmann, S. Kuhn, S. Reitzenstein, L. Keldysh, V. Kulakovskii, T. Reinecke, and A. Forchel. Strong coupling in a single quantum dot–semiconductor microcavity system. *Nature*, 432(7014):197–200, 2004. 7

[48] G. Rempe, H. Walther, and N. Klein. Observation of quantum collapse and revival in a one-atom maser. *Physical review letters*, 58(4):353, 1987. 7

[49] E.-M. Roller, C. Argyropoulos, A. Hogele, T. Liedl, and M. Pilo-Pais. Plasmon–exciton coupling using dna templates. *Nano Letters*, 16(9):5962–5966, 2016. 11

[50] G. Romero, D. Ballester, Y. Wang, V. Scarani, and E. Solano. Ultrafast quantum gates in circuit qed. *Physical Review Letters*, 108(12):120501, 2012. 13

[51] S. Rudin and T. Reinecke. Oscillator model for vacuum rabi splitting in microcavities. *Physical Review B*, 59(15):10227, 1999. 53

[52] K. Santhosh, O. Bitton, L. Chuntonov, and G. Haran. Vacuum rabi splitting in a plasmonic cavity at the single quantum emitter limit. *Nature communications*, 7(1):1–5, 2016. 12, 48

[53] A. E. Schlather, N. Large, A. S. Urban, P. Nordlander, and N. J. Halas. Near-field mediated plexcitonic coupling and giant rabi splitting in individual metallic dimers. *Nano letters*, 13(7):3281–3286, 2013. 11

[54] K. Şendur and W. Challener. Near-field radiation of bow-tie antennas and apertures at optical frequencies. *Journal of microscopy*, 210(3):279–283, 2003. 41

[55] Sigmaaldrich. Molecular structure of rhodamine 800. 44

[56] Y. Sugawara, T. Kelf, J. Baumberg, M. Abdelsalam, and P. Bartlett. Strong coupling between localized plasmons and organic excitons in metal nanovoids. *Physical review letters*, 97(26):266808, 2006. 11

[57] D. M. Sullivan. *Electromagnetic simulation using the FDTD method*. John Wiley & Sons, 2013. 27

[58] L. support. Symmetric and anti-symmetric bcs in fdtd and mode. 30

[59] O. Svelto and D. C. Hanna. *Principles of lasers*, volume 1. Springer, 2010. 14

[60] L. Tang, S. E. Kocabas, S. Latif, A. K. Okyay, D.-S. Ly-Gagnon, K. C. Saraswat, and D. A. Miller. Nanometre-scale germanium photodetector enhanced by a near-infrared dipole antenna. *Nature Photonics*, 2(4):226–229, 2008. 9

[61] R. Thompson, G. Rempe, and H. Kimble. Observation of normal-mode splitting for an atom in an optical cavity. *Physical review letters*, 68(8):1132, 1992. 7

[62] C. Weisbuch, M. Nishioka, A. Ishikawa, and Y. Arakawa. Observation of the coupled exciton-photon mode splitting in a semiconductor quantum microcavity. *Physical Review Letters*, 69(23):3314, 1992. 7

[63] M. Wersall, J. Cuadra, T. J. Antosiewicz, S. Balci, and T. Shegai. Observation of mode splitting in photoluminescence of individual plasmonic nanoparticles strongly coupled to molecular excitons. *Nano letters*, 17(1):551–558, 2017. 11, 53

[64] E. Wientjes, J. Renger, A. G. Curto, R. Cogdell, and N. F. van Hulst. Nanoantenna enhanced emission of light-harvesting complex 2: the role of resonance, polarization, and radiative and non-radiative rates. *Physical Chemistry Chemical Physics*, 16(45):24739–24746, 2014. 58

[65] E. Wientjes, J. Renger, A. G. Curto, R. Cogdell, and N. F. Van Hulst. Strong antenna-enhanced fluorescence of a single light-harvesting complex shows photon antibunching. *Nature communications*, 5(1):1–7, 2014. 6

[66] X. Wu, S. K. Gray, and M. Pelton. Quantum-dot-induced transparency in a nanoscale plasmonic resonator. *Optics express*, 18(23):23633–23645, 2010. 48

[67] G. A. Wurtz, P. R. Evans, W. Hendren, R. Atkinson, W. Dickson, R. J. Pollard, A. V. Zayats, W. Harrison, and C. Bower. Molecular plasmonics with tunable exciton- plasmon coupling strength in j-aggregate hybridized au nanorod assemblies. *Nano letters*, 7(5):1297–1303, 2007. 11

[68] K. Yee. Numerical solution of initial boundary value problems involving maxwell's equations in isotropic media. *IEEE Transactions on antennas and propagation*, 14(3):302–307, 1966. 28

[69] T. Yoshie, A. Scherer, J. Hendrickson, G. Khitrova, H. Gibbs, G. Rupper, C. Ell, O. Shchekin, and D. Deppe. Vacuum rabi splitting with a single quantum dot in a photonic crystal nanocavity. *Nature*, 432(7014):200–203, 2004. 7

[70] G. Zengin, M. Wersäll, S. Nilsson, T. J. Antosiewicz, M. Käll, and T. Shegai. Realizing strong light-matter interactions between single-nanoparticle plasmons and molecular excitons at ambient conditions. *Physical review letters*, 114(15):157401, 2015. 11

[71] P. Zijlstra, P. M. Paulo, and M. Orrit. Optical detection of single non-absorbing molecules using the surface plasmon resonance of a gold nanorod. *Nature nanotechnology*, 7(6):379–382, 2012. 52